Dissertation
submitted to the
Combined Faculties for Natural Sciences and for Mathematics
of the Ruperto-Carola University of Heidelberg, Germany
for the degree of
Doctor of Natural Sciences

presented by
Dipl.-Phys. Simon Martin Altevogt
born in Göttingen
Oral examination: 24th of July, 2007

Fast-beam Photodissociation Imaging of Molecular Ions

Referees:

Prof. Dr. Andreas Wolf
Prof. Dr. Peter Schmelcher

Kurzfassung

Abbildung von Photofragmentationsprozessen schneller Molekülionen

Ein neuartiger experimenteller Aufbau zur Messung von Photofragmentationsprozessen molekularer Ionen wurde etabliert. Der Aufbau kombiniert das Verfahren der Abbildung schneller Ionenstrahlen (keV Energien) mit einer Ionenfalle, die es erlaubt die Vibrationsanregungen der Ionen zu reduziern. Der Aufbau wurde am Freie-Elektronen-Laser (FEL) in Hamburg für die ersten Benutzer Experimente installiert. Mit der Apparatur wurden unter Verwendung eines gepulsten Nd:YAG Lasers (Photonen Energien von 2.33 und 4.66eV) Experimente an den Edelgasionen Ar_2^+ und Ne_2^+ und an HeH^+ unter Benutzung des FEL mit 38.8eV durchgeführt. Die Photodissoziation von Ar_2^+ wurde bei 266nm gemessen, wobei die $C^2\Sigma_g^+$ Potentialfläche dominierte. Die Winkelverteilung der Fragmente zeigte, den erwarteten hauptsächlichen Anteil an Dissoziation parallel zur Laserpolarization. Jedoch wurde auch ein beträchtlicher senkrechter Beitrag mit zunehmender bei der Dissoziation freiwerdender Energie gemessen. Obwohl die Annahme von Spin-Bahn Wechselwirkung die plausibelste Erklärung darstellt, war die beobachtete Größe des Effektes wesentlich höher, als durch theoretische Rechnungen vorhergesagt. Es wurde beobachtet, daß bei der Photofragmentation von Ne_2^+ bei 523nm die $A^2\Pi_u$ Potentialfläche dominiert. Die $C^2\Sigma_g^+$ Potentialkurve gewinnt an Bedeutung für höhere vibrations Anregung der Molekülionen. Experimentell wurde auch hier ein hauptsächlicher paralleler Charakter zusätzlich zu einem senkrechten Anteil gemessen. Der senkrechte Anteil blieb erhöht über den gesamten beobachteten Bereich der freiwerdenden kinetischen Energie. Die Photofragmentationsspektroskopie von HeH^+ am FEL bei 32nm zeigte im Spektrum der freiwerdenden Energie einen Anteil von ≈50% an hochangeregten He^0 Fragmenten, der den Beitrag vieler hoch angeregter Potentialflächen deutlich machte. Die Winkelverteilung zeigte einen dominierenden Anteil an $\Sigma \rightarrow \Pi$ Übergängen, die den wichtigen Beitrag dieser Symmetry zum Dissoziationsprozeß unterstreicht. Der gemessene Wirkungsquerschnitt für beide Symmetrien beträgt $(1.4 \pm 0.7) \cdot 10^{-18}\mathrm{cm}^2$.

Abstract

Fast-beam photodissociation imaging of molecular ions

A novel arrangement to study photofragmentation of molecular ions using fast beam (keV) imaging techniques combined with fast ion-beam pulsing and trapping has been realized. The setup was transferred to the new free-electron laser in Hamburg (FLASH) for the first user experiments. With this apparatus experiments were conducted on the two rare-gas dimer ions Ne_2^+ and Ar_2^+ utilizing a pulsed Nd:YAG laser at 2.33 and 4.66eV photon energy and on HeH^+ using the free electron laser at 38.8 eV. Photofragmentation of Ar_2^+ was measured at 266nm, where the $C^2\Sigma_g^+$ repulsive curve dominates. The angular fragment distribution was mainly parallel to the laser polarization, as expected, but a sizable transverse contribution increasing at energy releases corresponding to vibrationally excited target ions was found. Although spin-orbit coupling in Ar_2^+ remains as the most plausible explanation, the observed size of the effect is much larger than expected using theoretical predictions. Photodissociation of the Ne_2^+ was measured at 532nm where the $A^2\Pi_u$ curve is dominant and the $C^2\Sigma_g^+$ curve becomes important for higher vibrational target excitation. Also here, a mainly parallel angular charactistic was observed plus a perpendicular contribution which remained high throughout the observed kinetic energy release regime. The photofragmentation studies of HeH^+ with the free electron laser at 32nm wavelength, revealed in the kinetic energy release spectrum, a contribution of ≈50% from highly excited He^0 fragments, indicating the important contribution of many high-lying repulsive curves. The angular distributions showed a dominant contribution of $\Sigma \rightarrow \Pi$ transitions, underlining the large importance of this symmetry among the excited curves contributing to photodissociation. The cross sections for both symmetries were measured with a total of $(1.4 \pm 0.7) \cdot 10^{-18}\mathrm{cm}^2$.

Meinen Eltern

Contents

1 Introduction **1**

2 Background **5**

2.1 Photodissociation of diatomic ions 5

2.1.1 Photodissociation processes 5

2.1.2 Quantum mechanical treatment 7

2.2 Experimental techniques 10

2.2.1 Gas phase and trapped ion techniques 10

2.2.2 Fast ion beams 11

2.3 The kinematics of two body breakup 12

2.4 Angular distribution of photofragments 15

2.5 Monte Carlo simulations 16

3 A crossed ion beam setup for photodissociation imaging **19**

3.1 Basic elements of the setup 19

3.2 The **T**rapped **I**on **F**ragmentation setup at **F**LASH (TIFF) 21

3.2.1 Historic development 21

3.2.2 Beamline setup 21

3.2.3 Ion beam transport 24

3.2.4 Ion beam diagnostic 26

3.2.5 Ion beam pulsing 27

3.2.6 The vacuum system 27

3.3 The hollow cathode ion source 28

3.4 The ion beam trap 31

3.4.1 An electrostatic ion trap 31

3.4.2 Trap stability criteria 31

3.4.3 Ion trap mechanical construction 32

3.4.4 Electrostatic mirrors 32

3.4.5 Ion trap operation 35

3.5 Interaction region 38

3.5.1 Layout of the interaction region . . . 38
3.5.2 Forced overlap method used in the optical laser experiments . . . 39
3.5.3 Diagnostic of the overlap region at FLASH . . . 39
3.6 Photofragment detection . . . 43
3.6.1 The principle of delay line detection . . . 43
3.6.2 The delay line detector . . . 44
3.7 Light sources . . . 46
3.7.1 The Nd:YAG laser system . . . 46
3.7.2 The VUV free-electron laser at DESY in Hamburg (FLASH) . . . 48

4 Commissioning of the setup **53**
4.1 Control of the experiment . . . 53
4.1.1 Data acquisition system and timing of the experiment . . . 53
4.1.2 Power supplies . . . 53
4.1.3 Programatic control of the setup . . . 55
4.1.4 The vacuum interlock system . . . 56
4.2 Characterization of the ion source . . . 57
4.3 Characterization of the ion beam trap . . . 59
4.3.1 Stability of the ion beam trap . . . 59
4.3.2 Trapping and extraction from the ion beam trap . . . 61
4.4 Beam overlap measurements . . . 65
4.5 Detector calibration . . . 66

5 Optical laser experiments **69**
5.1 Rare gas dimer ions . . . 69
5.2 Timing and data acquisition . . . 73
5.3 Photodissociation of Ar_2^+ at 266nm . . . 74
5.3.1 Experimental parameters . . . 74
5.3.2 Fragment imaging . . . 74
5.3.3 Kinetic energy release and angular distributions . . . 78
5.3.4 Discussion . . . 83
5.3.5 Comparison to theoretical calculations . . . 86
5.4 Photofragmentation studies of Ne_2^+ ions at 532nm . . . 89
5.4.1 Experimental parameters . . . 89
5.4.2 Fragment imaging . . . 89
5.4.3 Kinetic energy release and angular distributions . . . 92
5.4.4 Discussion . . . 97

6 Free electron laser experiments **99**
6.1 Significance of the HeH^+ ion 99
6.2 Timing requirements 101
6.3 HeH^+ photodissociation using VUV photons at 32nm 104
6.3.1 Comparison to theoretical studies of the HeH^+ system 109

7 Summary and outlook **111**
7.1 Summarized results and conclusions 111
7.2 Outlook 113

References **115**

1. Introduction

The inner molecular dynamics at short internuclear separations are of importance for the theoretical understanding because they define the pathways a molecule can take in a reaction process. Photofragmentation studies provide a well controlled access to these regions, and the fragments resulting from the dissociative reactions carry information on the participating potential surfaces and their dynamical couplings.

Photodissociation can occur in a direct bound-continuum transition, in which case the emerging photofragments hold information about the vibrational levels of the bound state as well as information about the shape and symmetry of the dissociative state. This information manifests itself in the amount of energy released in the dissociation process and the angular distribution of fragments after dissociation. Indirect photodissociation involves an initial transition from a bound state to a higher lying quasi-bound state that subsequently dissociates via coupling to a repulsive potential energy surface. From the fragments emerging from such processes information on the lifetimes of the excited state and the dissociation mechanism can be obtained.

Spectroscopic information of molecular ions is in general much more difficult to obtain compared to neutral molecules, owing to the low target densities of 10^4 to $10^6 \mathrm{cm}^{-3}$ typically attainable. Photofragmentation spectroscopy has proven particularly adept in extracting spectroscopic information from the studies of molecular ions. This is mainly due to the fact that dissociation of molecular ions results in a neutral and a charged photofragment. These charged fragments can generally be detected with very high efficiencies.

These motivations have sparked extensive research in the field of molecular ion photofragment spectroscopy. Starting with the first pioneering experiments of Dehmelt and Jefferts [28] in 1962, who employed photodissociation by photons emitted by a powerful arc lamp as a probe to obtain the radio frequency spectrum of H_2^+ ions trapped in a rf quadrupole trap.

The advent of lasers opened up new possibilities since the low target densities could be compensated by higher photon intensities. One of the first to apply these new light sources to study photofragmentation were Ozenne et al. [77] in 1972. Since then various lasers have been used in photofragment studies and the evolution in the field has basically followed the advances in laser development. Starting with studies on H_2^+ using ruby lasers [77, 106, 107], to high resolution studies in the visible in the case of O_2^+ [37], to experiments using UV lasers [54]. For molecules some experimental results exist using VUV photon sources such as synchrotrons, for example in

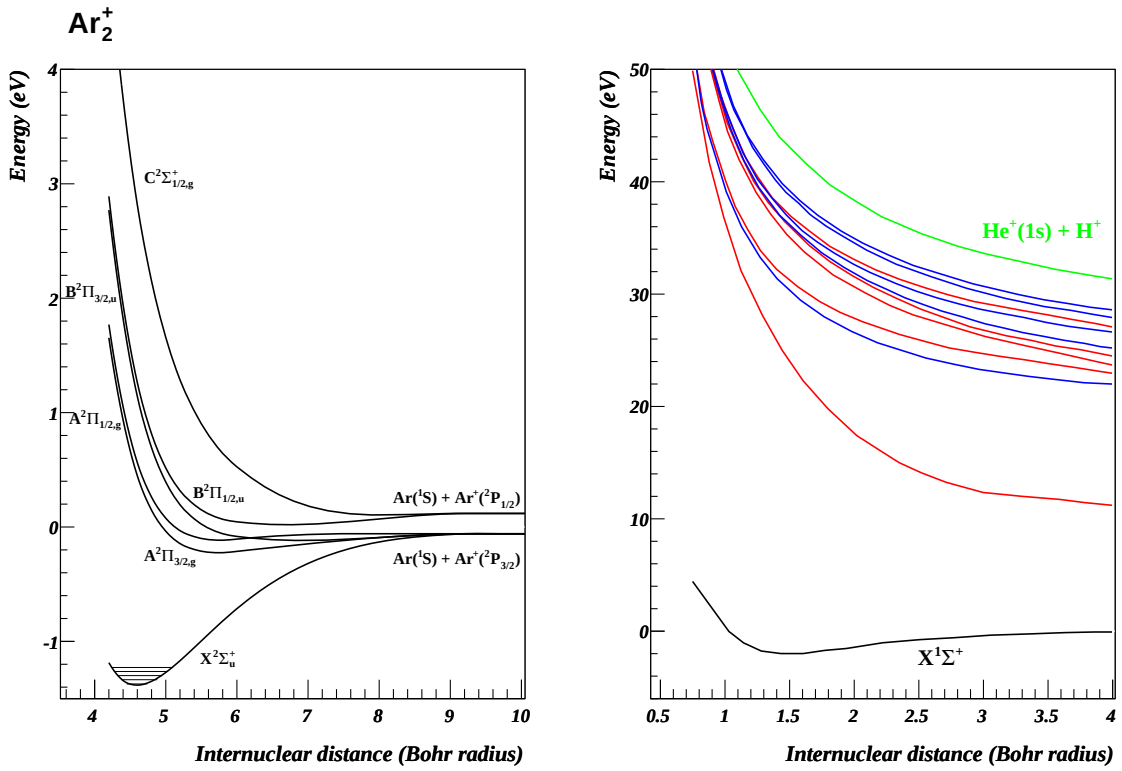

Figure 1.1: *Exemplary potential energy surfaces for the Ar_2^+ system [66] and the HeH^+ ion [82].*

the case of the CO molecule which was studied by Stark and co workerst [100].
Most of these aforementioned experiments used fast beams of molecular ions with several keV energies which were overlapped with a photon beam in either a collinear or a crossed geometry relying on detection of the charged photofragments with energy analyzers. These experiments achieved superb energy resolutions of 0.001-10meV [42] ceding very profound results on the shape of the potential energy surfaces taking part in the dissociation process. However, the information that could be obtained on angular distributions of the photofragments was limited. Exemplary potential curves of two systems presented in the scope of this work are displayed in Fig. 1.1. The left graph shows the Ar_2^+ system. This particular system shows various excited potential energy surfaces which arise from a ground state rare gas atom and a ground state ion. These excited states are still accessible using conventional laser sources. The different states are partly subject to splitting and mixing due to the spin orbit interaction. Many of these systems have been subject in previous investigations. However, better access to the angular distributions of photofragments can yield more detailed insight into the character and magnitude of these coupling effects which was not possible before.
Many molecular ions feature a vast manifold of highly excited potential energy surfaces, an example of which is the HeH^+ ion depicted in the right figure of Fig. 1.1. These high lying

potential energy surfaces correlate to excited atomic final states and can only be reached by energetic photons which were so far not available with sufficiently high intensities. Thus, the chemical dynamics on these high lying states leading to various fragmentation channels is at the moment largely unexplored.

Besides being of fundamental interest photofragmentation processes with energetic photons are also of importance in astrophysics. Photodissociation is one of the main destruction mechanisms for molecules and ions in the interstellar medium [57, 49]. For instance, photodissociation processes play a dominant role in the chemistry of diffuse clouds and in the outer parts of dense clouds [9]. Moreover, photodissociation not only leads to the destruction of molecules and molecular ions but it can also affect the chemistry in these clouds by producing atomic fragments with significant kinetic energy which leads to a heating of the ambient gas [49]. In some cases electronically excited fragments may be formed, which radiate and influence the ambient radiation field (see for instance [33] and references therein).

The wavelength regime of the interstellar radiation field, which is of importance for photodissociation processes, has been modeled by various groups, see for example [40] and [49], and was also subject to measurements [41]. Predictions of the intensities by the divers models differ by factors. However, they all show high photon flux in the VUV regime, due to Lyman α radiation from excited atomic hydrogen. Thus, in order to interpret or predict the observed abundances of molecules and molecular ions in these regions, an accurate knowledge of the photodissociation cross sections of various species of molecules and molecular ions even at low wavelengths is a prerequisite.

A number of recent developments now enables new insight into excited states to be gained with photodissociation experiments.

Development in detector technology has yielded imaging detectors that can record arrival time and position of charged as well as neutral fragments. This not only makes it possible to detect all particles resulting from a photodissociation reaction, but using these detectors energy release and angular distribution of the photofragments are directly accessible.

New 4th generation synchrotron radiation light sources have been developed, for instance the **F**ree-electron **LAS**er in **H**amburg (FLASH) started user operation in late 2005. These new light sources offer high photon flux in the vacuum ultra-violet (VUV) to soft X-ray wavelength regime. This development thus opens up the possibility to perform experiments on molecular ions or radicals using VUV photons despite the low target densities.

New developments in ion trapping techniques has lead to the appearance of table top devices which allow storage of fast ion beams for several 100ms [114, 24]. This allows to prepare the molecular ions in their vibrational ground state or to perform time dependent studies on these molecular ions.

Motivated by these three major developments, a new apparatus suitable for studying photofragmentation processes using VUV as well as conventional laser based light sources was designed.

In this work the new **T**rapped **I**on **F**ragmentation experiment at **F**LASH (TIFF) will be introduced. This novel setup combines the technique of fast ion beams at keV energies with a 3-dimensional imaging detector and an ion beam trap to allow cooling of the ions prior to dissociation. The TIFF experiment was designed and setup at the Max-Planck-Institut für Kernphysik in Heidelberg and was installed at the plane grating monochromator beamline (PG2) at FLASH in late 2005.
This work will present first results obtained on photodissociation studies of rare gas dimer ions, namely Ar_2^+ and Ne_2^+ , using UV and visible radiation. Additionally, first results achieved in a pathfinding experiment using VUV photons to study photofragmentation of HeH^+ ions, will be reported.

2. Background

2.1 Photodissociation of diatomic ions

2.1.1 Photodissociation processes

Studies of molecular photodissociation typically yield information on the characteristics of the bound states of the molecule or molecular ion as well as the symmetry and shape of the excited states involved in the dissociation process. Photofragment spectroscopy has been applied to obtain spectroscopic information from molecules but has proven particularly adept at investigating transitions in molecular ions [72].

The process of photodissociation of a diatomic molecular ion AB^+ is written as

$$AB^+ + h\nu \rightarrow (AB^+)^* \rightarrow A^+ + B. \tag{2.1}$$

Through a dipole allowed transition the molecular ion is transferred into an intermediate excited state which eventually breaks up into a neutral and an atomic photofragment. For a molecule the photodissociation process can be written similar to Eq. 2.1. Two distinct mechanisms of photodissociation are depicted schematically in Fig. 2.1.

Direct photodissociation

Photodissociation can occur through direct coupling to the continuum of the nuclear motions via a repulsive upper state as illustrated in Fig. 2.1 a). Since spontaneous emission back to the ground state is slow compared to the movement along the nuclear coordinate, all absorptions lead to dissociation of the molecule or molecular ion.

In this mechanism, the photodissociation cross section is continuous as a function of photon energy, and the maximum of the cross section is found close to the vertical excitation energy indicated by the arrow in Fig. 2.1 a) [108].

Direct photodissociation can also occur by absorption into the repulsive part of a potential curve which exhibits a bound well at larger distances (not shown in Fig. 2.1).

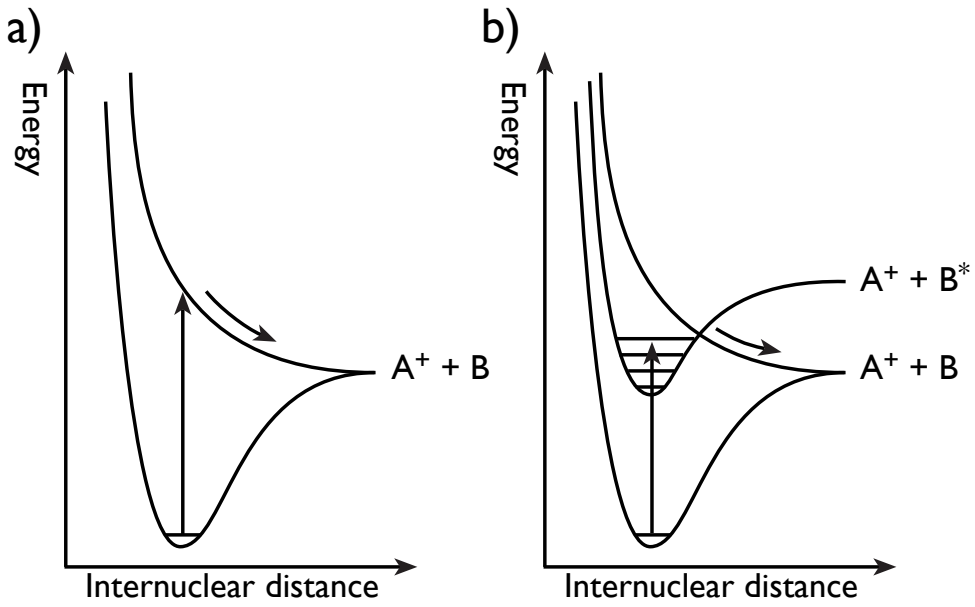

Figure 2.1: *Electronic potential energy curves as function of the internuclear distance illustrating processes of photodissociation for a diatomic molecular ion AB^+. The processes described in the figure are a) the direct photodissociation process, where the bound state of a molecule or molecular ion is directly coupled to a continuum state. The mechanism of predissociation is illustrated in b). This indirect process begins with line absorption into a bound vibrational level of an excited electronic state which is coupled to a third dissociative state of different symmetry. Transitions to the dissociating state occur without the emission of radiation and lead to the breakup of the molecule or molecular ion.*

Indirect photodissociation processes

Indirect photodissociation processes are not of importance for this study but shall nevertheless be briefly mentioned. A detailed account of the indirect dissociation mechanism can be found in the article by Kirby [49] and references therein.
The process of indirect photodissociation is illustrated in Fig. 2.1 b). Here the initial absorption occurs into a quasi-bound state which subsequently couples to a dissociating continuum.
In the case of indirect photodissociation one can distinguish between three different mechanisms. In predissociation (see Fig. 2.1 b)) the bound levels of an excited quasi-bound state are coupled to the continuum state. This third state usually crosses the excited electronic state. The cross section for predissociation consists of a series of discrete peaks, broadened by the predissociating process.
A second possible mechanism of indirect dissociation is the so called coupled states dissociation (not shown in Fig. 2.1). Here the quasi-bound excited electronic state is coupled to a repulsive state which does not cross the bound excited state. A third possibility is the spontaneous radiative dissociation. In this process spontaneous emission of radiation occurs as the molecule or ion makes a transition from a bound excited state into the continuum of a lower lying repulsive state.

2.1.2 Quantum mechanical treatment

Electronic and nuclear wavefunctions

In a molecule the forces acting on the atoms and electrons are comparable in size while the respective masses differ to a large extent. Thus, the nuclear motions are much slower than the electronic motions and both can effectively be treated independently and it is a good approximation to determine the electronic states at each value of the internuclear separation by treating the nuclei as fixed. This is called the Born-Oppenheimer (BO) approximation [16] which shall be briefly described here while a more detailed description can be found in [17].
To define the BO approximation let's consider a diatomic system with N electrons. The time independent Schrödinger equation for the system (neglecting spin interactions) is

$$(T_N + T_e + V)\Psi(\mathbf{R}, \mathbf{r}_1, \mathbf{r}_2, ..., \mathbf{r}_N) = E\Psi(\mathbf{R}, \mathbf{r}_1, \mathbf{r}_2, ..., \mathbf{r}_N), \tag{2.2}$$

where $\mathbf{R}$ denotes the internuclear coordinate and $\mathbf{r}_i$ are the position vectors of the electrons with respect to the center of mass of the molecule which is assumed to be fixed. T_N thereby denotes the kinetic energy operator of the nuclei, T_e is the electron kinetic energy operator and V is the potential energy of the system which consists of the sum of the Coulomb interactions between all pairs of particles.
In the case where the electrons move in the field of the fixed nuclei Eq. 2.2 simplifies to

$$(T_e + V)\Phi_q(\mathbf{R}, \mathbf{r}_1, \mathbf{r}_2, ..., \mathbf{r}_N) = E_q(\mathbf{R})\Phi_q(\mathbf{R}, \mathbf{r}_1, \mathbf{r}_2, ..., \mathbf{r}_N). \tag{2.3}$$

This is known as the electronic wave equation [17]. The eigenvalues $E_q(\mathbf{R})$ and the wavefunctions Φ_q for each electronic state q depend parametrically on the internuclear coordinate $\mathbf{R}$.
The wavefunctions Φ_q form a complete orthonormal set for each value of $\mathbf{R}$, thus the exact wavefunction Ψ can be expanded as

$$\Psi(\mathbf{R}, \mathbf{r}_1, \mathbf{r}_2, ..., \mathbf{r}_N) = \sum_q F_q(\mathbf{R})\Phi_q(\mathbf{R}, \mathbf{r}_1, \mathbf{r}_2, ..., \mathbf{r}_N), \tag{2.4}$$

where $F_q(\mathbf{R})$ represents the nuclear motion wavefunction for the electronic state q. Inserting this in the Schrödinger equation (Eq. 2.2) and projecting the equation with $\Phi_{q'}$ yields

$$\sum_q \int d\mathbf{r}_1 d\mathbf{r}_2 ... d\mathbf{r}_N \Phi^*_{q'}(T_N + T_e + V - E)F_q(\mathbf{R})\Phi_q = 0. \tag{2.5}$$

The action of the operator $T_N = -\frac{\hbar^2}{2\mu}\nabla^2_R$ (here μ represents the reduced mass of the system) on the product $F_q(\mathbf{R})\Phi_q$ can be written as

$$T_N(F_q\Phi_q) = -\frac{\hbar^2}{2\mu}\left(F_q(\nabla^2_R\Phi_q) + 2(\nabla_R F_q \cdot \nabla_R\Phi_q) + \Phi_q(\nabla^2_R F_q)\right). \tag{2.6}$$

Within the Born-Oppenheimer approximation the terms including derivatives of the electronic wavefunction with respect to the nuclear coordinate are neglected. Thus, using the relation given in Eq. 2.3 and the orthonormality property of Φ_q the Eq. 2.5 uncouples and one arrives at

$$\left(-\frac{\hbar^2}{2\mu}\nabla^2_R + E_{q'}(\mathbf{R}) - E\right)F_{q'}(\mathbf{R}) = 0. \tag{2.7}$$

The nuclear wavefunction $F_{q'}(\mathbf{R})$ can be described as a vibrational part χ depending on R, and a rotational part Y depending on the polar angles θ and ϕ of the vector $\mathbf{R}$. Thus for a given state q' one can write

$$F_{q'}(\mathbf{R}) = \frac{\chi_{\nu,J}(R)}{R}Y_{J,M_J}(\theta, \phi) \tag{2.8}$$

where Y denotes the spherical harmonic functions.
For a bound electronic state, the vibrational wavefunction $\chi_{\nu,J}$ satisfies Eq. 2.7 and one obtains

$$-\frac{\hbar^2}{2\mu}\frac{d^2}{dR^2}\chi_{\nu,J} + \left(E_{q'}(R) + \frac{\hbar^2}{2\mu}\frac{J(J+1)}{R^2} - E_{q',\nu,J}\right)\chi_{\nu,J}(R) = 0, \tag{2.9}$$

in which ν and J are the vibrational and rotational quantum numbers and $E_{q'}(R)$ describes the electronic energy dependence on R and forms the so called potential energy curve (see for instance Fig. 2.1) within which the nuclei vibrate.

For $R \to 0$, $E_{q'}(R)$ is dominated by the Coulomb repulsion between the nuclei, while for $R \to \infty$, $E_{q'}(R)$ tends to a constant energy $E_{q'}(\infty)$ which is the sum of the energies of the two isolated atoms from which the molecule is composed. If there is a stable bound state $E_{q'}(R)$ will exhibit a minimum at some distance R_0.

Photodissociation cross sections

In the above section we have discussed the case were the nuclei vibrate in a bound potential well. In the case of direct photodissociation process the electronic state has no potential well or the energy regime of interest lies above the dissociation limit $E_{q'}(\infty)$ of a bound potential curve. In this case Eq. 2.9 changes to

$$-\frac{\hbar^2}{2\mu}\frac{d^2}{dR^2}\chi_{k,J} + \left(E_{q'}(R) + \frac{\hbar^2}{2\mu}\frac{J(J+1)}{R^2} - E_k\right)\chi_{k,J}(R) = 0, \tag{2.10}$$

where $E_k = \frac{k^2}{2\mu}$ is the relative kinetic energy of the dissociating atomic fragments and k is the momenta of the fragments. The continuum wavefunctions $\chi_{k,J}(R)$ behave for large internuclear distances R according to

$$\chi_{k,J}(R) \propto sin(kR + \eta), \tag{2.11}$$

where η denotes a phase shift which depends on the energy and shape of the potential [45, 49]. Assuming a dissociation process were the molecule is in a bound state Ψ_i before the dissociation and is transferred into a continuum state $\Psi_{k,f}$ where the fragments separate with the kinetic energy E_k. Thus, the cross section in the dipole approximation is proportional to [49]

$$\sigma(E_k) \propto |\langle \Psi_{k,f}|\mathbf{D}|\Psi_i\rangle|^2, \tag{2.12}$$

where $\mathbf{D}$ is the electric dipole operator given by [17]

$$\mathbf{D} = e\left(\sum_i Z_i\mathbf{R}_i - \sum_j \mathbf{r}_j\right) \tag{2.13}$$

where the first sum is over the $\mathbf{R}_i$ and charges $Z_i e$ of all the nuclei and the second sum is over the positions $\mathbf{r}_j$ of all electrons. If we further assume that the states Ψ_i and $\Psi_{k,f}$ can be described in the Born-Oppenheimer approximation and ignoring the effect of rotations, the electric dipole operator and the matrix element in Eq. 2.12 can be written as

$$\langle \Psi_{k,f}|\mathbf{D}|\Psi_i\rangle = \int \frac{1}{R^2} d\mathbf{R}\chi^*_{k,f}\mathbf{D}_{el}(R)\chi_i \tag{2.14}$$

where $\mathbf{D}_{el}(R) = \int \phi^*_f \left(\sum_j \mathbf{r}_j\right)\phi_i d\mathbf{r}$ is the electric dipole transition moment, which is usually responsible for the absorption from the initial into the final electronic state.

The direct photodissociation cross section for absorption into the vibrational continuum, given by [3, 49], can then be written as

$$\sigma(\Delta E_{k',\nu}) = \frac{2}{3}\frac{\pi e^2}{mc} g \Delta E_{k',\nu} |\langle \chi_{k',f}(R)|D_{el}(R)|\chi_{\nu,i}(R)\rangle|^2 \tag{2.15}$$

where χ is a solution of Eq. 2.10 at energy $E_{k'} = \Delta E_{k',\nu} - (E_\nu(\infty) - E_\nu)$ and g is the degeneracy factor [3].
Assuming, that the electronic transition triggered by the absorption takes place instantaneously with respect to the nuclear motion, $D_{el}(\mathbf{R})$ can be said to be independent of $\mathbf{R}$. This assumption is called the Franck-Condon principle. Hence, Eq. 2.15 can be simplified to

$$\sigma(\Delta E_{k',\nu}) = \frac{2}{3}\frac{\pi e^2}{mc} g \Delta E_{k',\nu} D_{el} f_{\nu,\nu'}, \tag{2.16}$$

with $f_{\nu,\nu'} = |\langle \chi_{k',f}(R)|\chi_{\nu,i}(R)\rangle|^2$ the Franck-Condon factor.

2.2 Experimental techniques

Several experimental techniques have been applied to study ion photofragmentation processes. All of these techniques have been used with lasers as photon sources, and in particularly favorable cases the light from incoherent sources, such as arc lamps, has been used. Most of these techniques have been successfully applied in other fields before they were applied to photodissociation studies. The most important techniques shall be briefly described here a more extensive description can be found in the review articles by Moseley [72] and Mosely and Durup [71] and in the references to individual experiments given below.

2.2.1 Gas phase and trapped ion techniques

Photodissociation cross section measurements in the gas phase have been studied using drift tube mass spectrometers by for instance Beyer et al. [11] and Moseley and co workers [73]. In these drift tubes ions are formed in the gas phase through initial electron processes and subsequent ion-molecule reactions. Under the influence of a weak electric field the molecular ions drift through the background gas towards an extraction aperture allowing them to thermalize in collisions. Before the aperture the ions are overlapped with a laser beam. Parent ions and photofragment ions are detected through some from of mass spectrometer. Dissociation cross sections can be derived through the disappearance of parent ions or the appearance of photofragments.
Photodissociation studies utilizing ion traps have been mostly applied to study larger molecular ions, for example by Freiser et al. [32]. The ions are irradiated while stored inside the trap and similar to gas phase techniques, cross sections are determined by measuring the disappearance of parent ions.

2.2.2 Fast ion beams

Although the above described techniques have been useful in the study of photofragmentation, the major development in this field has come through the application of fast ion beams. The pioneering study in this field was that of von Busch and Dunn [110] who crossed a beam of H_2^+ ions with photons from a powerful arc lamp and measured the wavelength dependence of the photodissociation cross section with a resolution of 200Å.

The first to apply lasers to the spectroscopic study of photodissociation, using fast beams of H_2^+ ions, were Ozenne et al. [77] and van Asselt and co workers [107, 106]. The application of lasers to this technique opened up many new possibilities, since the low ion density could be compensated by the higher photon densities.

The setups used for fast ion beam photodissociation by the various groups differ to a large extent. However, in general one can state that in all the different applications the molecular ions are produced in an ion source and are accelerated to the desired energy. The term "fast" ion beams thereby varies between energies of 10 to 10^5eV. The ion specie of interest is then mass selected using magnetic or quadrupole mass spectrometers. In the following interaction region the photon beam is overlapped with the ion beam in either a crossed or collinear geometry, in many experiments both possibilities were foreseen. In the early experiments of the 1970s up to the late 1980s, the charged photofragments are commonly detected using an energy analyzer. At fixed laser frequency, the energy analyzer can be scanned to measure the energy distribution of the photofragments. Making use of the amplification of the rather small center of mass dissociation energies in the laboratory frame an energy resolutions down to 10meV for the crossed geometry and 0.001meV in coaxial geometry [42] in the center of mass frame of the ion was achieved.

Since the most setups only detected photofragments ejected in the direction of the ion beam propagation, while photofragments ejected perpendicular to the ion beam were strongly suppressed, insights into the angular distribution of fragments could also be obtained assuming a good collimation of the ion and photon beam. In the crossed beams geometry the laser polarization can even be turned to obtain both parallel and perpendicular orientation with respect to the ion beam direction.

However, these described experiments have their limitations which are imposed by the finite resolution of the analyzers used to determine the photofragment energies and by the unavoidable energy spread and angular divergence in the ion beam.

With the availability of 3-dimensional imaging detectors, such as micro channel plates (MCP) (see for instance [27]), the fast ion beam technique was revolutionized. These modern detectors allow the detection of multiple charged as well as neutral particles recording the position and arrival time of each fragment.

One of the first applications of this new detection scheme was done by de Bruijn and Helm [26] in order to study the photodissociation of H_2. In their apparatus the H_2 beam was produced

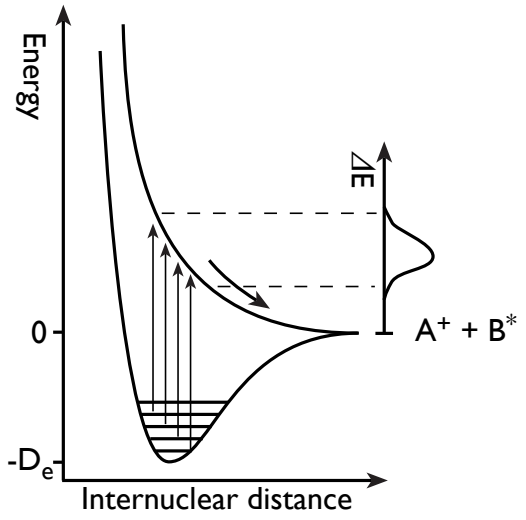

Figure 2.2: *Schematic illustration of the relation between the kinetic energy release and the internal excitation of a molecular ion.*

from a H_2^+ ion beam in a charge exchange cell. The H_2 molecules were overlapped with the laser beam in a crossed geometry. The imaging detector was mounted straight ahead of the overlap region oriented perpendicular to the ion beam direction. The main advantage of this detection scheme is that nearly all fragments can be detected with an efficiency that is in first order independent of the kinetic energy release and the ejection angel of the fragments in the center of mass frame. The energy resolution of such a system is in first approximation determined by the beam energy and the distance between the overlap region and the detector and can be on the order of 1meV [39].

2.3 The kinematics of two body breakup

To discuss the kinematics of photodissociation first the process of direct dissociation is rewritten as

$$\mathrm{AB}^+(\alpha_i) + h\nu \longrightarrow \mathrm{A}^+(\alpha_{f,A}) + \mathrm{B}^0(\alpha_{f,B}), \tag{2.17}$$

where $\mathrm{AB}^+(\alpha_i)$ represents the molecular two body system in an initial rovibronic state α_i, $h\nu$ is the photon energy, $\mathrm{A}^+(\alpha_{f,A})$ is the ionic fragment with electronic excitation $\alpha_{f,A}$ and $\mathrm{B}^0(\alpha_{f,B})$ is the neutral atomic fragment with electronic excitation $\alpha_{f,B}$. The energy balance of the dissociation process is illustrated in Fig. 2.2 and can be written as

$$\Delta E = h\nu + \mathrm{E}_{int}(\alpha_i) - \mathrm{D}_e - \mathrm{E}_{int}(\alpha_{f,A}, \alpha_{f,B}). \tag{2.18}$$

Where $\mathrm{E}_{int}(\alpha_i)$ represents the initial internal excitation of the molecular ion, D_e is the dissoci-

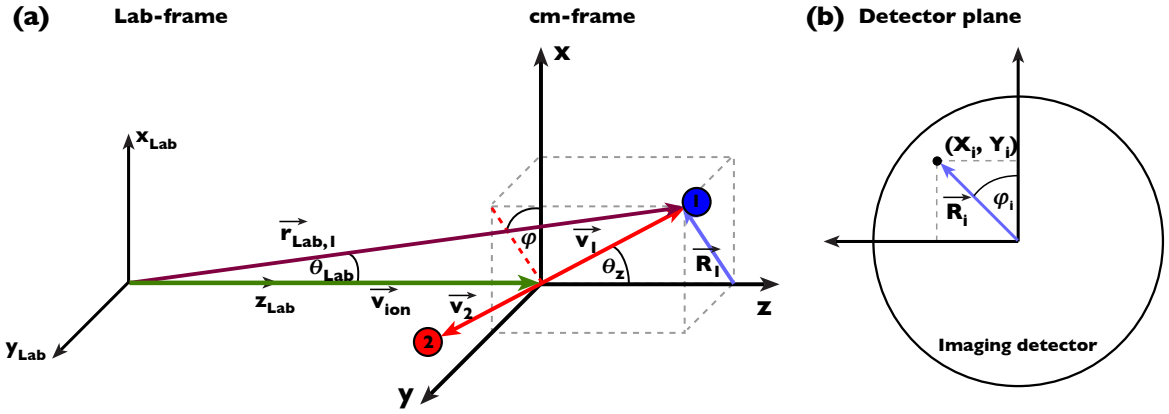

Figure 2.3: *Vectors and coordinates used to describe the breakup of a two body system. (a) Photodissociation at the interaction point in the center of mass frame of the molecule and in the laboratory frame of reference. (b) Detection of photoframgments at the imaging detector. (X,Y) is the point of impact, which is related to the polar coordinates:* $R^2 = Y^2 + X^2$ *and* $tan(\varphi) = Y/X$.

ation energy and $E_{int}(\alpha_{f,A}, \alpha_{f,B})$ denotes the internal excitation of the reaction products. The excess energy ΔE released in the dissociation process is carried away by the fragments in the form of kinetic energy. Hence, ΔE is also referred to as the kinetic energy release. Measuring the energy release in a photodissociation process can thus yield information on the initial rovibronic excitation stored in the molecular ion.

Fig. 2.3 (a) indicates the vectors and coordinates characterizing the photofragmentation process [81]. A detailed account of the kinematics of a breakup of a two body system can also be found in [83, 39].

In the laboratory frame of reference the position of a dissociation fragment is given by $\vec{r}_{Lab}$. The angel between $\vec{r}_{Lab}$ and the z_{Lab}-axis is defined as θ_{Lab}. The center of mass frame of the dissociating molecule is moving with respect to the lab-frame at the velocity $\vec{v}_{ion}$ parallel to the z_{Lab}-axis. The photofragments dissociate in the cm-frame with velocities $\vec{v}_1$ and $\vec{v}_2$. The fragment velocities and the kinetic energy release ΔE given in Eq. 2.18 are connected through

$$\Delta v = |\vec{v}_1 - \vec{v}_2| = \sqrt{\frac{2\Delta E}{\mu}}, \tag{2.19}$$

with $\mu = \frac{M_1 M_2}{M_1 + M_2}$ being the reduced mass and M_i the mass of the respective fragment.

The angel between $\vec{v}_i$ and the z-axis is defined as θ_z. φ constitutes the angle between the x-axis and the projection of $\vec{v}_i$ onto the x-y-plane.

Therefore, the velocity of a fragment in the lab-frame can be described as

$$\vec{\mathrm{v}}_{Lab,i} = \mathrm{v_{Lab,i}} \begin{pmatrix} sin(\theta_{Lab,i})cos(\varphi_i) \\ sin(\theta_{Lab,i})sin(\varphi_i) \\ cos(\theta_{Lab,i}) \end{pmatrix} \tag{2.20}$$

$$= \begin{pmatrix} 0 \\ 0 \\ \mathrm{v_{ion}} \end{pmatrix} + \mathrm{v}_i \begin{pmatrix} sin(\theta_{z,i})cos(\varphi_i) \\ sin(\theta_{z,i})sin(\varphi_i) \\ cos(\theta_{z,i}) \end{pmatrix} \tag{2.21}$$

with $\varphi_i = \varphi_{Lab,i}$ and either $\mathrm{v}_1 = \Delta\mathrm{v}\frac{\mu}{\mathrm{M}_1}$ or $\mathrm{v}_2 = -\Delta\mathrm{v}\frac{\mu}{\mathrm{M}_2}$.
A field free propagation of a photofragment (here for fragment number 1) from the interaction point to the detector along the z-axis is given by

$$\vec{\mathrm{r}}_{Lab,1} = \vec{\mathrm{v}}_{Lab,1} \cdot \mathrm{t}_{tof,1} \tag{2.22}$$

$$= \begin{pmatrix} 0 \\ 0 \\ \mathrm{v_{ion}} \end{pmatrix} \mathrm{t_{tof,1}} + \Delta\mathrm{v}\frac{\mu}{\mathrm{M}_1}\mathrm{t_{tof,1}} \begin{pmatrix} sin(\theta_{z,i})cos(\varphi) \\ sin(\theta_{z,i})sin(\varphi) \\ cos(\theta_{z,i}) \end{pmatrix} \tag{2.23}$$

$$= \begin{pmatrix} X_1 \\ Y_1 \\ L \end{pmatrix} \tag{2.24}$$

with $\mathrm{t}_{tof,1}$ being the time of flight of the particle to the detector, L being the distance between the interaction point and the detector, and X and Y the coordinates on the detector as depicted in Fig. 2.3 (b).
From there we can arrive at the following conclusion for the time of flight $\mathrm{t}_{tof,1}$

$$\mathrm{t}_{tof,1} = \frac{\mathrm{L}}{\mathrm{v_{ion}}} \cdot \frac{1}{1 + \frac{\Delta\mathrm{v}\mu}{\mathrm{v}_{ion}\mathrm{M}_1}cos(\theta_{z,1})} \tag{2.25}$$

and for $\vec{\mathrm{R}}_1$, which is the radial position on the imaging detector as illustrated in Fig. 2.3 (b), one obtains

$$\mathrm{R}_1 = \sqrt{X_1^2 + Y_1^2} \tag{2.26}$$

$$= \frac{\Delta\mathrm{v}\mu}{\mathrm{M}_1} \cdot \mathrm{t_{tof,1}} \cdot \sin(\theta_{\mathrm{z},1}) \tag{2.27}$$

$$= \frac{\Delta\mathrm{v}\mu}{\mathrm{M}_1} \cdot \sin(\theta_{\mathrm{z},1}) \cdot \frac{\mathrm{L}}{\mathrm{v_{ion}}} \cdot \frac{1}{1 + \frac{\Delta\mathrm{v}\mu}{\mathrm{v_{ion}}\mathrm{M}_1}\cos(\theta_{\mathrm{z},1})}. \tag{2.28}$$

Inversion of Eq. 2.25 and Eq. 2.27 yields a formula for the angle θ_z

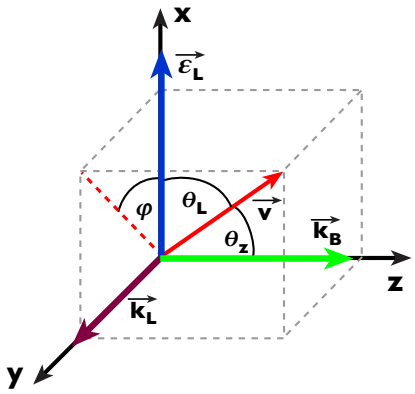

Figure 2.4: *Vectors and coordinates used to characterize the angular distribution of photodissociation fragments.*

$$\theta_{z,1} = \begin{cases} \arctan\left(\frac{\mathrm{R}_1}{\mathrm{L}-\mathrm{t}_{tof,1}\mathrm{v}_{ion}}\right) & \text{for } \mathrm{L}-\mathrm{t}_{tof,1}\mathrm{v}_{ion} > 0 \\ \pi + \arctan\left(\frac{\mathrm{R}_1}{\mathrm{L}-\mathrm{t}_{tof,1}\mathrm{v}_{ion}}\right) & \text{for } \mathrm{L}-\mathrm{t}_{tof,1}\mathrm{v}_{ion} < 0 \end{cases} \tag{2.29}$$

and for the kinetic energy release ΔE one arrives at

$$\Delta\mathrm{E} = \frac{1}{2}\mu\Delta\mathrm{v}^2 \quad = \quad \frac{1}{2}\frac{\mathrm{M}_1^2}{\mu}\frac{(\mathrm{L}-\mathrm{t}_{tof,1}\mathrm{v}_{ion})^2 + \mathrm{R}_1^2}{\mathrm{t}_{tof,1}^2}. \tag{2.30}$$

2.4 Angular distribution of photofragments

This section will give a brief overview of how the angular distribution of photofragments can be calculated from coordinates measured by an imaging detector. A more detailed account can be found in [83].

The angular distribution for photofragments, from initially randomly oriented molecules, can be written in the form

$$\mathrm{P}(\theta_L, \varphi)d\Omega_L = \frac{1}{4\pi}(1 + \beta \cdot \mathrm{P}_2(cos(\theta_L)))d\Omega_L \tag{2.31}$$

which was given by [115, 21]. Here θ_L is the angel between the laser polarization, given by $\vec{\varepsilon}_L$, and the direction of ejection of the fragments in the center of mass frame ($\vec{\mathrm{v}}$) illustrated in Fig. 2.4. $\mathrm{P}_2(cos(\theta_L)) = \frac{1}{2}(3cos^2(\theta_L) - 1)$ is the second Legendre polynomial of $cos(\theta_L)$ and β is the anisotropy parameter. $\vec{\mathrm{k}}_B$ indicates the ion beam propagation direction and $\vec{\mathrm{k}}_L$ gives the direction of the laser beam.

The anisotropy parameter is limited to values of $-1 \leq \beta \leq 2$, where $\beta = -1$ corresponds to a $sin^2(\theta_L)$ distribution, a value of $\beta = 2$ to a $cos^2(\theta_L)$ distribution, and $\beta = 0$ to an isotropic distribution.

In case of fast direct photodissociation of a diatomic molecule, β is equal to 2 if $\Delta\Lambda = 0$ which gives a parallel transition and beta is equal to -1 if $\Delta\Lambda = \pm 1$ which corresponds to a perpendicular transition. Λ thereby denotes the quantum number corresponding to the projection of the

total electronic orbital angular momentum along the internuclear axis (see for example [17]). This allows to determine the identity of the potential curves involved in the photodissociation process from the angular distribution of the photofragments.
With the solid angel $d\Omega_L$ defined by $d\Omega_L = sin(\theta_L)d\theta_L d\varphi_L$ Eq. 2.31 can be rephrased as

$$\begin{aligned} \mathrm{I}(\beta,\theta_L)d\theta_L &= \frac{1}{4\pi}\int_0^{2\pi} d\varphi(1+\beta\cdot \mathrm{P}_2(cos(\theta_L))\cdot sin(\theta_L)d\theta_L \quad (2.32)\\ &= \frac{1}{2}\left(1-\frac{\beta}{2}\right)sin(\theta_L)+\frac{3}{4}\beta cos^2(\theta_L)sin(\theta_L)d\theta_L. \quad (2.33)\end{aligned}$$

The theoretical curves for the angular distributions according to Eq. 2.33 assuming pure parallel and perpendicular transitions and assuming no rotation of the molecular ion before dissociation are displayed in Fig. 2.5.
Since the solid angel is conserved upon rotation of the coordinate system at the interaction point and using the conversion

$$cos(\theta_L) = \frac{\vec{\mathrm{v}}\cdot\vec{\varepsilon}_L}{\mathrm{v}} = sin(\theta_z)cos(\varphi)\cdot\varepsilon_x + sin(\theta_z)sin(\varphi)\cdot\varepsilon_y + cos(\theta_z)\varepsilon_z, \quad (2.34)$$

the angular distribution in terms of θ_z can be written as

$$\begin{aligned} \mathrm{I}(\beta,\theta_z)d\theta_z &= \frac{1}{4\pi}\int_0^{2\pi} d\varphi(1+\beta\cdot \mathrm{P}_2(\frac{\vec{\mathrm{v}}_1\cdot\vec{\varepsilon}_L}{\mathrm{v}_1}))\cdot sin(\theta_z)d\theta_z \quad (2.35)\\ &= \left(\frac{1}{2}\left(1-\frac{\beta}{2}\right)+\frac{3}{4}\beta cos^2(\theta_z)\cdot\varepsilon_z^2+\frac{3}{8}\beta sin^2(\theta_z)\cdot(\varepsilon_x^2+\varepsilon_y^2)\right)\cdot sin(\theta_z)d\theta_z \quad (2.36)\end{aligned}$$

2.5 Monte Carlo simulations

The angular distribution of fragments following a dissociation event was simulated. Therefore, a set of molecular ions with isotropic orientation was generated. The molecules were fragmented according to the probability distribution given in Eq. 2.31, assuming a pure parallel transition

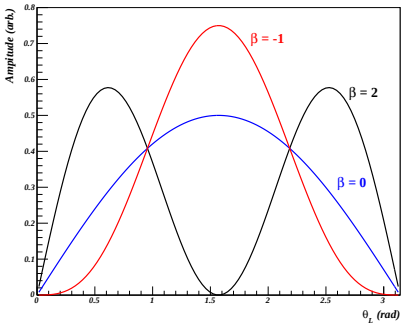

Figure 2.5: *Theoretical angular distributions of photofragments according to Eq. 2.33 for characteristic β values.*

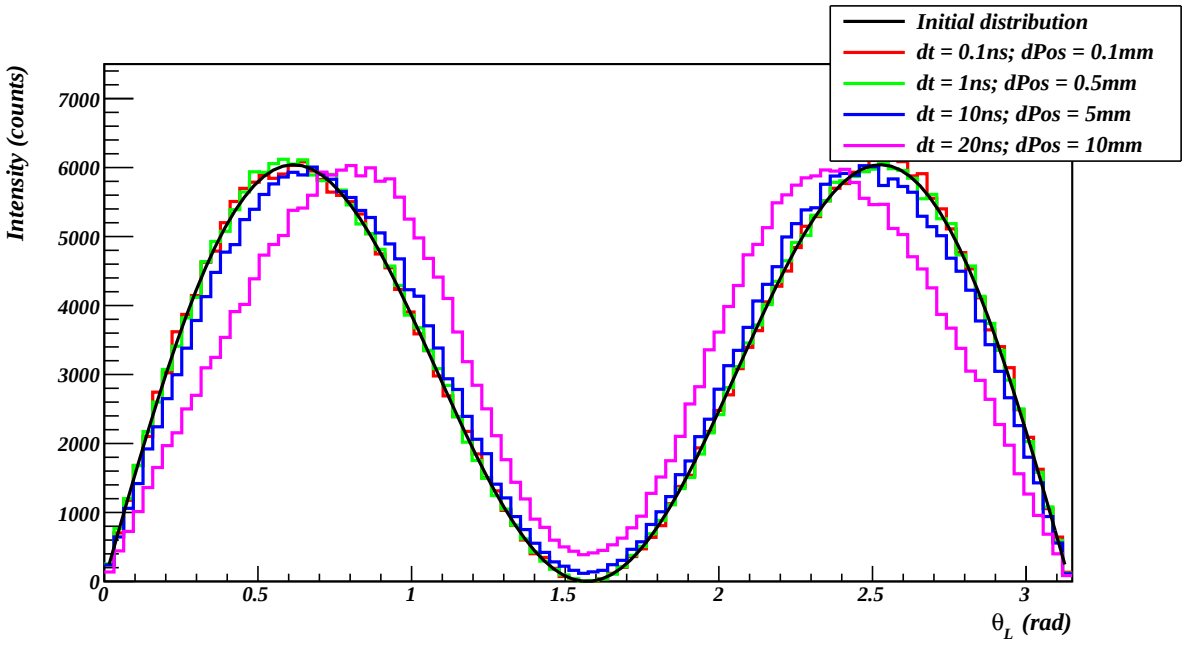

Figure 2.6: *Results of the Monte Carlo simulations assuming a purely parallel transition and taking into account different time (dt) and position (dPos) resolution.*

($\beta = 2$). The resulting photofragments were then propagated to the detector position according to Eq. 2.24 and the arrival time t_{tof} and position on the detector was recorded for each fragment. To simulate the effect of a finite position and time resolution on the angular distributions it was assumed that the coordinates and times obtained in the simulations are subject to small uncertainties which are added to the corresponding values. The uncertainties were randomly generated from a gaussian distribution with a predefined width dt for the arrival time and dPos for the X and Y position of the fragment on the detector respectively.
The results of these simulations for different values of dt and dPos are depicted in Fig. 2.6. The solid curve illustrates the initial angular distribution of the photofragments at the interaction point. In comparison with the simulated curves for finite resolution one can state that effects on the shape of the angular distribution can only be expected for very high uncertainties of both the time and the position coordinates.

3. A crossed ion beam setup for photodissociation imaging

3.1 Basic elements of the setup

In order to perform vacuum ultra-violet (VUV) photodissociation experiments on molecular ions, it was decided to setup a crossed photon and ion beam experiment. With this geometry the momenta of charged as well as neutral fragmentation products emerging from the region of interaction can be directly measured using time and position resolving particle detectors. To alleviate neutral fragment detection, the decision was taken to use fast ion beams of few keV energy. Since production and handling of ions at such energies can be done mainly using methods employing electrostatic fields. This makes the resulting setup compact and versatile. This is of particular importance since, at such large facilities as a free-electron laser, it has to be integrated into existing experimental stations. Additionally, it was decided to integrate a trapping device to allow cooling of the molecular ions or to make time-dependent studies of certain processes possible.

A schematic sketch of the experiment is shown in Fig. 3.1. Ions are created in an ion source kept at several kV potential and accelerated to a beam energy of several keV. To transport the ion beam focussing and steering units are installed along the beam line. The desired ion species is mass-selected using a dipole magnet. In the ion beam trap ions can be stored up to seconds to allow them to relax vibrationally. The ions are then extracted from the trap. To reduce the background of neutrals in the detector section the beam is bend by 90° in a quadrupole deflector, and the ion beam is focussed in the region where the photon beam and ion beam overlap. The emerging charged and neutral photofragments are detected using two imaging detectors. Light and charged fragments can be imaged on a detector close to the overlap of the two beams (Detector 2). This detector is equipped with a hole to allow the unreacted beam and heavy photofragments to pass. The beam is removed with an electrostatic deflector and the neutral fragments are detected on a second imaging detector situated further downstream.

This chapter will describe in detail the experimental setup sketched in this section, including the utilized light sources. The experimental results characterizing the performance of the experimental setup are presented in Ch. 4.

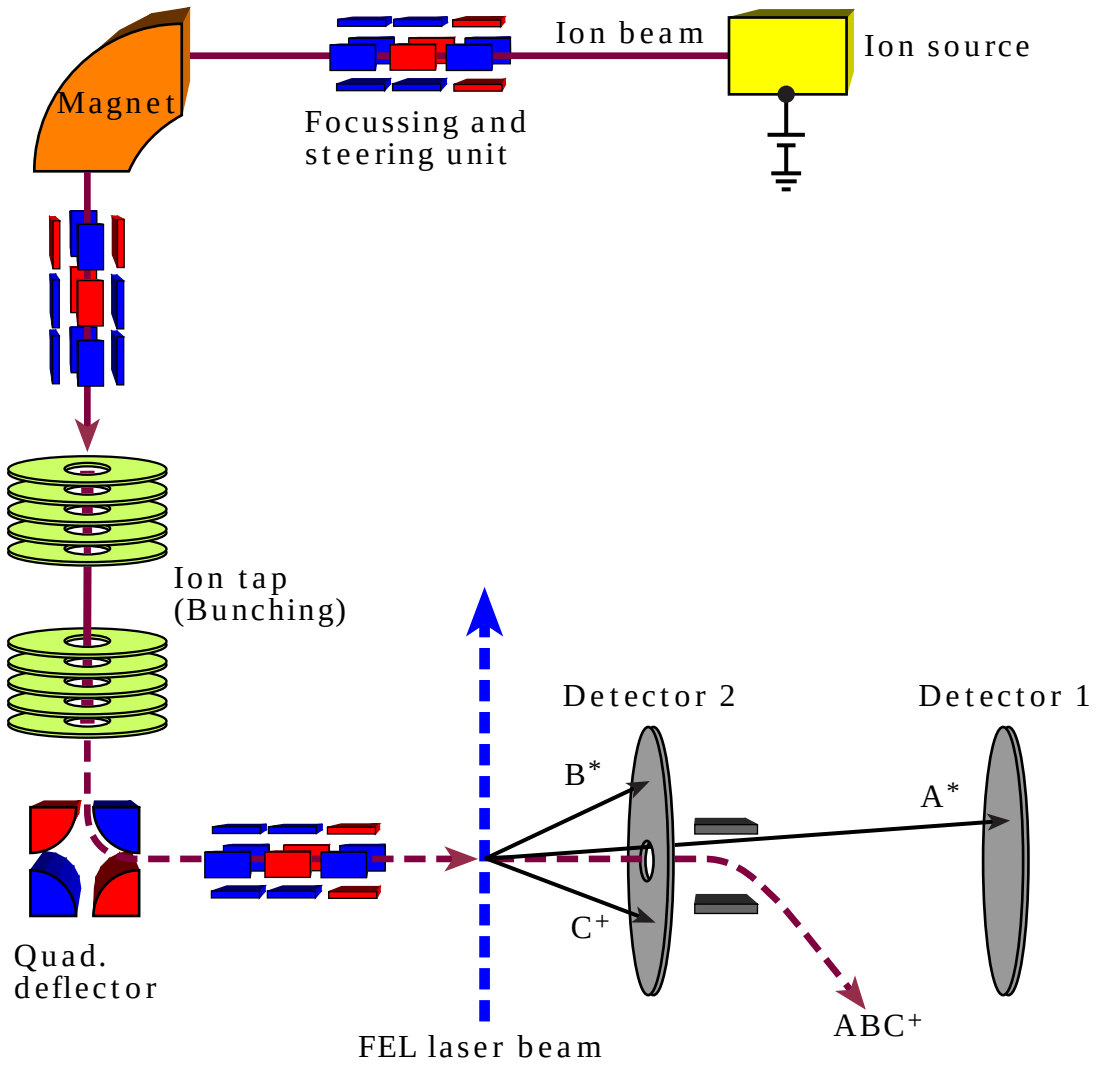

Figure 3.1: *General idea of a crossed beam photofragment imaging setup crossing cold molecular ions with VUV photons from a free-electron laser.*

In the photodissociation experiments conducted with this setup which are described in Ch. 5 and Ch. 6 only one detector situated away from the overlap region (here Detector 1) was available. Thus, emphasize was at first put on the heavy neutral fragments produced in photodissociation reactions. However, the detector with a hole has been installed and tested in the end of February 2007 and first experiments making use of this new detector will soon take place.

3.2 The Trapped Ion Fragmentation setup at FLASH (TIFF)

3.2.1 Historic development

Photodissociation imaging experiments with the setup described in this work were done in two distinct phases. In the preparation phase, mainly conducted at the Max-Planck-Institut für Kernphysik in Heidelberg, the experiment was set up and commissioned. Also first test experiments with an optical laser system on rare gas dimer ions namely Ar_2^+ and Ne_2^+ could be carried out. The results of these experiments can be found in Ch. 5.
In the second phase the experiments with vacuum-ultra-violet (VUV) photons were conducted. The complete setup was moved to the free-electron laser in Hamburg (FLASH, see Ch. 3.7.2) situated at Deutsches Elektronen-Synchrotron (DESY) that began user operation in 2005. The installation of the setup in Hamburg was carried out in October 2005 with first experiments starting in November 2005. The results of these experiments are described in Ch. 6.
Changes were necessary to adapt the experiment to the environment at the free-electron laser. Since the FEL beam height at the plane grating monochromator beamline (PG2), at which this experiment is permanently installed, is at approximately 2.60m, a large part of the experiment had to be transfered to that height and an additional upcoupling section for the ion beam was added. To facilitate the description of the setup emphasize will be put on the current status and the changes and developments the setup did undergo will be discussed briefly. Where it is necessary for the understanding of experimental results the different stages will be covered in detail.

3.2.2 Beamline setup

A complete technical drawing of the current status of the setup is displayed in Fig. 3.2 and a picture of the installation at the free-electron laser is depicted in Fig. 3.3.
The TIFF experiment can be divided into distinct functional segments. The first segment contains the ion source and the mass selecting magnet. The second segment includes the ion beam trap followed by the overlap region between photon and ion beam, and the final section contains the imaging detector. Each segment includes focussing lenses, steerer units, deflectors, apertures and a chopper unit to influence and control the ion beam. Beam diagnostics is done using Faraday cups, pickups and MCP detectors.

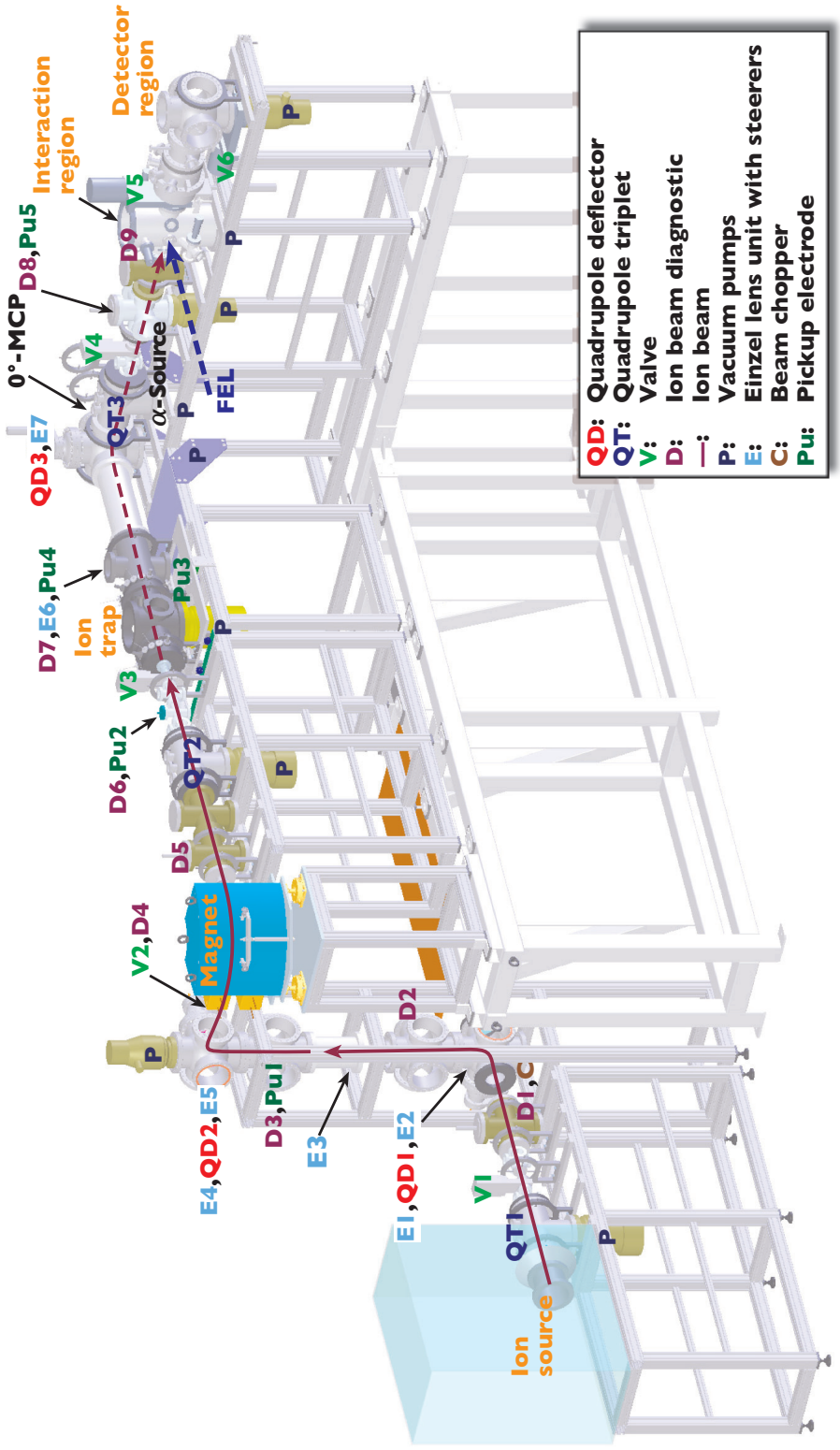

Figure 3.2: *Technical drawing of the TIFF installation at the free-electron laser in Hamburg (FLASH).*

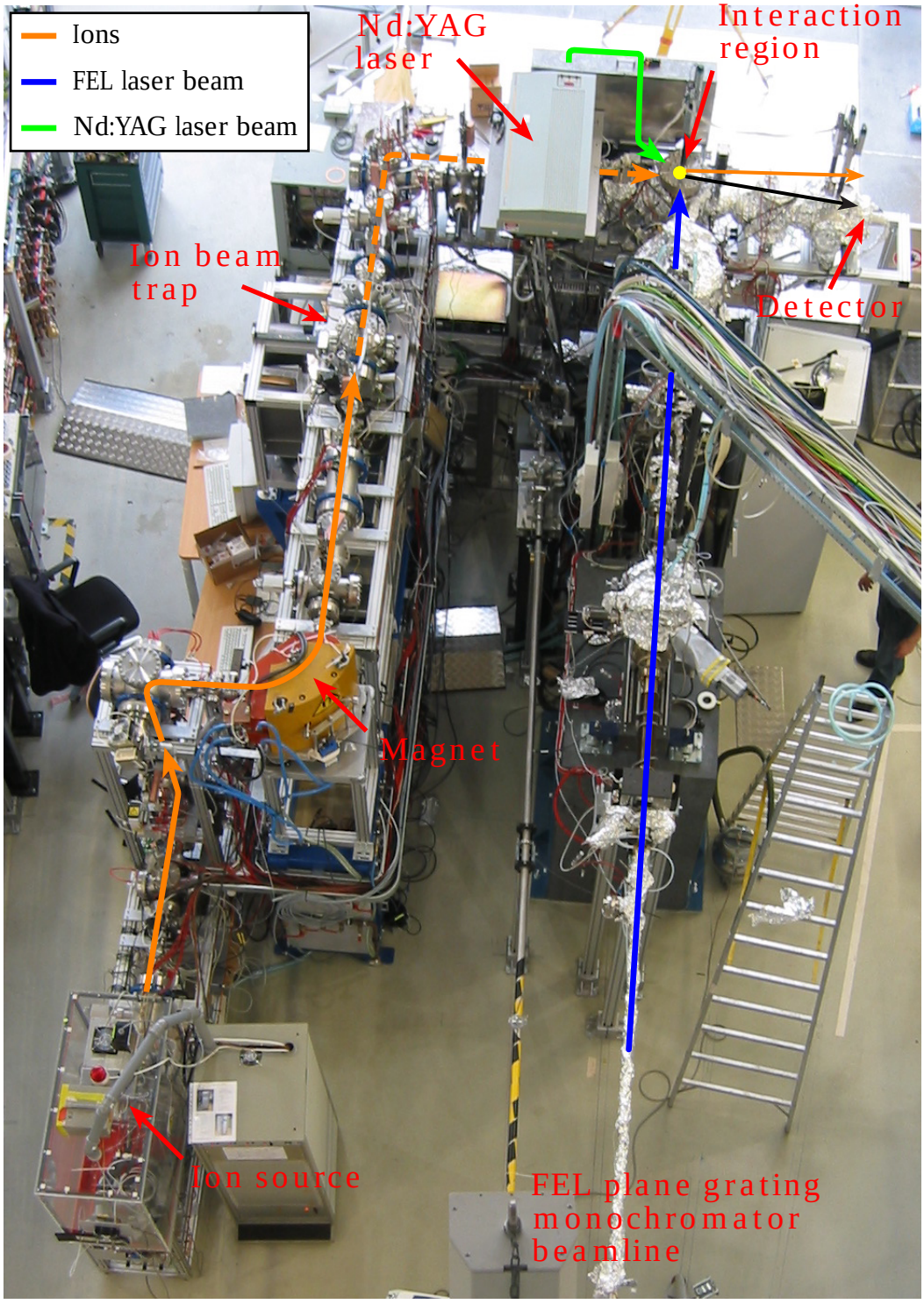

Figure 3.3: *Picture of the TIFF installation at the free-electron laser in Hamburg (FLASH).*

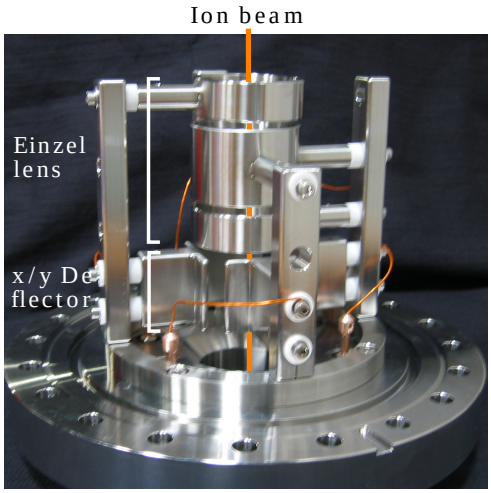

Figure 3.4: *Picture of an Einzel lens unit. The upper part shows the actual Einzel lens electrode (center) and the two upper and lower grounded electrodes. The x/y deflector contains four plates mounted in a rectangular fashion. Each set of opposing plates is used for vertical or horizontal steering of the ion beam. The ion beam passes through each element on the indicated trajectory.*

The beam of molecular or atomic ions is produced in the ion source. After it has been accelerated upon leaving the source the ion beam enters into the first quadrupole triplet (QT1) which matches the focussing to the first quadrupole deflector (QD1). The deflector bends the beam by 90° in the upward direction. After being transported to the correct FEL beam height the beam is flipped back into the horizontal plane by QD2. In the 90° dipole magnet the ions are mass selected. About 50cm before the trap the ion beam passes through the second quadrupole triplet (QT2). QT2 allows matching the ion beam to the acceptance of the ion beam trap. When the ion beam leaves the ion trap it enters QD3 and is bend by 90° so it now runs perpendicular to the photon beam coming from the free-electron laser. Via the third quadrupole triplet (QT3) the beam is focused in the interaction region and brought to overlap with the photon beam. For more details about the processing of the beam in the interaction region and in the detector region following after that please see Ch. 3.5.

3.2.3 Ion beam transport

At the beamline, two types of devices are used to focus and steer the beam. The first type is a combination of an Einzel lens and a set of horizontal and vertical deflection plates. An example is displayed in Fig. 3.4. The second type is a unit composed of three electrostatic quadrupoles, a so called quadrupole triplet. The electrodes of each quadrupole are placed above, below, left and right of the ion beam with the electrode surfaces oriented parallel to the beam as indicated in Fig. 3.5. The quadrupole units are mounted inside a DN160CF 3-way cross. The overall length of the complete triplet is 30cm. Each individual electrode is 75mm in length and 52mm wide. The profile of each electrode is semicircular with a maximum thickness of 30mm.
In each quadrupole module opposing electrodes have the same polarity while neighboring electrodes have opposite polarity. Therefore, each quadrupole element produces a focus in either the x- or y-plane. The lower part of Fig. 3.5 shows the electrical connections to each electrode.

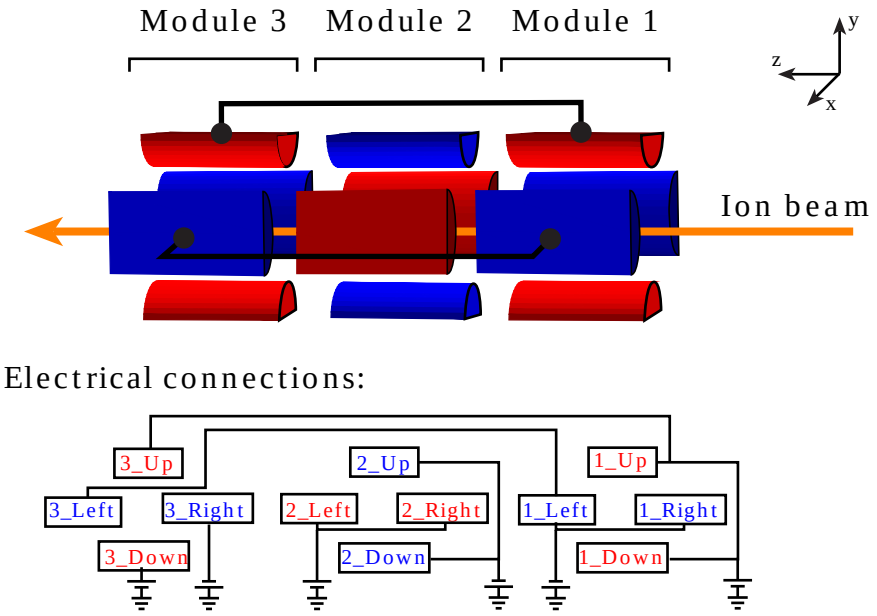

Figure 3.5: *Schematic drawing of the quadrupole triplet and a sketch of the electrical connections to each individual electrode.*

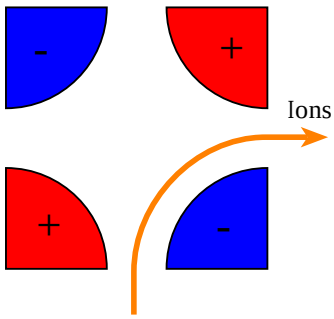

Figure 3.6: *Cut through view of the quadrupole deflector unit. The ion beam entering from below is bend by 90° if the electrode potential is of the order of the beam energy.*

Assuming a beam of positively charged ions, the focus in x direction is achieved by module 2. Due to the interconnection of module 1 and module 3 the focus in the y direction is split up between these two modules. In the case of negatively charged ions the focal planes are reversed. In module 3 the electrode situated below the ion beam and the electrode to the right of the ion beam are independent of the interconnection to module 1. These electrodes can be set slightly higher or lower than the respective opposing electrode effectively producing a small potential gradient in either the x- or y-plane which is used to steer the beam.
For 90° deflection of the beam in the upcoupling section as well as after the ion beam trap another type of electrostatic quadrupole is used. In this case the electrodes are oriented so that the surfaces are perpendicular to the ion beam (see Fig. 3.6) producing a transverse quadrupole field. Two opposing electrodes have the same polarity while neighboring electrodes have opposite polarity. If the ion beam enters such a quadrupole between the frontmost two electrodes and the potential of each electrode is on the order of the beam energy (i.e. 4.2kV in our case) the beam is bend by 90° and leaves between the two rightmost electrodes. The quadrupole deflector has strong defocussing effects on the ion beam therefore each quadrupole deflector is vested with two Einzel lens units of the type displayed in Fig. 3.4. The Einzel lens units are mounted on DN160CF flanges and are directly installed on the 6-way crosses that houses the quadrupole deflector.

3.2.4 Ion beam diagnostic

Every functional segment of the setup contains ion beam diagnostic units installed in between the focussing elements along the beam pipe. Each unit consists of a small Faraday cup with 5mm diameter and apertures of 1, 3 and 5mm. Each Faraday cup is enclosed by a grounded housing with a 5mm opening facing the ion beam. The ion beam current signal delivered by the cup is connected to the outside of the vacuum chamber via a BNC feedthrough. The signal line coming from each Farady cup is connected to a switching unit where each channel can be electronically selected for display on a picoamperemeter (Keithley Model 414A Picoammeter). The active Faraday cup is coupled to a battery which biases the cup to -100V while the inactive cups remain grounded. Each diagnostic unit is positioned on a linear motion feedthrough, and

can be moved to different positions or retracted from the beam pipe completely.
For non-destructive detection of ion pulses several pickup electrodes are mounted in the center of the beam pipe. The pickup electrodes consist of a small metal ring with a diameter of 3cm and a thickness of 0.6cm. Each pickup is connected to a BNC feedthrough passing the signal to the outside of the vacuum chamber. The ion bunch passing through the ring produces a mirror charge on the electrode which can be amplified using a charge sensitive amplifier. A recording of these bunches utilizing a scope is displayed in Ch. 4.3.2.
To diagnose the transverse beam profile two MCP detectors are installed. These MCPs are equippped with phosphor screens and are monitored using CCD cameras. Each MCP detector is attached to a motion feedthrough and can be removed from the beam pipe. One is installed in the interaction region and the second one is mounted just before the imaging detector (see also Ch. 3.5).
To monitor the stored ion beam inside the ion beam trap a 40mm MCP detector (0°-MCP) situated just after QD3 approximately 60cm downstream from the exit mirror of the ion trap. The third quadrupole deflector is therefore mounted on a translation stage so it can be removed from the beam pipe to prevent it from blocking the detector.

3.2.5 Ion beam pulsing

To produce a pulsed ion beam two posiblities have been used at the beamlines. It is possible to either use the longitudinal pulsing capabilities of the ion beam trap or a transverse chopper unit which is installed about 50cm downstream from the ion source. The transverse ion beam chopper unit consists of two short electrodes with a width of 4cm and a length 2cm. These electrodes are mounted inside the beam pipe about 1.5cm apart so that the ion beam can pass between the two plates. One side of the chopper is grounded and the other electrode is connected to a fast HV push-pull switch, which can switch the high potential to ground and vice versa in about 200ns. At a beam energy of 4.2keV a setting of higher than 3000V was found to be sufficient, to deflect the ion beam onto the walls of the vacuum chamber.

3.2.6 The vacuum system

The vacuum system of the setup is divided into six distinct segments. As can be taken from Fig. 3.2 valves are placed along the beam pipe so that the different segments can be separated from each other to facilitate maintenance work and to protect against accidental vacuum leaks. The first segment contains the ion source and the first quadrupole triplet and is pumped by a 500l/s turbo pump (Varian Navigator TV551) situated below QT1. Under typical operating conditions the pressure is on the order of $5 \cdot 10^{-7}$mbar to $2 \cdot 10^{-5}$mbar depending on the source inside pressure. To allow for differential pumping the beam pipe diameter is reduced to 40mm in a 40cm section installed after QT1 which also contains the valve (V1).

The following segment number two contains the two quadrupole deflectors installed in the up-coupling section and is pumped by a 250l/s turbo pump (Varian Navigator TV301) situated on top of QD2. Normal operating pressure is on the order of 10^{-6}mbar. In the section containing the valve (V2), between QD2 and the magnet, the pipe diameter is reduced to 40mm. Together with the magnet vacuum chamber this serves as a second differential pumping section.
The next segment includes the magnet, the quadrupole triplet number two (QT2) and another differential pumping section between triplet and the ion beam trap. The vacuum is provided by a second 500l/s turbo pump installed below QT2. Under normal operating conditions the inside pressure ranges from $5 \cdot 10^{-9}$mbar to $2 \cdot 10^{-8}$mbar.
The fourth segment comprises the ion beam trap, the third quadrupole deflector (QD3) as well as the third quadrupole triplet unit (QT3). Vacuum in this segment is provided by two cryo pumps and a second 250l/s turbo pump. The cryo pumps are installed beneath the ion beam trap and below the quadrupole deflector while the turbo pump is mounted underneath the quadrupole triplet. Upon normal operation the vacuum inside the ion beam trap is between $8 \cdot 10^{-10}$mbar and $4 \cdot 10^{-9}$mbar while the pressure outside the trap is typically on the order of $8 \cdot 10^{-9}$mbar. A fourth differential pumping section is installed after QT3 containing valve number four (V4).
The fifth segment contains the interaction region. This segment is pumped by a 50l/s ion pump (Varian model VacIon Plus 55) installed underneath a vacuum chamber before the interaction region and a NEG getter pump (Saes SORB-AC cartridge pump) situated below the interaction region. This yields an inside pressure upon operation of up to $4 \cdot 10^{-9}$mbar.
The last segment is separated from segment number five by a valve with a size of 100mm (V5) and contains the imaging detector. It is pumped by a third 250l/s turbo pump installed below the detector chamber. The turbo pump can be segregated from the chamber by a 100mm valve (V6) mounted between chamber and pump. Under normal operating conditions the vacuum in the detector chamber is at the same level as in segment five.
The last two segments, namely interaction region and the detector section, are baked at 150°C for more than 24 hours.
To measure the inside pressure of the vacuum chambers each segment contains one full range vacuum gauge (Leybold IONIVAC ITR 90) which can indicate pressures ranging form $5 \cdot 10^{-10}$mbar to atmospheric pressure. For measurement of ultra high vacuum two extractor gauges (Leybold IONIVAC IE 514) are installed at the chamber of the ion beam trap and the vacuum chamber housing the interaction region. These allow pressure determination down to $1 \cdot 10^{-12}$mbar.

3.3 The hollow cathode ion source

The ion source in use is a hollow cathode type source that was previously used for production of cold H_3^+ [5]. A picture of the complete source is displayed on the left of Fig. 3.7.
Ions are extracted from the negative glow of a self-sustained discharge [88] burning in a gas

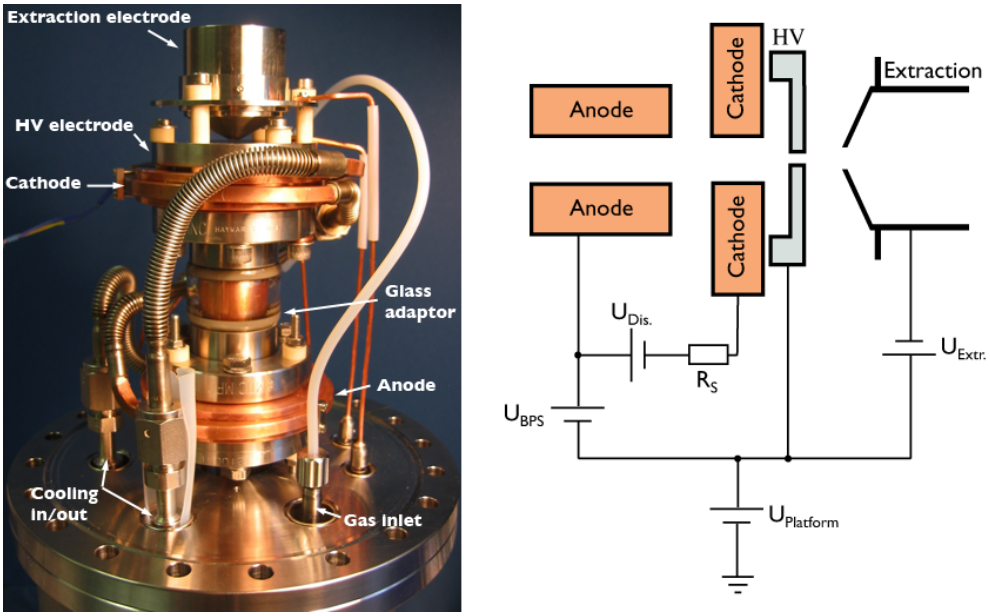

Figure 3.7: *The hollow cathode ion source and a schematic diagram of the electrical wiring.*

$U_{Platform}$	4200V
U_{BPS}	≈100V
I_{BPS}	5-8mA
$U_{Dis.}$	250-400V
$I_{Dis.}$	45mA
$U_{Extr.}$	-3000V
p_{source}	0.1-1.0mbar

Table 3.1: *Typical ion source settings.*

between a hollow cathode and a hollow anode.

The anode and cathode electrodes are isolated against each other by the glass adaptor. Together with a window (below the anode in the picture) and the bias electrode they form an enclosed volume with only a small opening in the bias electrode. The diameter of the opening can be varied between 0.2-1.0mm by exchanging a small disc held in place by the HV electrode. The anode is extended on the inside of the glass adaptor by a copper cylinder with an inside diameter of about 1cm reaching almost all the way to the cathode forming one hollow anode structure. A cup like extraction electrode is mounted on top of the ion source electrically insulated from the remaining electrodes by ceramic tubes as displayed in Fig. 3.7.

The electrical wiring diagram of the source is displayed on the right side of Fig. 3.7. The source is mounted on a high voltage platform and is electrically insulated from the rest of the beam pipe by a piece of tubing made from plexiglas. The discharge is driven by $U_{Dis.}$ with the series resistor $R_S = 10 - 40k\Omega$ serving as a spark protection. Anode and cathode can be moved up and down potential wise by U_{BPS}. Typical settings for all voltages can be taken from Tab. 3.1. To a good approximation the platform voltage $U_{Platform}$ defines the potential on which the ions are created and thus their kinetic energy after extraction from the source. The extraction electrode potential is lower than the platform voltage producing a steep field gradient at the exit of the ion source which accelerates the ions when leaving the source.

Via U_{BPS} the negative glow region of the discharge situated inside the hollow cathode can be adjusted slightly higher than the potential of the HV electrode to produce a small drift field inside the source. Pulled by this drift field the ions leave the ion source through the opening inside the HV electrode and are then accelerated by the strong extraction field imposed by the extraction electrode. When leaving the extraction electrode the ions are further accelerated to ground potential until they reach the final beam energy of typically 4.2keV.

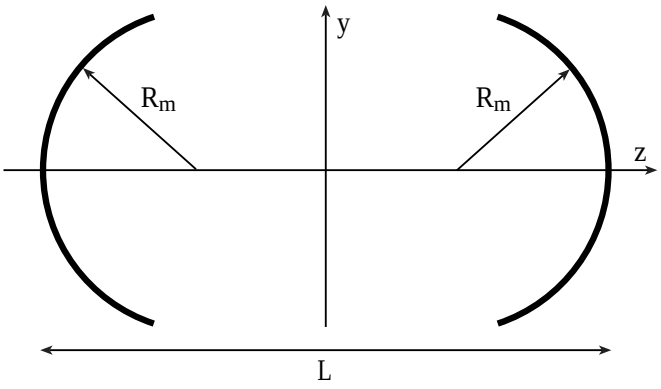

Figure 3.8: *Model of an optical resonator consisting of two concave mirrors with radius of curvature R_m. Such a resonator is used as an analogy for the ion beam trap. The focal length of a concave mirror is defined as $f_m = \frac{R_m}{2}$ as can be taken from [55, 65].*

3.4 The ion beam trap

3.4.1 An electrostatic ion trap

As trapping device for the ion beam an electrostatic ion trap device invented by Zajfman et al. [114] is used. A description of the trap assembly can also be found in [24].
In an optical resonator, as illustrated in Fig. 3.8, a beam of light is trapped between two concave mirrors, if certain conditions relating to the length of the resonator and the focus length of the mirrors are fulfilled. The laws of geometrical optics can be directly applied to the motion of charged particles in an electromagnetic fields with the difference that the index of refraction becomes a continuous function of space [102]. If only electrostatic fields are present the index of refraction is proportional to the square root of the electric potential. Thus, it is possible to construct an ion trapping device based on the principle of an optical resonator, utilizing ion mirrors. Such ion mirrors can be designed using either magnetostatic [87] or electrostatic fields. However, an electrostatic design offers the advantage of having no limit on the mass of the trapped particles.

3.4.2 Trap stability criteria

The stability of the ion trap can be divided into two parts: longitudinal and radial confinement. The longitudinal confinement of ions inside the trap is achieved if the confining potential V_s generated by the mirrors is high enough to stop the ions, i.e.,

$$V_s > \frac{E_{kin}}{q}; \tag{3.1}$$

where E_{kin} is the kinetic energy of the ions and q is their charge.
Exploiting the analogy to light propagation the radial stability criteria can be directly derived from (ABCD)-matrix calculations developed in geometrical optics (see for example [113]). It is given by

$$0 \leq (1 - \frac{\mathrm{L}}{\mathrm{R}_1}) \cdot (1 - \frac{\mathrm{L}}{\mathrm{R}_2}) \leq 1 \tag{3.2}$$

with L being the length of the resonator and R_1 and R_2 the radii of curvature of the two mirrors. Using the definition of the focal length $f = \frac{\mathrm{R}}{2}$ and assuming a symmetric resonator ($\mathrm{R}_1 = \mathrm{R}_2$) one obtains the simple relation

$$\frac{\mathrm{L}}{4} \leq f \leq \infty. \tag{3.3}$$

3.4.3 Ion trap mechanical construction

Fig. 3.9 shows a picture of the ion beam trap. The trap consists of two cylindrical-symmetric electrostatic mirrors made up of seven mirror electrodes labeled M0–M6. The electrode M1 holds a small cylindrical insert which extents from M1 all the way to the inside of electrode M2 depicted in the enlarged section shown in the lower part of Fig. 3.9. Two additional focussing electrodes Z0 and Z1 are added to the each stack of mirror electrodes.
All trap electrodes are made from 304 stainless steel and are mounted using ceramic balls which ensure precise alignment of all parts and, provide the electrical insulation of the electrodes. The two sets of mirror electrodes are interconnected by four rods and are coaxially oriented. An additional Einzel lens is mounted just after the exit mirror followed by a set of vertical and horizontal deflection plates. The complete assembly is mounted on a double sided DN160CF flange (visible in the picture contained in Fig 3.9) and can be inserted into the vacuum chamber from one side. A second double sided flange supports the exit mirror at the other end of the vacuum chamber.
The overall length of a mirror including the Einzel lens electrodes Z1 and Z0 is 103mm with a diameter of 93mm. The field free region between both mirrors has a length of 227mm. This results in a complete length of the trap assembly of 433mm. If the additional focussing and steering electrodes mounted after the exit mirror are also taken into account the total length of the complete assembly rises to 620mm. More detailed dimensions can be found in Fig. 3.9.
Electrical connections to all electrodes is achieved using stainless steel wires. These wires are spot welded to each electrode and then guided to electrical feedthroughs mounted on the double sided flanges. The interconnection between the wires and the electrical feedthroughs is done with removable push-on connectors.

3.4.4 Electrostatic mirrors

The focal properties of the trap mirrors were modeled with the help of SIMION [25]. The program SIMION can both solve the Laplace equation for a specific potential configuration in space as well as propagate ions on the computed potential grid. The program uses a fourth order Runge-Kutta method to solve the Newtonian equation of motion.

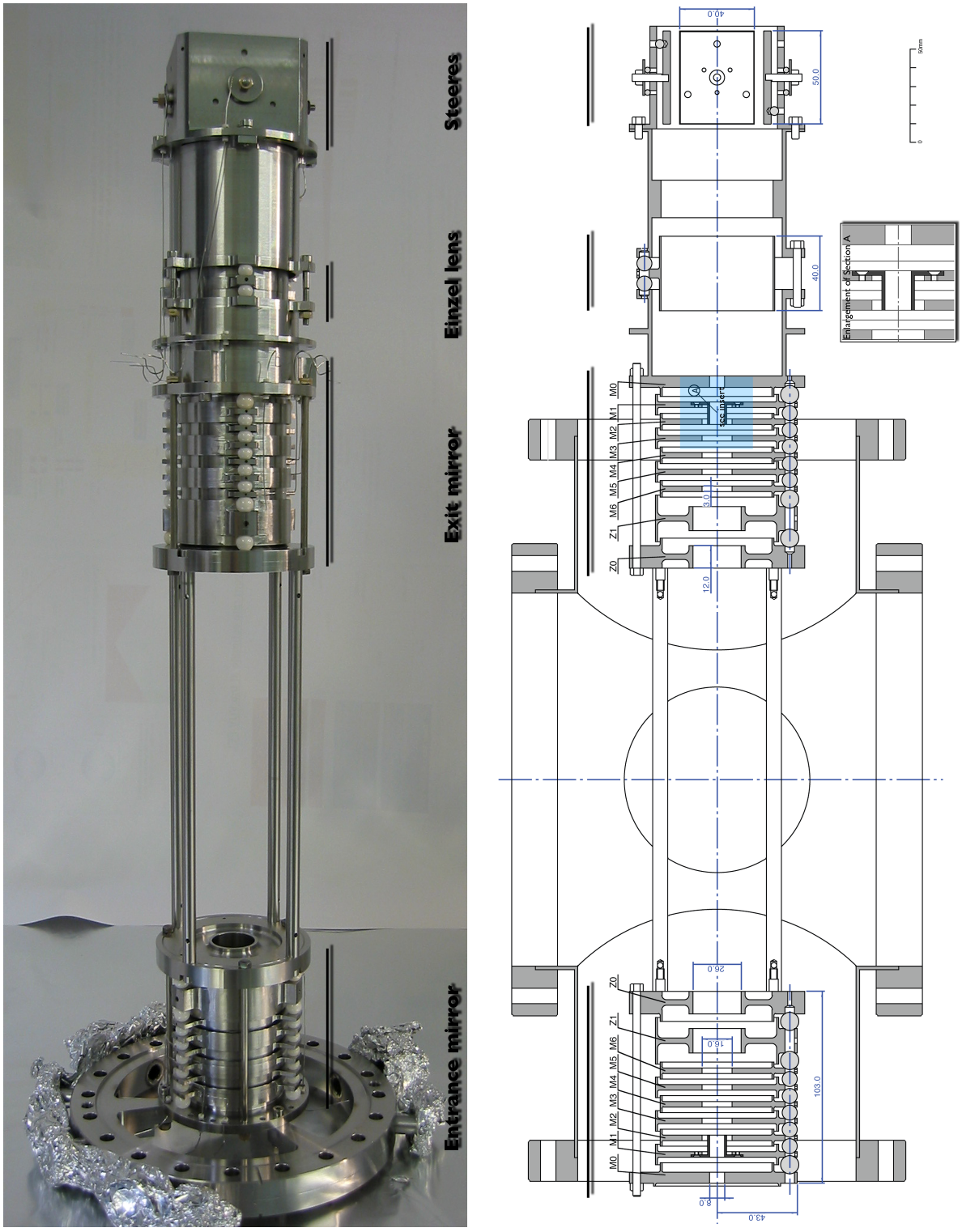

Figure 3.9: *Overview of the ion beam trap assembly.*

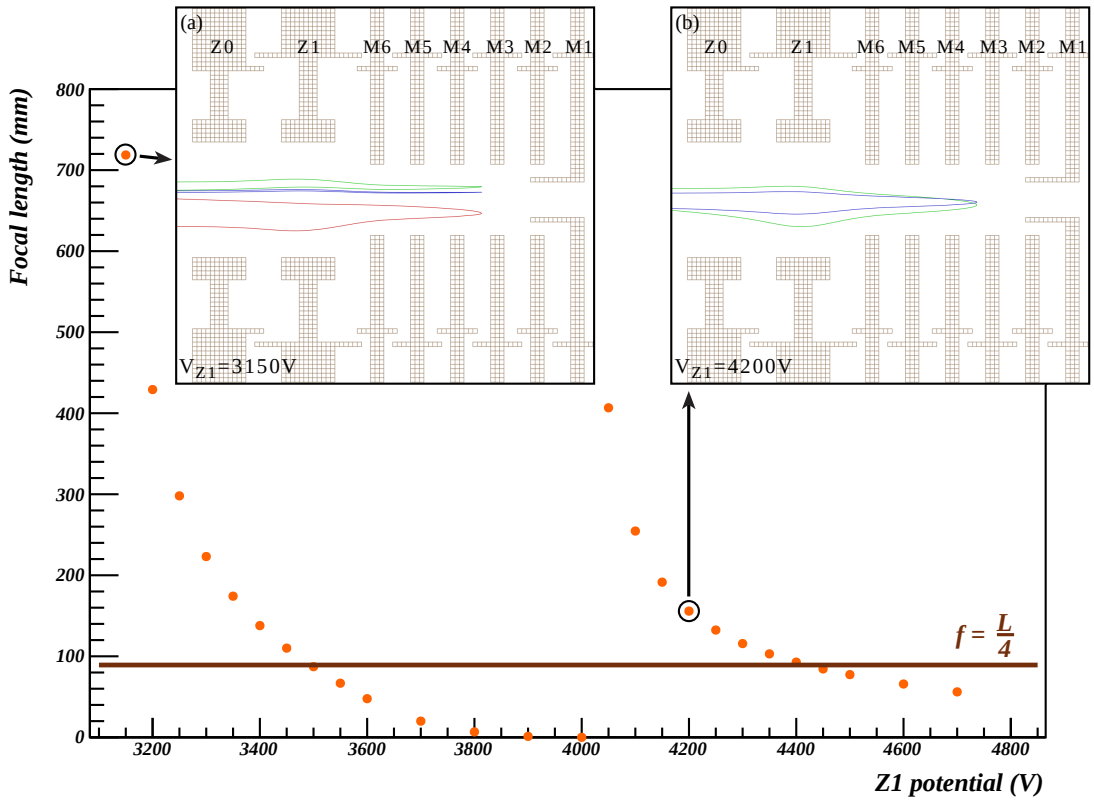

Figure 3.10: *SIMION simulations of the focal length versus the potential of the Einzel lens electrode Z1 for Ar^+ ions with 4.2keV kinetic energy. The inserts show the simulations of ion trajectories inside the trap mirror for two exemplary voltage settings, (a) corresponds to $V_{Z1} = 3150V$ and (b) $V_{Z1} = 4200V$. The settings for the remaining mirror electrodes were $V_{M5} = 1625V$, $V_{M4} = 3250V$, $V_{M3} = 4875V$, $V_{M2} = 6500V$ and $V_{M1} = 5700V$, all electrodes not mentioned were grounded.*

The geometry files describing the ion trap assembly needed for the simulations were kindly provided by [79]. An example of these simulations using a particular set of electrode potentials is shown in Fig. 3.10. The potential of the Einzel lens electrode Z1 was varied between $V_{M2} = 3100 - 4700V$. The focal length of each setting was than determined by trajectory simulations of Ar^+ ions with 4.2keV beam energy initially moving parallel to the axis of symmetry (z-axis, compare with Fig. 3.8). By comparing the turn around points inside the mirror z_m with the point where the ion crosses the axis of symmetry after being reflected z_c the focal length f could be calculated by $f = z_m - z_c$. To account for aberrations of the mirror these calculations were performed for a small group of ions where the distance y from the z-axis changed for each ion ranging from 0-1.5mm. From the results obtained from this group of ions an average focal length was then calculated.
It was found in the simulations that the length of the trap $L = 2z_m$ is independent of the value of V_{Z1}, i.e. the value of z_m is defined by the settings of the mirror electrodes M1–M5. Hence L was assumed to be constant with a value of L = 357mm.
Fig. 3.10 shows the relation between the Einzel lens voltage V_{Z1} and the focal length. The lower limit of the stability criteria Eq. 3.3 is indicated by a horizontal line. For different values of V_{Z1} similar focal properties can be obtained leading to a division into two distinct regions of stability: a region reaching from $3100V \lesssim V_{Z1} \lesssim 3500V$ and a region of V_{Z1} extending from $4050V \lesssim V_{Z1} \lesssim 4450V$. The simulated trajectories for $V_{Z1} = 3150V$ and $V_{Z1} = 4200V$ depicted in Fig. 3.10 (a) and (b) show that the behavior of the ions inside the mirror clearly changes in the two stability regions. For $V_{Z1} = 3150V$, which exemplifies the lower lying region, different trajectories with various distance y from the z-axis have turning points inside the mirror that are distributed radially, while in the case of $V_{Z1} = 4200V$ trajectories focus close to the z-axis.

3.4.5 Ion trap operation

For trap operation the M1 electrodes of each mirror are set to a potential V_{M1} which is high enough to stop the ions (compare to Eq. 3.1) for 4.2keV ions a value of $V_{M1} = 4600V$ is used. In most cases the potential V_{M1} is then divided linearly among the electrodes M2–M5, although different partitions are possible. This produces a retarding field with variable field gradient in direction of the M1 electrode. The M6 electrode is grounded as well as M0 which closes the stack and reduces the electric field outside of the ion trap. The last electrode (Z0) is grounded and closes the stack to the inside of the ion trap thus making the region between the two mirrors field free. The Einzel lens electrode Z1 focuses the ion beam and is usually set to a potential ranging between 3200-4800V depending on trapping conditions as discussed in Ch. 3.4.4.
The power supplies (up to 10kV for the Einzel lenses and mirror electrodes) are connected through a set of fast HV switches (Behlke, series HTS) to each electrode. The HV switches allow raising or dropping the voltages of each mirror with rise or fall times of around 100ns.
To facilitate injection and extraction of ions into or from the trap the electrode M1 was given a

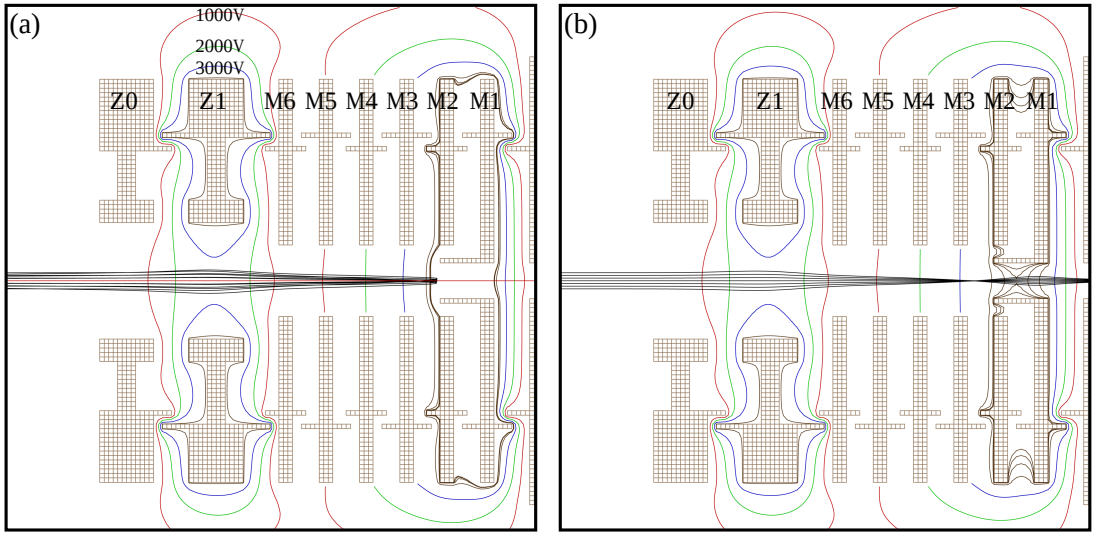

Figure 3.11: *SIMION simulations of one of the trap mirrors. The lines indicate equipotential surfaces with the following color coding red = 1000V, green = 2000V, blue = 3000V and brown corresponds to multiple potentials between 3900-4000V. In order to illustrate the behavior of ions inside the mirror simulations of Ar^+ ions at 4.2keV were carried out. The resulting trajectories are indicated by the black lines. The trap settings were $V_{Z1} = 3900V$, $V_{M5} = 1000V$, $V_{M4} = 2000V$, $V_{M3} = 3000V$, $V_{M2} = 4000V$, $V_{M1} = 4600V$ for (a) and $V_{M1} = 4000V$ for (b), all other electrodes were grounded.*

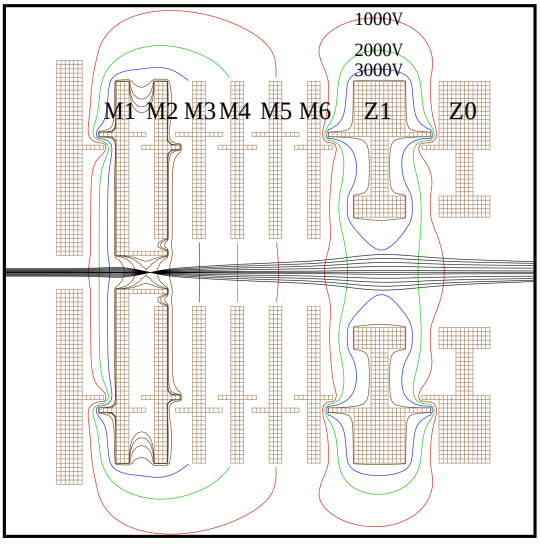

Figure 3.12: *SIMION simulations of injection into the trap through one of the trap mirrors. The lines indicate equipotential surfaces with the following color coding red = 1000V, green = 2000V, blue = 3000V and brown corresponds to multiple potentials between 3900-4000V. An injected beam of Ar^+ ions at 4.2keV was simulated and the resulting trajectories are displayed by the black lines. The trap settings were $V_{M1} = 4000V$, $V_{M2} = 4000V$, $V_{M3} = 3000V$, $V_{M4} = 2000V$, $V_{M5} = 1000V$ and $V_{Z1} = 3900V$, all other electrodes were grounded.*

special shape using a cylindrical insert. By lowering the potential of this electrode, it is possible to produce a hole inside the mirror through which ions can pass into or out of the trap. The effect of this electrode is illustrated with the simulations shown in Fig. 3.11 and Fig. 3.12.

The calculations show the obtained equipotential surfaces indicated by lines of the same color. Fig. 3.11 (a) displays the result for a configuration with M1 at high potential, here $V_{M1} = 4600V$. In Fig. 3.11 (b) the M1 potential is then lowered to $V_{M1} = 4000V$ resulting in an open channel inside the electrode indicated by the equipotential lines adjacent to M1.

Trajectory simulations of a set of Ar^+ ions at an energy of 4.2keV were also carried out to illustrate the properties of the mirrors at different voltage settings. The trajectory of each ion inside the mirror is indicated by a black line. In case of a situation where the trap is closed, i.e. $V_{M1} = 4600V$, depicted in Fig. 3.11 (a) the potential of the M1 electrode is high enough that ions remain stored inside the ion beam trap. The simulated trajectories show the ions turning around close to the M2 electrode. In Fig. 3.11 (b) the potential V_{M1} was lowered to 4000V. Under these settings the equipotential surfaces around the M1 and M2 electrode illustrate the occurrence of the hole inside the M1 electrode. The trajectory calculations performed with the same set of Ar^+ ions as in Fig. 3.11 (a) shows that the kinetic energy of the ions is now sufficient to overcome the potential barrier and they leave the ion trap.

Injection into the ion beam trap was also simulated and is displayed in Fig 3.12, showing a beam of Ar^+ ions at 4.2keV energy with a diameter of 2mm being injected through a hole inside the mirror. Simulated potential settings are the same as used for the simulation of extraction illustrated in Fig. 3.11 (b).

In previous work conducted using this type of ion trap [24, 114, 85, 84] a different scheme for injection and extraction of ions was applied. In their case an ion bunch was injected with the complete entrance mirror at ground potential. While the ion bunch resides inside the trap the

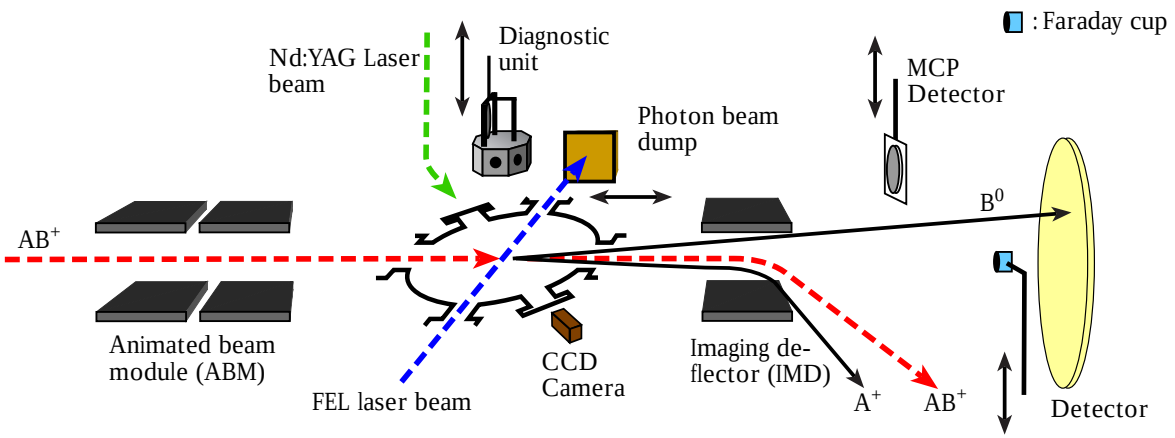

Figure 3.13: *Schematic drawing of the interaction region.*

entrance mirror was quickly raised and the trap is effectively closed around the ion bunch. For extraction the procedure was reversed and the exit mirror was quickly lowered while the entrance mirror remained at high potential. In our applications ions were mostly injected and extracted through a hole in the mirror although usage of the above mentioned method is also possible.

3.5 Interaction region

3.5.1 Layout of the interaction region

Fig. 3.13 shows a schematic drawing of the ion-photon overlap region and the imaging detector setup. The ion beam is focused into the overlap region where it passes through the animated beam module (ABM). The ABM unit is used to shift the ion beam in vertical direction. After leaving the ABM unit the beam is crossed either with the FEL beam or the laser beam coming from the Nd.YAG laser system. The neutral and charged fragments resulting from photodissociation events and the unreacted ions leave the overlap region towards the imaging detector. In the imaging deflector unit (IMD) all charged fragments are deflected and only the neutral fragments proceed to the imaging detector.

The ABM is made up of two sets of up-down deflection plates each with a length and width of 6cm. Opposing plates are placed 6cm apart. The distance between the two sets of plates is 2cm. The IMD consists of two opposing metal deflection plates with a length of 10cm and a width of 6cm situated 7cm apart.

In case of the ABM unit the electrical connections vary depending on the direction of steering. Assuming an ion beam of positively charged particles and the ABM should produce a parallel shift in the downward direction. On the first set of deflection plates the corresponding settings would be a positive polarity on the upper plate and a negative polarity on the lower plate. To

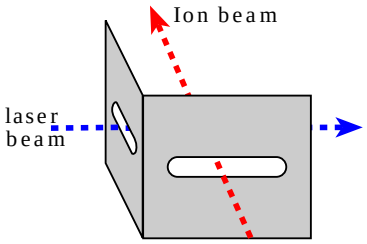

Figure 3.14: *Schematic drawing of the device used to force the overlap of ion and photon beam.*

compensate for the downward shift of the first electrode set and produce a net parallel shift the polarities on the second set of electrodes need to be the opposite of the first set. For ion deflection the upper plate of the IMD is connected to a positive power supply while the lower plate is grounded. A potential of 2500-4000V on the upper plate was found to be sufficient to steer all charged particles away from the detector.

3.5.2 Forced overlap method used in the optical laser experiments

For the optical laser experiments on Ar_2^+ conducted in Heidelberg no diagnostic unit was installed in the interaction region. The best overlap of ion and photon beam was determined by shifting the ion beam stepwise using the animated beam module and comparing the resulting photodissociation signals. However, after these experiments a forced overlap method was applied to control the overlap of the two beams. Therefore a linear motion feedthrough was installed in the interaction chamber above the crossing point of ion and photon beam. An assembly of two plates mounted in a 90° angel illustrated in Fig. 3.14 is attached to the feedthrough. Using the motion feedthrough the device can be moved into the overlap region of ion and photon beam. Each plate contains a 3mm slit allowing photon and ion beam to pass the device if both beams are situated at the same height.

3.5.3 Diagnostic of the overlap region at FLASH

Overview of the diagnostic unit

At the experimental setup installed at FLASH the overlap of the ion and photon beam can be monitored using a diagnostic unit as displayed in Fig. 3.15 (a)). This diagnostic unit is installed inside the interaction region chamber at the crossing point of ion and laser beam (see Fig. 3.13). The diagnostic device is attached to a linear motion feedthrough and can be moved into the overlap region.

Ion beam diagnostics

To determine the transverse profile of the ion beam the unit features a 25mm MCP equipped with a phosphor screen. Upon operation the front plate of the MCP is typically at -1300V

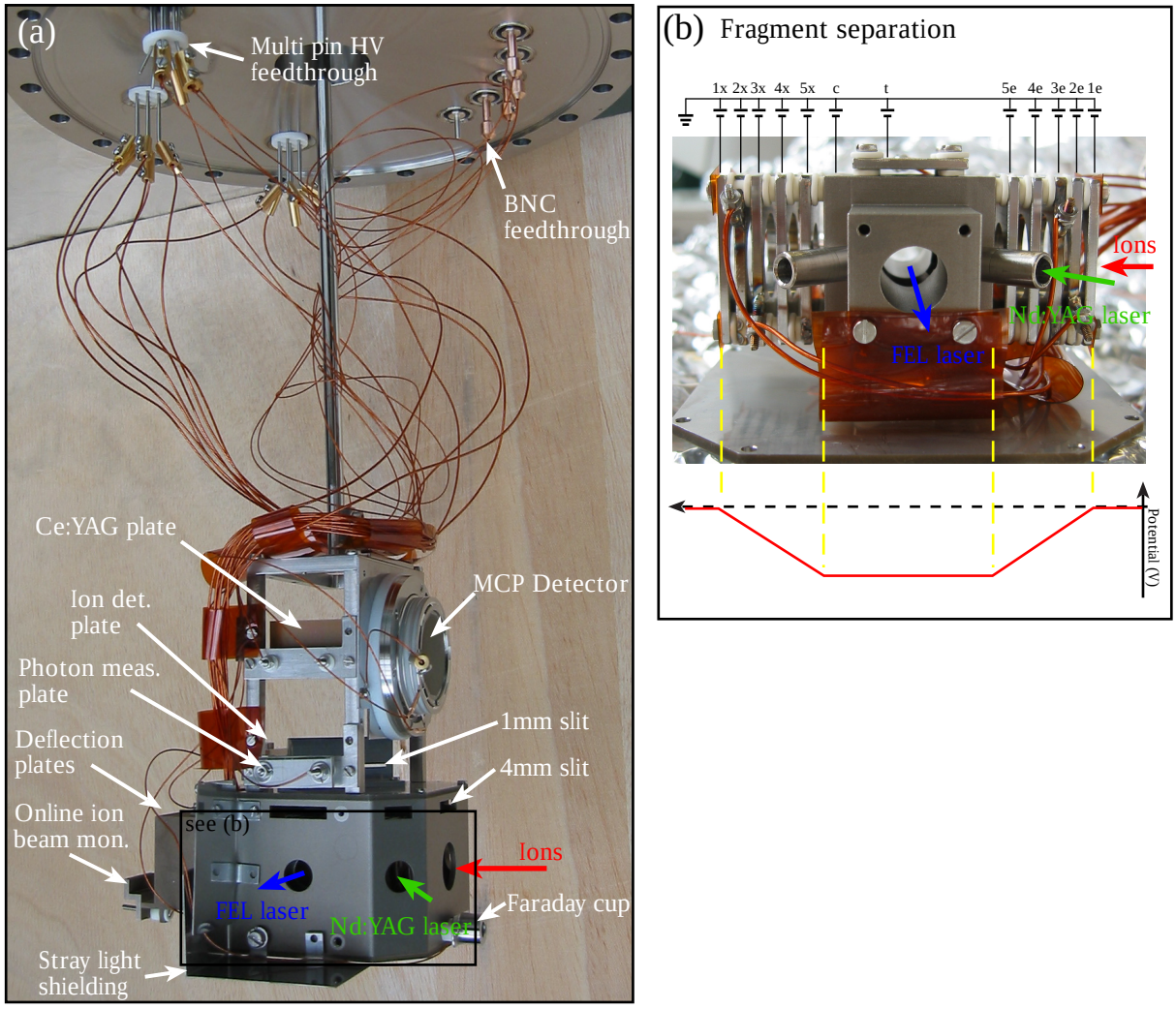

Figure 3.15: *Interaction region diagnostic unit. Fig. 3.15 (a) shows a picture of the complete unit and (b) illustrates the device used for fragment separation mounted on the inside of the diagnostic unit (position is indicated by a black rectangle in Fig. 3.15 (a)).*

to -2000V, the back plate remains grounded and the phosphor screen is at 2000V. To obtain pictures from the phosphor screen of the MCP detector a CCD camera is installed outside the vacuum chamber pointing at the center of the interaction region as illustrated in Fig. 3.13 (a). Below the MCP detector a plate used for ion detection is mounted electrically insulated behind the 1mm slit. Additionally a Farady cup is installed in the lower part of the diagnostic unit. The cup has an opening of 5mm diameter an is mounted electrically insulated inside a grounded housing. Ion current signals originating from the cup and the detection plate are connected in series and transferred to the outside of the vacuum chamber via a BNC feedthrough as shown in Fig. 3.15 (a). For ion current measurements both detection devices are biased to -100V using a battery.
As further means of ion beam diagnostic another Faraday cup is installed just before the imaging detector. The cup is mounted on a linear motion feedthrough and can be moved to different positions in the beam pipe. Additionally a second MCP detector with phosphor screen is installed just before the imaging detector. Similar to the MCP detector contained in the diagnostic unit the phosphor screen can be monitored by a CCD camera situated outside the vacuum chamber. To remove the MCP detector from the beam pipe it is attached to a linear motion feedthrough.

Photon beam diagnostics

Facing the photon beam coming from the free-electron laser a small copper plate coated with a Cerium doped YAG crystal (Ce:YAG) is installed. When excited by ultra-violet photons this crystal emits florescence light in the green [104]. The plate is mounted at about the same height as the phosphor screen from the MCP detector and can be monitored by the CCD camera.
At the same height as the ion detection plate an additional photon detection plate is mounted on the diagnostic unit at a 90° angel. The plate is electrically isolated from the rest of the structure. The photon beam coming from the FEL striking the plate surface produces an electrical signal which is fed to a BNC feedthrough and can be monitored outside the vacuum via a charge sensitive amplifier.
After crossing the ion beam the FEL beam can be collected on a photon beam dump installed about 1m downstream. Basically the photon beam dump is a small 3x3cm^2 copper plate mounted electrically isolated on a linear motion feedthrough. The beam dump can thus be removed from the beam pipe allowing the photon beam to pass on to experiments situated behind this setup. Similar to the photon measurement plate it is also possible to obtain a photon beam related signal from the photon beam dump.

Determination of the overlap of ion and photon beam

In order to determine the spatial overlap of the two beams a plate with a slit of 1mm width is mounted just below the MCP detector at a 45° angle which allows the ion beam and the

FEL beam to pass the slit at the same time. Ion and FEL beam are then collected on the ion detection plate or photon measurement plate respectively. A measurement of the spatial overlap of the two beams can be done by moving the 1mm slit across the interaction point and comparing the ion signal with the photon signal directly. Experimental results of such a scan can be seen in Fig. 4.9. Additionally, such an overlap scan can also be carried out using a 4mm slit which is situated just below the 1mm slit.
To determine the temporal overlap a fast timing signal can be extracted form the photon beam dump. In case of the MCP detector the signal of the electron charge cloud produced by impinging particles on the MCP front plate is measured at the back of the MCP detector yielding an arrival time signal of the ions. If one compares the two signals using an oscilloscope the temporal overlap can be determined. An example of such a measurement is displayed in Fig. 4.8.

Biased interaction region

The lower part of the diagnostic unit contains the device displayed in Fig. 3.15 (b). Somewhat similar in design to the ion beam trap (compare Ch. 3.4) the unit consists of five entrance and exit electrodes (labeled 1e–5e and 5x–1x respectively) and a central metal block (c). Additional electrodes are mounted on top (t) as well as on the bottom (b, not visible in Fig. 3.15 (b)) of the central part. The complete unit features openings at the appropriate places to allow the ion beam as well as the FEL and Nd:YAG laser beam to pass through as indicated by the arrows in Fig. 3.15 (b). The whole assembly is enclosed by the octagonal box attached to the interaction region diagnostic unit as can be seen in Fig. 3.15 (a).
Electrical connections are made by attaching capton insulated cables to threaded rods welded to each electrode. The cables are then fed to multi pin HV feedthroughs as shown in Fig. 3.15 (a). The voltage for each individual electrode is supplied by a separate negative 6kV power supply (iseg EHQ 8060 unit). The potential on the central electrode is distributed evenly across the entrance and exit electrodes producing a homogeneous field inside the central part with a field gradient towards electrode 1e and 1x respectively as indicated in the lower part of Fig. 3.15 (b). Ions entering the assembly as indicated by the arrow will be accelerated towards the center and obtain higher kinetic energy. In the region of homogeneous electric field the ion beam is overlapped with the photon beam. While the unreacted ions and charged fragments produced in reactions with photons are decelerated again upon leaving the assembly on the other side, neutral fragments will leave with a higher kinetic energy. Neutral fragments will thus arrive at the detector earlier resulting in a separation of photodissociation fragments in time.
For online monitoring of the ion bunch intensity another detection plate is mounted after the biased interaction region. The ion bunches leaving the interaction region are thereby deflected onto the detection plate indicated in Fig. 3.15 a) by a set of vertical deflection plates also installed after the biased interaction region. The ion bunch signal emanating from the electrically isolated plate is fed to the outside of the vacuum chamber and enhanced using a charge sensitive amplifier.

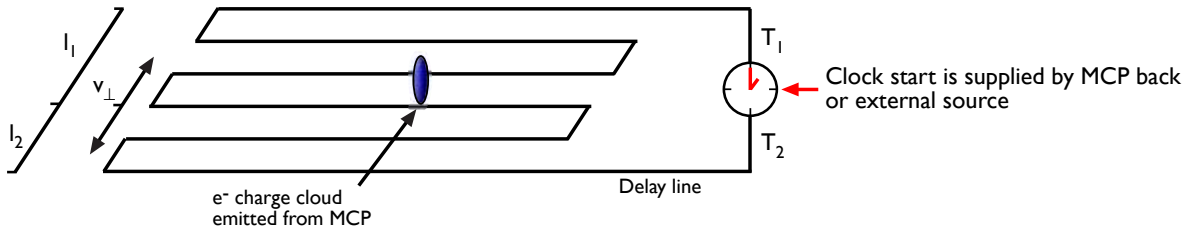

Figure 3.16: *Schematic principle of operation of a delay-line readout for one dimension. A meander-shaped delay-line picks up the charge cloud (here emitted form the MCP stack), the induced signals travel along the wire with an effective speed of* $v_\perp$ *towards the ends. The signal arrival time difference is proportional to the pickup position in direction of* $v_\perp$*.*

Individual ion bunch intensities can thus be constantly recorded during the ongoing experiment.

3.6 Photofragment detection

3.6.1 The principle of delay line detection

The principle behind the delay-line technique is to take advantage of the delay that a signal experiences when traveling on a transmission line which is preferably meander-shaped or helical to introduce an effective propagation speed $v_\perp$ (see Fig. 3.16). For each dimension, the respective position is directly proportional to the time difference $T_1 - T_2$, where T_1 and T_2 are the arrival times of the signal at the two ends of the delay-line measured with respect to a time zero. In case of a 2D delay-line with crossed wires and if we declare the actual event as the zero point in time one obtains the following:

$$T_{x1}(i) = t_{tof}(i) + P_{x1}(i) - D_s \quad (3.4)$$

$$T_{x2}(i) = t_{tof}(i) + P_{x2}(i) - D_s \quad (3.5)$$

$$T_{y3}(i) = t_{tof}(i) + P_{y3}(i) - D_s \quad (3.6)$$

$$T_{y4}(i) = t_{tof}(i) + P_{y4}(i) - D_s, \quad (3.7)$$

where i denotes the particle number, T the time recorded for each wire end, P contains the propagation time on the x- or y-wire until the hit is recorded, D_s is the delay of the clock start and t_{tof} contains the time it takes the fragments to fly from the event location to the detector. Any coordinate for a given particle i can be calculated in the following way:

$$\begin{aligned} \mathrm{X}(i) &= l_1 - (\frac{l_1 - l_2}{2}) && (3.8)\\ &= \frac{\mathrm{v}_x}{2}(\mathrm{P}_{x1}(i) - \mathrm{P}_{x2}(i)) && (3.9)\\ &= \alpha_x(\mathrm{T}_{x1}(i) - \mathrm{T}_{x2}(i)) && (3.10) \end{aligned}$$

and respectively

$$\mathrm{Y}(i) = \alpha_y(\mathrm{T}_{y3}(i) - \mathrm{T}_{y4}(i)) \quad (3.11)$$

with α_x and α_y being the characteristic detector calibration factors, which can be determined by calibrating the detector with a mesh with known grid size (see Sec. 4.5).
Additionally Eq. 3.4 - 3.7 allow two independent determinations of the arrival time t_{tof} of each particle, namely

$$\mathrm{t}_{012}(i) = \mathrm{t}_{tof}(i) - \mathrm{D}_s = \frac{1}{2}(\mathrm{T}_{x1}(i) + \mathrm{T}_{x2}(i) - \mathrm{S}_{12}(\Delta\mathrm{T}_{12}(i)) \quad (3.12)$$

$$\mathrm{t}_{034}(i) = \mathrm{t}_{tof}(i) - \mathrm{D}_s = \frac{1}{2}(\mathrm{T}_{y3}(i) + \mathrm{T}_{y4}(i) - \mathrm{S}_{34}(\Delta\mathrm{T}_{34}(i)) \quad (3.13)$$

where $\mathrm{S}_{12}(\Delta\mathrm{T}_{12}) = \mathrm{P}_{x1}(i) + \mathrm{P}_{x2}(i)$ is the timesum for channel 1 and 2 and $\mathrm{S}_{34}(\Delta\mathrm{T}_{34}) = \mathrm{P}_{y3}(i) + \mathrm{P}_{y4}(i)$ is the timesum for channel 3 and 4 respectively. The availability of two independent determinations of t_{tof} makes it possible to check the validity of an event and in case of a multi-hit event allows an assignment of corresponding hits. A valid event has then to fulfill the following condition

$$\mathrm{t}_{012}(i) - \mathrm{t}_{034}(i) = 0. \quad (3.14)$$

3.6.2 The delay line detector

For photofragment detection a RoentDek DLD80 MCP [44, 99] delay-line detector system was used in all experiments. The detector system comprises a pair of 80mm MCP plates in a chevron configuration mounted in front of a 2D-position sensitive delay-line anode (see Fig. 3.17). The anode comprises two double delay-line helical propagation lines (Lecher-line). For each dimension a wire pair is formed by a collection (signal) wire and a reference wire.
For neutral as well as positively charged photofragments the front of the MCP stack was operated with a potential of -2400V to -3000V while the MCP back was kept on ground. A potential difference of about +20V to +50V of the signal wire with respect to the reference wire ensures that the electron cloud emerging form the MCP stack is mainly collected on the signal line, shared almost equally between both dimensions. The anode holder has to be supplied with an

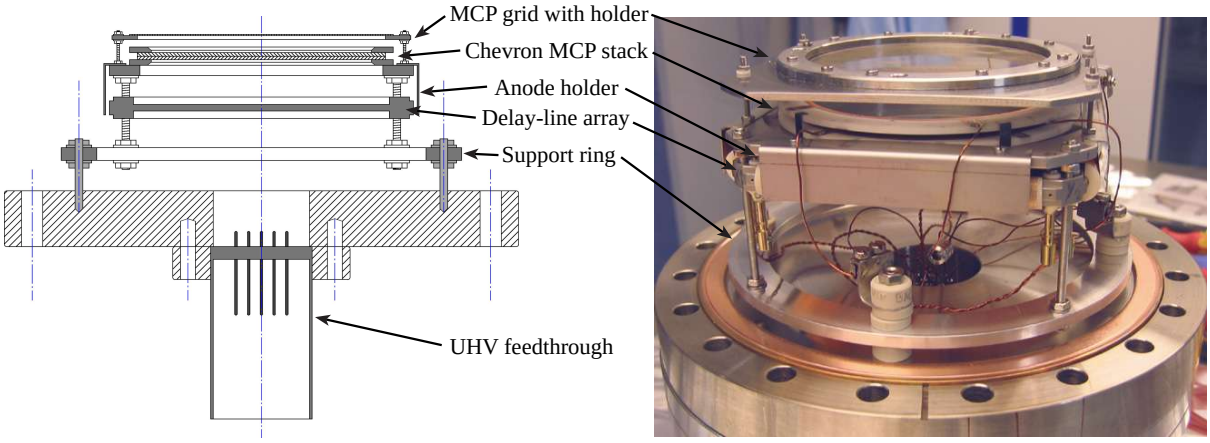

Figure 3.17: *Schematic drawing (not to scale) and a picture of the RoentDek DLD80 delay-line detector used for photofragment detection in our experiments.*

intermediate potential with respect to the anode wires and the MCP back potential to ensure proper charge cloud propagation. The optimal voltage settings for both holder and wires depends on the relative distance between the MCP, holder plates and the anode wires. These settings were determined experimentally and can be found in Tab. 3.2. To shield the detector a grounded grid was added in front of the detector at a later stage.

MCP grid	0V
MCP front	-2400V to -3000V
MCP back	0V
Anode holder	+300V
Reference wires	+680V
Signal wires	+700V

Table 3.2: *Detector voltage settings.*

For readout of the detector signals the RoentDek DLATR6 module was used. It contains a 6 channel differential amplifier with integrated constant fraction discriminator (CFD) circuits for each channel. The onboard CFD stages provide precise ECL timing signals with an accuracy of less than 50ps and can separate a consecutive pair of incoming signals with a pulse-pair resolution of 20ns. The timing signals are then passed on to a time-to-digital-converter (TDC) module which digitizes the timing information and is read out by a PC after each detector exposure. For more details concerning the DAQ system see Ch. 4.1.1.

3.7 Light sources

3.7.1 The Nd:YAG laser system

Optical laser setup in Heidelberg

The laser used in the optical laser experiments is a Continuum Powerlite 6050 Q-switched Nd:YAG laser system. The laser system features an internal doubling crystal. Thus output of 1064nm light and 532nm light is possible. Typical operating parameters can be taken from Tab. 3.3.
The setup of the laser including optics as shown in Fig. 3.18. The laser beam leaving the Nd:YAG laser is coupled down from the original beam size of 7-8mm to approximately 2-3mm in diameter via a telescope. In a two prism arrangement the beam is transferred to the correct height thereby changing the polarization of the 532nm beam from originally vertical orientation to horizontal. Afterwards the beam is sent through the doubling crystal. The resulting 266nm light is separated from the 532nm by a dichroic mirror installed at a 45° angel after the crystal.

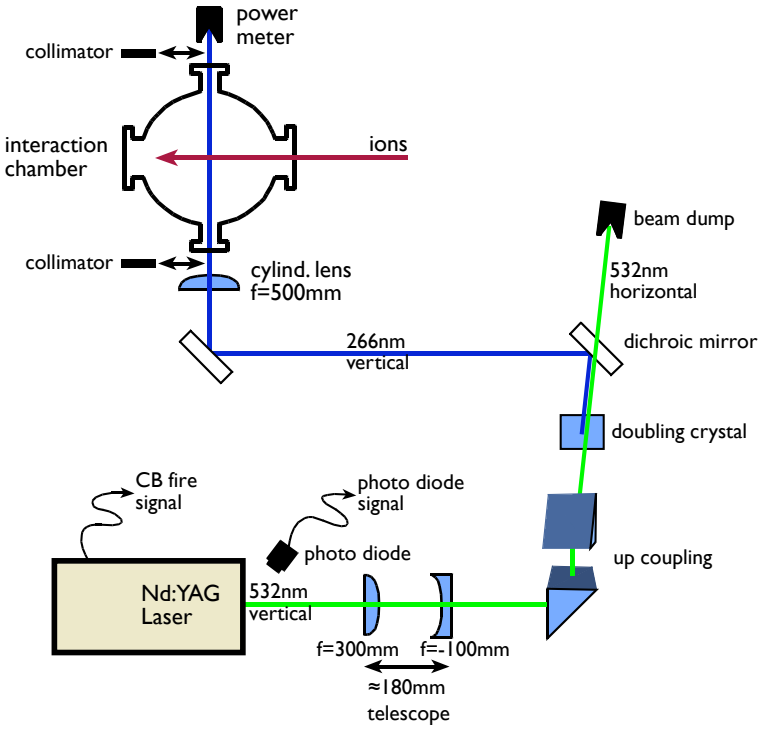

Figure 3.18: *Experimental setup for the optical laser experiments.*

Laser output	1064nm, 532nm, 266nm (with 2nd doubling see Fig. 3.18)
Energy per pulse	30mJ, 3mJ, 1mJ
Pulsewidth	6–9ns
Linewidth (FWHM)	30GHz
Repetition rate	40–50Hz

Table 3.3: *Technical specifications for the Continuum Powerlite 6050 laser system taken from [20].*

The 532nm light is collected in a beam dump situated after the dichroic mirror. The 266nm light is reflected onto another mirror and then sent through a cylindrical lens which focuses the beam in the center of the interaction chamber. The laser beam enters and exits the vacuum chamber through quartz viewports. After being overlapped with the ion beam the laser beam is collected in a power meter situated outside the vacuum chamber. For 532nm operation the doubling crystal is removed and the dichroic mirror is replaced. Alignment of the laser beam to the center of the vacuum chamber can be controlled by two removable collimators installed on both sides of the interaction chamber.
For the experimental timing the flash lamp fire pulse, called CB fire, is extracted from the laser. The CB fire pulse is emitted about 155μs before a light pulse is delivered. A second timing signal is obtained from a fast photo diode (EO Tech ET-2030) with a risetime of less than 300ps which monitors the actual laser output.

Optical laser installation at the FEL

At the FEL the optical laser described in the previous section is mounted on top of the beam line as can be seen in Fig. 3.3. Here the laser beam emitted from the laser is reflected by 90° so it is parallel to the beam line. Afterwards it is coupled down onto an optical table mounted on the side of the beam pipe using two mirrors. On the optical table the beam is reflected into the interaction chamber. Before entering the vacuum chamber at a 45° angle with respect to the ion beam as indicated in Fib. 3.13 it passes through a telescope reducing the overall beam diameter to 3mm. The laser beam is brought to overlap with the ion beam and leaves the interaction chamber on the other side where it is collected by a power meter.

3.7.2 The VUV free-electron laser at DESY in Hamburg (FLASH)

Principle of operation of a SASE FEL

In a conventional laser the amplification derives from the stimulated emission of electrons bound to atoms, either in a crystal, liquid dye or gas, whereas the amplification medium of a free-

electron laser (FEL) are "free" (unbound) electrons. Since the electrons in the FEL are not bound to atoms and thus not limited to specific transitions, the wavelength of the FEL is tunable over a wide range depending on accelerator energy.
The basic principle of the free-electron laser based on the self amplified spontaneous emission (SASE) process [14, 52, 97] can be described as follows and is illustrated in Fig. 3.19. The free electrons are stripped from atoms in an electron gun and are accelerated to relativistic velocities. These relativistic electrons are send through a long, periodic magnetic dipole array, a so called undulator. Due to the Lorentz force introduced by the magnetic field of the undulator the electrons are accelerated in the direction transverse to their propagation and are forced on a sinusoidal path. Hence, they emit synchrotron radiation in a narrow cone in the forward direction at the resonance wavelength λ_{ph}. This spontaneous emission acts back onto the electron bunch inside the undulator. Electrons that are in phase with the electromagnetic wave are retarded while the ones with opposite phase gain energy causing a longitudinal fine structure of the electron bunch, the so called micro-bunching. With micro-bunching fully established, all electrons radiate in phase which yields a radiation power output proportional to N_e^2, where N_e is the number of electrons in the bunch. This gives an amplification of many orders of magnitude with respect to the radiation power emitted by spontaneous emission, which is proportional to N_e.

Layout of the FLASH facility

The free-electon laser in Hamburg [7, 1, 4] results from an extension of the TTF FEL, Phase 1 [93, 2, 18] which successfully demonstrated SASE at 109nm in 2000 [6]. The main goals of FLASH are to extent the accessible radiation wavelength down to 6nm and to make the facility more accessible for users. An overview of the facility including the experimental hall is depicted in Fig. 3.19.
The electron beam is produced in a radio frequency (RF) photocathode gun and accelerated up to 1GeV beam energy by six superconducting TESLA modules [78]. At energy levels of 130MeV and 450MeV the electron bunches a compressed from a length of 2mm RMS at the exit of the gun to approximately 50μm RMS in order to provide the peak current of 2.5kA required for the FEL. Before the electron bunch enters the undulator section particles with too large energy deviations are removed in the collimator section. In the undulator section the electron bunch is forced onto a sinusoidal path producing the FEL radiation. When leaving the undulator a dipole magnet deflects the electron beam into a beam dump, while the FEL light propagates to the experimental hall.
The experimental hall features five different beamlines for user experiments. Two of these beamlines (PG1 and PG2) are served by a high resolution monochromator while the other three (BL1, BL2 and BL3) use the direct FEL beam. The TIFF experiment is currently installed 1.5m before the focus of the PG2 [62] beamline as indicated in Fig. 3.19. The monochromator

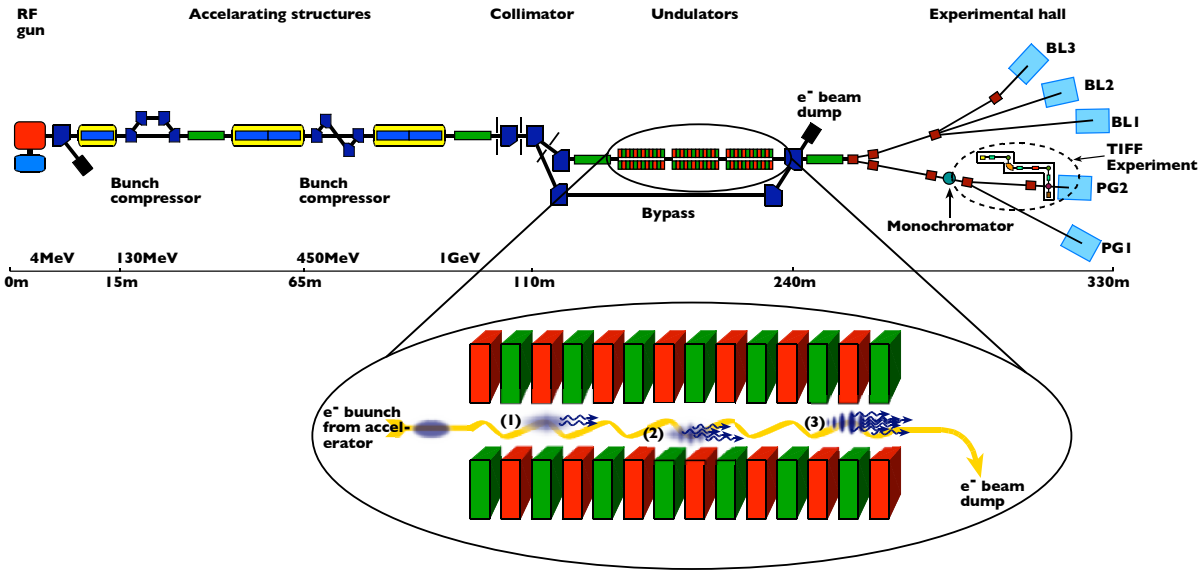

Figure 3.19: *Layout of the FLASH facility at DESY based on [1]. Insert: SASE principle; (1) the electron bunch traveling at relativistic velocities in the undulator is forced on to a sinusoidal orbit by the magnetic field; (2) in resonance the back action of the emitted spontaneous radiation on the electron bunch leads to a modulation of the electron density on the scale of the undulator radiation wavelength (micro bunching); (3) with complete micro bunching all electrons radiate in phase leading to an overall radiation power growth proportional to* N_e^2.

serving this beamline is a plane grating monochromator developed at BESSY [31]. The tuning range of the monochromator includes the full FEL spectral range and higher harmonics up to 1keV photon energy. The exit arm of the monochromator is rising at an angel of 4° such that the focal point of the PG1 and PG2 beamlines is approximately 2.5m above ground.

4. Commissioning of the setup

4.1 Control of the experiment

4.1.1 Data acquisition system and timing of the experiment

In the experiments conducted in Heidelberg the HM1 TDC module supplied by RoentDek was used. This TDC unit features 4 TDC channels with one common start input, an adjustable resolution ranging from 133ps to 808ps, a range of 2.1 - 13.2μs (depending on resolution) and the possibility to record up to 3 hits per channel. For more precise specifications see [92, 91]. Using a PCI based interface card the data was transferred to the PC.
At a later point the data acquisition was changed to a CAMAC based system. The layout of the data acquisition system as well as the other systems used to control the experiment is displayed in Fig. 4.1. The data acquisition (DAQ) system consists of a CAMAC crate with a 32 channel time-to-digital converter (TDC, LeCroy Model 2277) used to readout the detector. This particular TDC features a resolution of 1ns, a range of up to 65μs and it can record up to 16 hits per channel. For processing of analog signals there is a 8 channel analog-to-digital converter (ADC, Ortec AD 811) installed in the CAMAC crate which returns the peak height of an input signal after receiving an externally supplied trigger signal. As an alternative the DAQ PC is equipped with a 2 channel PCI scope card (Gagescope Model CS 14100). This card allows recording of arbitrary wavefroms. An example of a recorded scope trace can be found in Fig. 4.8.
The timing of the experiment is based on two PCI based timer counter cards (PCI-6602) supplied by National Instruments. Each card offers 8 channels with a precision of 12.5ns giving 5V TTL signals as output. Each channel can be triggered by an external source or can be free running. The detailed timing configurations are subject to constant changes depending on the experimental conditions and will thus be discussed at a later stage (see Ch. 5.2 and Ch. 6.2).

4.1.2 Power supplies

Compact FieldPoint system

To address power supplies that feature control and monitoring based on analog voltages (usually 0-10V) it was decided to use the Compact FieldPoint (cFP) system supplied by National

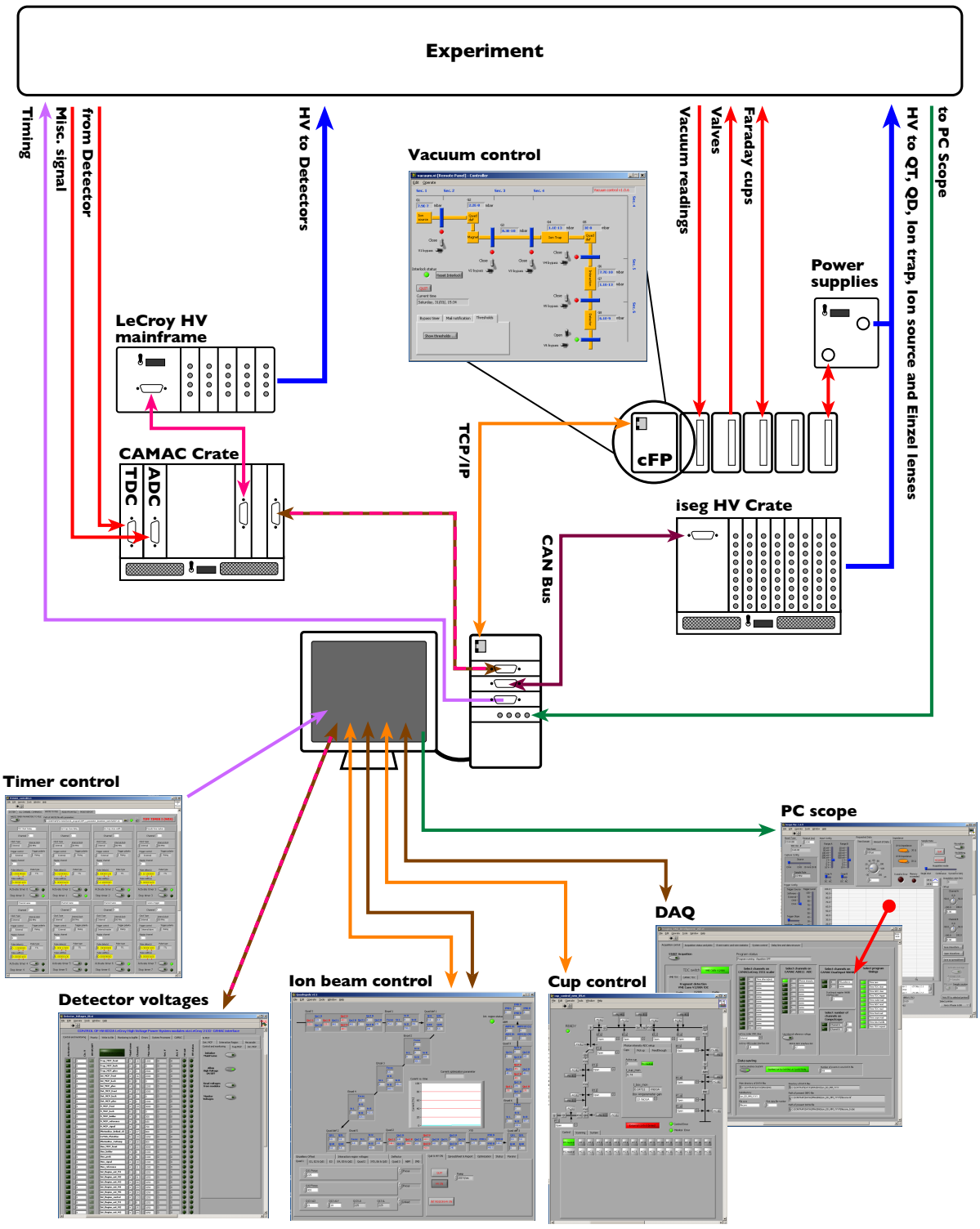

Figure 4.1: *Schematic of the programmatic control of the experiment.*

Instruments. This system features controller units that are able to address different input or output (I/O) units. The I/O cards come in 8 channel or 16 channel variants and can supply or read either analog or digital signals. The controller units as well as the I/O cards are mounted on a back plane which can accept up to 8 different I/O modules. Communication with the cFP host controllers is done via the TCP/IP protocol so standard network cabling can be used and no additional interface cards are necessary on the PC side. Power supplies controlled by the cFP system are ion trap power supplies, Einzel lenses, quadrupole triplets, magnet power supply and the ion source.
Furthermore the motorized motion feedthroughs carrying the ion beam diagnostic units (see Ch. 3.2.2) and the interaction region feedthrough (see Ch. 3.5) are also remote controlled using the cFP system.

CAN bus based power supplies

The power supplies needed for the quadrupole triplets and steerer units are controlled through a different system. Due to the high density of medium voltage channels with low power requirements, needed for that application a multi channel system made by iseg Spezialelektronik GmbH (EHQ multi channel HV system) was chosen. In our case this system features 8 interchangeable HV modules installed in one 19" crate which can be addressed via a CAN interface. Each HV module is available with either positive or negative polarity and offers 8 channels ranging form 0-2000V (EHQ 8020) or from 0-6000V (EHQ 8060). Thus a total of 64 channels are available which is sufficient to supply the high voltage necessary for the quadrupole triplets, the steerer units and for the electrodes installed in the interaction region used for fragment separation (see Ch. 3.5).

LeCroy high voltage mainframe

Voltages for the detectors are supplied by a LeCroy multi channel high voltage mainframe (LeCroy Model 1440) addressed via an interface module plugged into the CAMAC crate as shown in Fig. 4.1. This system can deliver stable voltages of 1.6kV or 3.2kV of both polarities. This system supplies the voltages to the imaging detector, the 0°-MCP detector as well as the diagnostic MCPs installed in the interaction region and in front of the imaging detector.

4.1.3 Programatic control of the setup

The programatic control of all the systems discussed in the previous section is achieved by specifically written applications developed with the LabView programming environment provided by National Instruments. These applications run on a Windows 2000 based computer system and communicate with the above mentioned systems through several interface cards as indicated in Fig. 4.1.

The programmatic control of the different power supplies mentioned in Ch. 4.1.2 is split up among three different LabView based applications. One program is used to control the ion source related functions, like magnet and other associated power supplies, the valve controlling the gas inlet and the recording of mass spectra as shown in Fig. 4.2 and Fig. 4.3. Another separate program is in charge of controlling the power supplies necessary to operate the ion beam trap and a separate program is used for communication with the LeCroy high voltage system supplying the detector voltages. The remaining HV channels are all used to control the properties of the ion beam and are therefore merged into the ion beam control program. This program combines control over all focussing and steering units, the quadrupole deflectors, the ABM module, the IMD unit and the fragment separation unit installed in the interaction region (see also Ch. 3.2.2 and Ch. 3.5). Furthermore by using an algorithm very similar to the Powell optimization method [86] the program offers a way to programatically optimize the ion beam current at a given point along the beam line. This method works by monitoring the ion beam current measured by a Faraday cup and varying a user given set of parameters in small steps up and down. Two different approaches can be taken. Either each parameter is varied individually and the move in the direction yielding the highest increase in beam current is made before moving to the next parameter. In the second approach, the parameter is continuously varied in one direction until a maximum in the ion beam current is reached before moving on to the next parameter.
The motorized motion feedthroughs are controlled using the cup control program. Each feedthrough is assigned a unique identifier encoded using 14 bits. A motion feedthrough can be selected giving its individual address using a cFP digital output module. The feedthrough position is set and monitored via 0-10V analog signals also using cFP I/O modules. The timing of the experiment using the timer cards (see Ch. 4.1.1) is influenced through the timer control program. The program allows to set the settings for each timer channel separately or channels can be grouped together defining one master channel on which other channels are dependent on. In the LabView program controlling the scope card individual time markers can be defined on a per channel basis. The recorded peak heights at these marker positions are then passed on to the DAQ program running on the same computer. The DAQ application reads out the data from the CAMAC crate via a Wiener CC32 interface card and obtains the data from the scope through shared variables stored in the computer memory. The data is then written to disk in small ASCII files typically containing 500 to a few thousand events.

4.1.4 The vacuum interlock system

Each FieldPoint controller can be used as an embedded stand alone system featuring a real-time capable operating system. This possibility was utilized for the vacuum control system. The readings from the eight vacuum gauges are read in via a 0-10V analog input card, status readings are processed via a digital input card and the valves are controlled with a 230V output

module all mounted on the FieldPoint bank. All the channels are integrated and processed with a real-time application deployed on the FieldPoint controller. Due to the real-time nature of the underlying operating system a well defined response time to a defined fail state, for instance if a given vacuum threshold is crossed, of only several milliseconds is guaranteed.
The user communication with the vacuum monitoring program can be done through a web interface thus making the service accessible from almost any computer. Through the web interface the user can control the valves along the beam line and set individual threshold levels for each vacuum reading. In case of a failure users can be notified by email. Through the monitoring capabilities included in LabView the vacuum levels are constantly logged to another computer.

4.2 Characterization of the ion source

In Ch. 3.3 the ion source and it's individual components were described. This section will focus on the results obtained from measurements with the ion source. These measurements involved testing the source under different conditions with the main focus lying on good conditions for production of molecular ions. Two examples of these measurements can be found in Fig. 4.2 and Fig. 4.3. Fig. 4.2 and Fig. 4.3 show two different mass spectra obtained from the hollow cathode ion source with different gas mixtures. In both cases the ion source voltage settings were comparable to the ones shown in Tab. 3.1. The spectra were obtained by recording the current in the Faraday cup situated directly after the 90° bending magnet (see Fig. 3.2 and Fig. 3.3) while the magnet current is slowly ramped up.
Fig. 4.2 shows a mass spectra taken from the hollow cathode ion source with a gas mixture of Hydrogen, Neon and Helium. The ratio of Neon to Helium was about 2 to 3 with some trace amounts of Hydrogen. The source inside pressure was about 0.2mbar and the pressure outside the ion source was $2.5 \cdot 10^{-6}$mbar.
The second example depicted in Fig. 4.3 shows a mass spectra taken with a pure Argon gas mixture and is on display in Fig. 4.3. Source inside pressure was ≈0.6mbar and outside pressure was $1.3 \cdot 10^{-5}$mbar.
The mass spectra demonstrate that this type of ion source is well suited for production of a wide variety of molecular ions. With respect to the photodissociation experiments described in Ch. 5 and Ch. 6 sufficient ion currents of 10-40nA in the case of HeH^+ and around 100-150nA of Ne_2^+ for photodissociation experiments could be obtained (compare with Fig. 4.2). In the case of Ar_2^+ the ion yield was lower than the other species but was also still sufficient to perform photodissociation experiments (compare with Fig. 4.3). Also high currents of atomic ions could be obtained from the ion source. This was of importance for studies of the ion beam trap which will be elaborated in the next section where a typical ion yield of 150-200nA of Ar^+ was used to study trapping under different conditions. Because of the low ion yield of Ar_2^+ the high current of Ar^+ were also quite helpful for the Ar_2^+ photodissociation measurements. Since the experimental

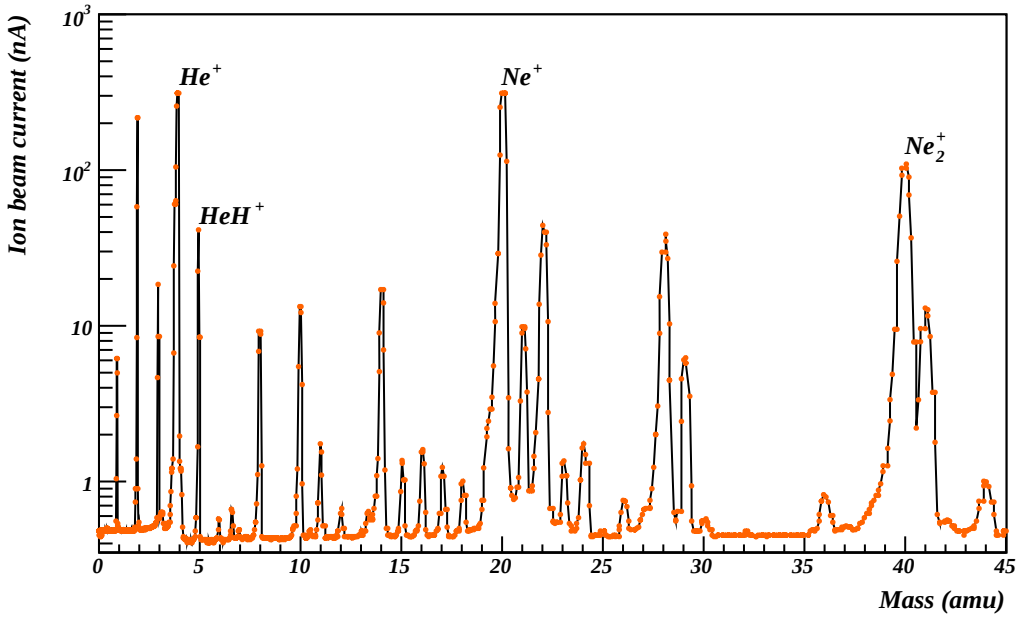

Figure 4.2: *Mass scan taken from the hollow cathode ion source with a Hydrogen, Neon and Helium gas mixture. With a ratio of Neon to Helium of 2 to 3 and trace amounts of Hydrogen. Source inside pressure was ≈0.2mbar and outside pressure was* $2.5 \cdot 10^{-6}$*mbar.*

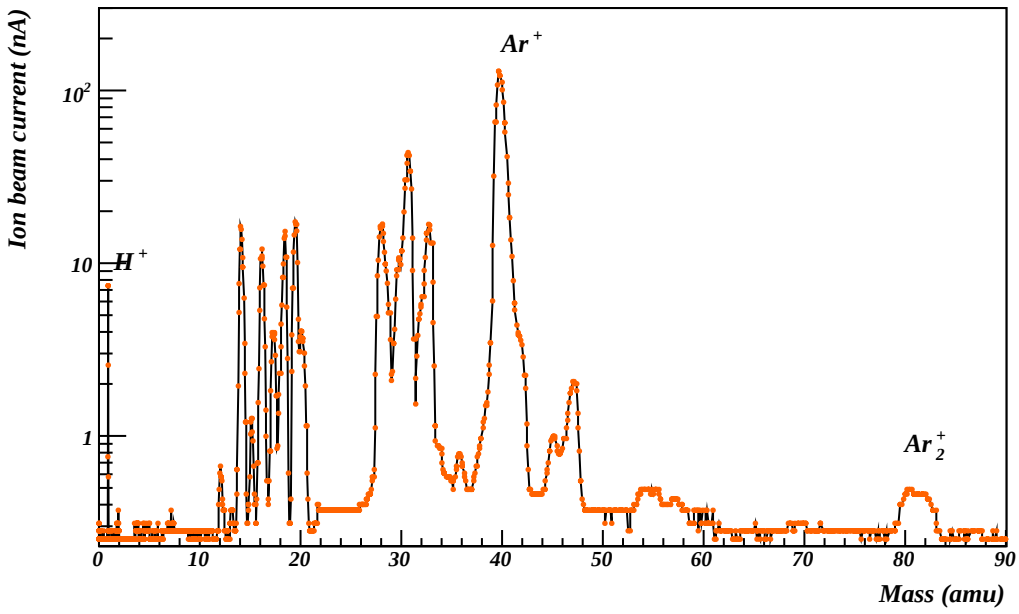

Figure 4.3: *Mass scan taken from the hollow cathode ion source with a pure Argon gas mixture. Source inside pressure was ≈0.6mbar and outside pressure was* $1.3 \cdot 10^{-5}$*mbar.*

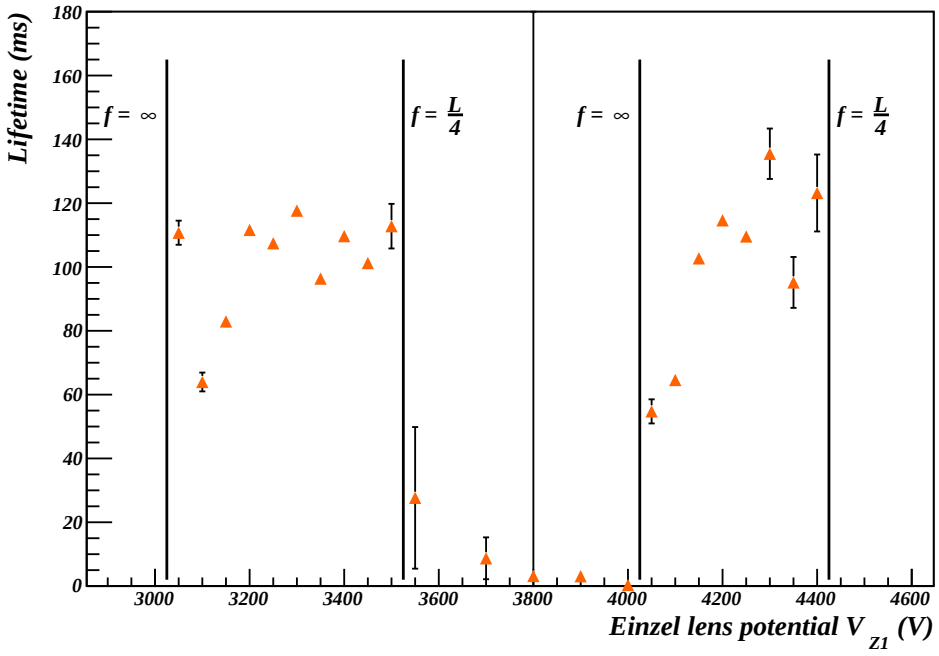

Figure 4.4: *(a) Fitted lifetimes for the long time behavior* t $>$ 30*ms of the measured decay curves as a function of* V_{Z1}*; (b) measured relative efficiency* ϵ_r *versus the Einzel lens potential* V_{Z1}*. Trap settings:* $V_{M5} = 1625V$*,* $V_{M4} = 3250V$*,* $V_{M3} = 4875V$*,* $V_{M2} = 6500V$ *and* $V_{M1} = 5700V$*, all electrodes not mentioned were grounded. The trap inside pressure was* $8 \cdot 10^{-9}$*mbar.*

setup is mostly based on electrostatic focussing and deflection optimal settings for an ion beam should be mostly independent of the mass of the ion. Making use of this fact the settings could be optimized with a strong Ar^+ beam. Then changing the magnet current to the Ar_2^+ beam required only subtle changes to the focussing and steering settings.

4.3 Characterization of the ion beam trap

4.3.1 Stability of the ion beam trap

Fig. 4.4 shows the experimental results obtained from trapping studies. In Fig. 4.4 a bunch of Ar^+ ions was injected into the trap for different values of V_{Z1} and it's evolution in the trap was followed for more than 1s by observing the count rate of neutral particles on the 0°-MCP. Two exemplary decay curves are displayed in Fig. 4.5. From these decay curves the lifetime of the trapped ions was derived. Fig. 4.4 shows the results for the lifetime of the decay curves. For each value of V_{Z1} data was accumulated over 100 injections and the long time behavior of the decay curves 30ms $\leq$ t $\leq$ 800ms (compare also to Fig. 4.5) was fitted with an exponential decay

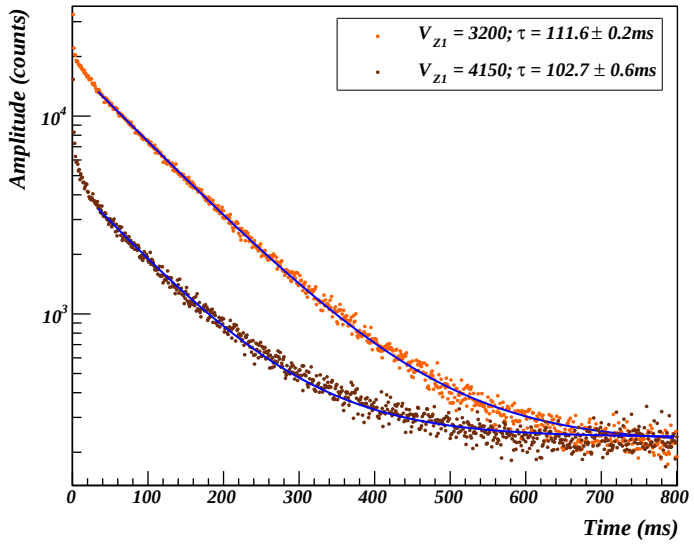

Figure 4.5: *Two exemplary lifetime curves for Ar^+ ions stored inside the ion trap for different settings of the Einzel lens electrode.*

taking into account a background. Time values $t \leq 30$ms were ignored due to saturation of the MCP detector resulting from the large number of particles hitting the detector upon injection. The obtained lifetimes are plotted versus V_{Z1}. As was expected, judging by the results obtained from the simulations (compare to Fig. 3.10), they are clearly two distinct regions where ions are trapped between the two mirrors. To compare to the simulation results the Einzel lens potentials corresponding to the boundary conditions given in Eq. 3.3 are marked by vertical lines. In general the agreement between the experimental data and the theoretical values is quite good even though the optical model cannot take into account the fact that ions penetrate into the mirror and are not reflected by a solid surface. The model furthermore has its limitations because it can also not cope with the large differences in focal length observed in the simulations for ions with increasing distance from the z-axis or with different angles of incident. For this reason the simulations carried out to determine the focal properties only took into account ions with small ($y \leq 1.5mm$) offset from the z-axis.
For a more detailed description of the ion beam trap and the interesting dynamics taking place in such an electrostatic ion trap can be found in [84, 85].

4.3.2 Trapping and extraction from the ion beam trap

To study trapping and extraction Ar^+ ions with a kinetic energy of 4.2keV were produced in the ion source and the ion beam was pulsed using the ion beam chopper (compare Fig. 3.2). Short bunches of Ar^+ ions with a typical length of several μs were then injected into the ion beam trap by lowering the entrance mirror to ground. Once the bunch is stored, its evolution can be monitored using the 0°-MCP located approximately 60cm after the trap (see Fig. 3.2), which measures the number of neutral Argon atoms emerging through the exit mirror. These atoms are produced in charge-exchange collisions with the residual gas inside the trap. In case of stable trapping conditions, the rate of neutral Argon atoms exiting the trap and hitting the MCP detector is proportional to the number of ions trapped between the mirrors, so that the beam decay can be studied this way.
The red curve in Fig. 4.6 shows an example for the measured number of neutral Argon hitting the 0°-MCP. Approximately 10^6 Ar^+ ions in a bunch of $3\mu s$ length were injected into the trap for each injection and the data shown here is a sum over 500 injections. Similar decay curves can be measured for different values of V_{Z1}. For all of these curves an increase in count rate could be observed at short times t < 20ms. After the first 20ms, the decay curves were characterized by a slow decaying part. In Fig. 4.6 an exponential fit taking into account a background level yields a lifetime for t < 20ms of $\tau = 262.1 \pm 9.4$ms.
In a detailed study of the characteristics of the ion beam trap Pedersen et al. [85] found that this multiexponential behavior of the decay curves could be attributed to different competing processes. Involving collisions with a residual gas species R, they considered two possibilities, namely electron capture (I) and elastic or inelastic scattering (II), and collisions among the

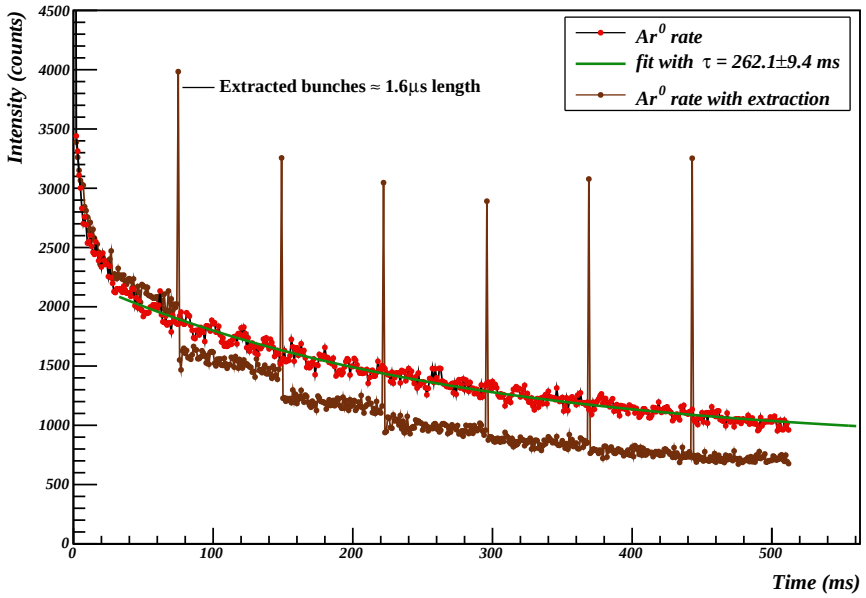

Figure 4.6: *The rate of neutral Argon atoms exiting the trap as measured by the 0°-MCP detector. The red curve shows an example for trapping without extracting the ions from the trap. The spectrum was summed over 500 injection cycles. The green curve indicates an exponential fit yielding a lifetime of* $\tau = 262.1 \pm 9.4$*ms. The brown curve illustrates trapping combined with multiple short extractions of ions also summed over 500 injection cycles. In this case the extraction electrode M1 was lowered form* $V_{M1} = 4600V$ *to 4440V several times for* $t_{extr.} = 1.6\mu s$*. The short bunch of extracted ions hits the 0°-MCP resulting in a steep increase in count rate. Due to saturation of the MCP detector the number of extracted ions appears to be higher for extraction numbers 5 and 6. Here the trap settings were* $V_{Z1} = 3900V$*,* $V_{M5} = 1000V$*,* $V_{M4} = 2000V$*,* $V_{M3} = 3000V$*,* $V_{M2} = 4000V$ *and* $V_{M1} = 4600V$*, all other electrodes were grounded. The trap inside pressure was* $3 \cdot 10^{-9}$*mbar.*

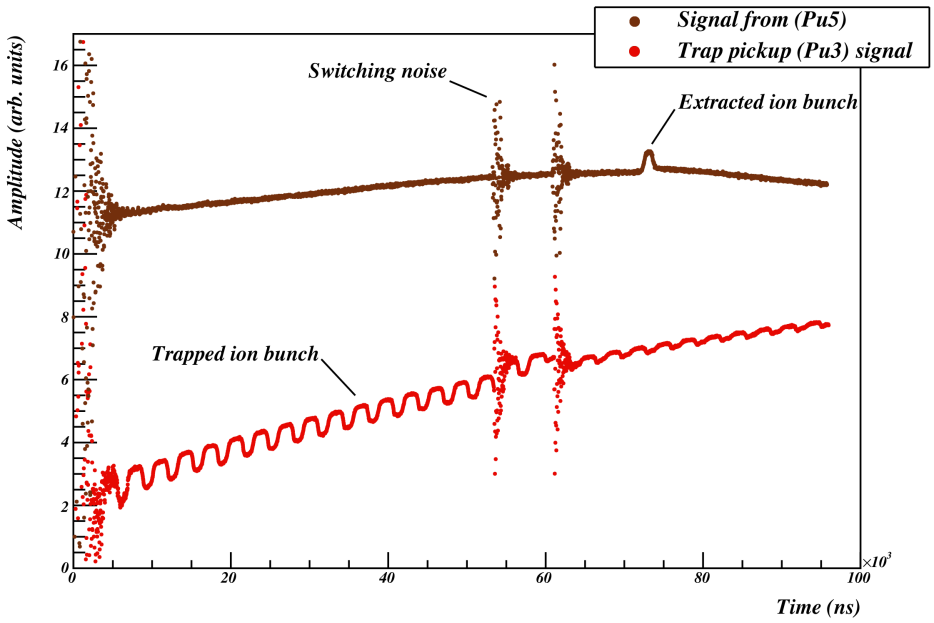

Figure 4.7: *Trapping and extraction as measured with the pickup electrodes (see Ch. 3.2.4). The brown curve shows the bunch oscillating inside the ion trap as recorded by the trap pickup (Pu3). After switching the trap electrode, which manifests itself in the spectrum by the indicated spikes, a bunch is registered by the pickup situated shortly before the interaction region (Pu5, red curve). At the same time some ions still remain trapped causing the oscillations on the Pu3 signal at long times. Trap settings are the same as described in Fig. 4.6.*

stored particles themselves (III). For a beam of Ar^+ these processes can be written as

$$\text{(I)} \quad Ar^+ + R^0 \longrightarrow Ar^0 + R^+ \tag{4.1}$$

$$\text{(II)} \quad Ar^+(\vec{p}_i) + R^0 \longrightarrow Ar^+(\vec{p}_f) + R^0 \tag{4.2}$$

In Reaction 4.1 a trapped ion captures an electron from a residual gas atom or molecule and leaves the trap as a neutral atom. In Reaction 4.2 the ion's initial momentum $\vec{p}_i$ is changed to $\vec{p}_f$ and the ion is lost from the trapped if scattered into an unstable orbit. Ion loss due to the second mechanism can occur after a single collision or after multiple collisions.
The third process is the collision of two stored ions with initial momenta $\vec{p}_{i,1}$ and $\vec{p}_{i,2}$ leading to Ar^+ ions with different final momenta $\vec{p}_{f,1}$ and $\vec{p}_{f,2}$ resulting in ion loss if scattering into unstable orbits occurs.

$$\text{(III)} \quad Ar^+(\vec{p}_{i,1}) + Ar^+(\vec{p}_{i,2}) \longrightarrow Ar^+(\vec{p}_{f,1}) + Ar^+(\vec{p}_{f,2}) \tag{4.3}$$

While the loss of ions from the trap due to electron capture (I) was found to be largely independent of the trap settings, the ion-loss rate due to the other two mechanisms turned out to be a complicated function of the exact trajectory of the ions inside the trap and extensive calculations would be necessary to fully understand the different contributions from each loss process. However, in their study Pedersen and co workers could conclude the following. Ion loss as a result of ion-ion scattering depends directly on the ion density and hence influences the decay curve mostly at the early times. The reduction of trapped ions because of electron capture or ion neutral scattering define the long term behavior of the decay curves with the scattering process being the largest contributor.
The brown curve in Fig. 4.6 demonstrates extraction through a hole in the exit mirror using the M1 electrode. This method of extraction is described in Ch. 3.4.5 and illustrated by simulations in Fig. 3.11. In this particular example the trap was filled with Ar^+ ions at 4.2keV beam energy and the extraction electrode (M1) was then lowered from $V_{M1} = 4600$V to 4440V for a short time of 1.6μs for 6 consecutive times. The spectrum was summed over 500 complete cycles. The short extracted ion bunches are recorded by the 0°-MCP detector producing a sharp increase in count rate. As can be seen from the spectrum in Fig. 4.6 short bunches can be extracted from the ion trap without disturbing the remaining ions inside the trap.
Fig. 4.7 shows the same extraction process recorded with the pickup electrodes situated inside the ion trap (Pu3) and Pu5 situated after the third quadrupole deflector (see Fig. 3.2). Here the signal produced by the ion bunch passing through the pickup electrode is amplified an recorded using the PC scope (see Ch. 4.1.1). The brown curve in Fig. 4.7 shows the ion bunch oscillating inside the ion trap. The switching of the M1 electrode is registered by the pickup electrodes because of electronic noise associated with it which results in sharp peaks in the

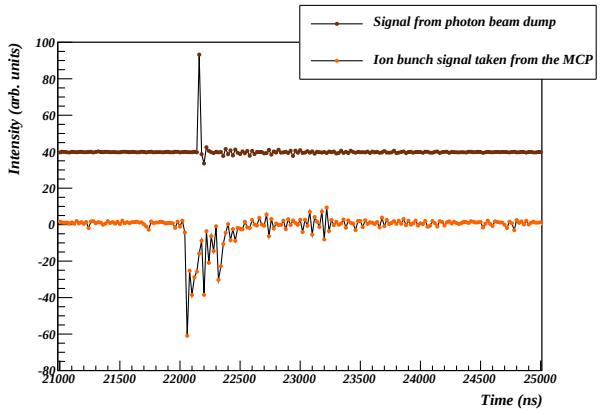

Figure 4.8: *Temporal overlap measurement. The brown curve shows the FEL laser signal taken from the photon beam dump via a charge sensitive amplifier. The lower curve is the ion bunch measured with the MCP detector. The ion signal was taken from the MCP back and fed directly into an oscilloscope.*

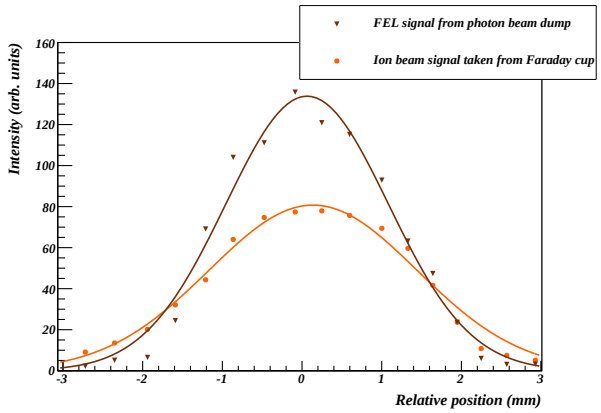

Figure 4.9: *Spatial overlap as measured by scanning a 1mm slit across the overlap region. The brown curve shows the FEL intensity as measured by the photon beam dump. The orange curve illustrates the ion beam as monitored by the Faraday cup. Each data point was averaged over approximately 10 FEL photon pulses, for the ion current measurement the ion beam was in DC mode.*

recorded spectrum. If the M1 electrode is lowered for a short time a part of the trapped ions is extracted which manifests itself by an ion bunch signal recorded by Pu5 (red curve) shortly after extraction.

4.4 Beam overlap measurements

Using the diagnostic unit described in Fig. 3.5.3 the properties of the two overlapping beams can be determine. Fig. 4.8 shows an example for how the temporal overlap is determined. The brown curve shows the signal emanating from the photon pulse impinging on the copper photon beam dump (see Fig. 3.13). The lower signal shows the ions hitting the 25mm MCP detector installed in the interaction region as taken from the back of the MCP detector. In this particular example the delay of the ion bunch was picked so that the photon pulse will strike the ion bunch in the first 100ns.

Fig. 4.9 displays the result of a scan with the 1mm slit (see Fig. 3.15) across the overlap position of photon and ion beam. Here the diagnostic unit was scanned slowly around the position of the 1mm slit and the photon beam and ion beam signal were recorded simultaneously. The brown curve shows the averaged photon beam signal taken from the photon measurement plate (see Fig. 3.15) as described in Ch. 3.5.3. From the FEL pulse train one exemplary micro-pulse is

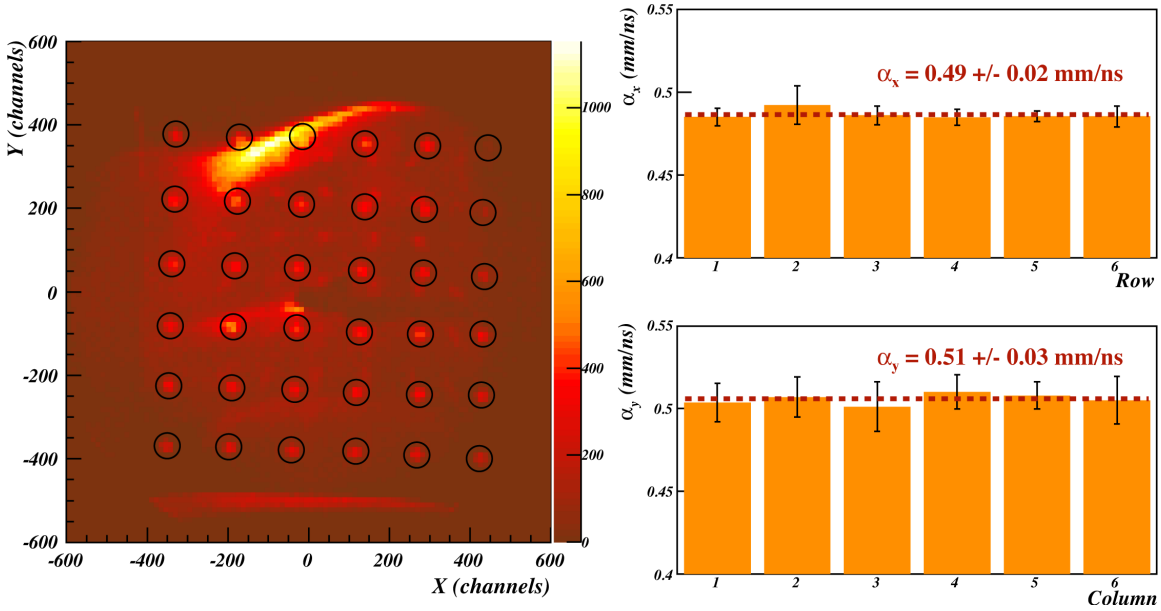

Figure 4.10: *Negative image of the calibration grid illuminated by the alpha source. The circles indicate the found positions for the calibration grid holes. From the known distance between the holes α_x and α_y can be derived. The results are plotted on the right side.*

picked and the signal height of that pulse is recorded by an analog-to-digital converter (ADC). For each datapoint the photon signal is averaged over 2s which corresponds to approximately 10 FEL micro-pulses. The ion beam signal was measured by dumping the beam onto an insulated biased metal plate mounted behind the 1mm slit very similar to a Faraday cup. The DC ion beam current was directly measured by the pico-amperemeter.

4.5 Detector calibration

As described in Ch. 3.6 it is necessary to determine the characteristic detector calibration parameters α_x, α_y as well as the timesums S_{12} and S_{34}. Therefore a calibration grid was installed just beside the detector which can be moved in and retracted at any time from outside the vacuum chamber via a mechanical motion feedthrough of 100mm travel length. The grid is made up of a 6 x 6 matrix of 2mm holes with a 10mm spacing covering almost the complete detector. To guarantee an even illumination of the detector during calibration we also installed an Americium 241 alpha source about 2.5m upstream from the detector (see also Fig 3.2).
Fig 4.10 shows the negative image of the calibration grid illuminated by the alpha source. From the imprints left by the holes of the grid on the detector and the known grid spacing one can derive the calibration values for $\alpha_x = 0.49 \pm 0.02$mm/ns and $\alpha_y = 0.51 \pm 0.03$mm/ns. The fringes visible in the detector image indicate the problems encountered when the detector front is not

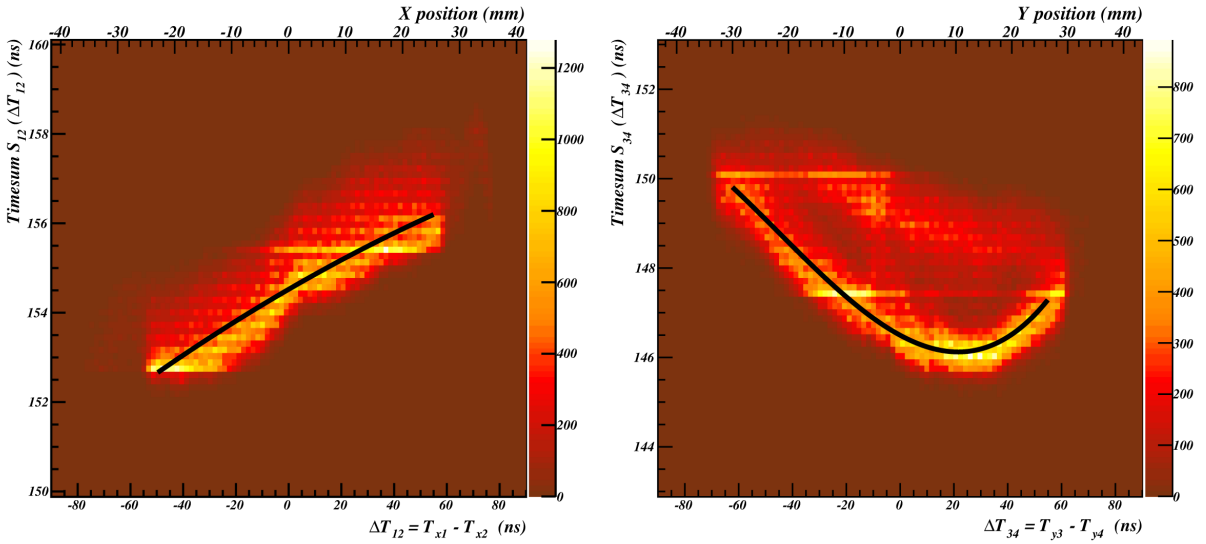

Figure 4.11: *Timesum calibration for the x- and y-positions of the detector. Plotted is the timesum S_{12} as a function of the x-position $\Delta T_{12} = T_{x1} - T_{x2}$ in ns and for completeness also in mm (see upper scale) and on the right side S_{34} as function of the y-position ΔT_{34}. The resulting calibration functions in ns scale are plotted in both graphs.*

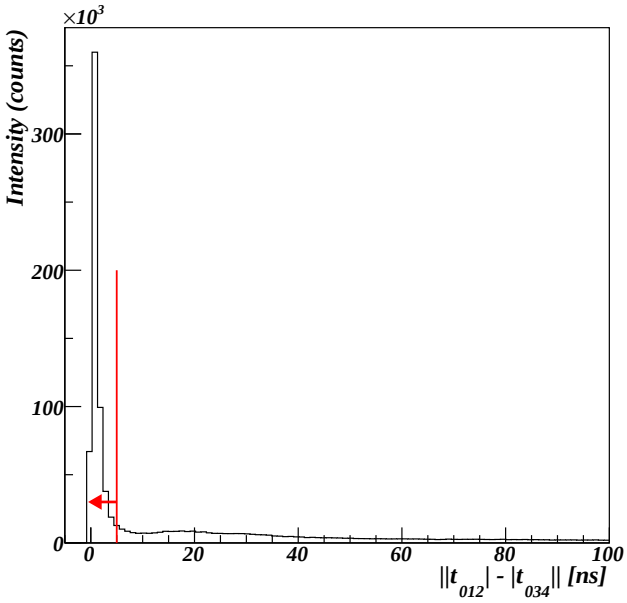

Figure 4.12: *Showcase example of the distribution of the* $||t_{012}| - |t_{034}||$ *(see also Eq. 3.14) values for one run. The red line indicates the 5ns cut performed for event validation.*

shielded by the MCP grid (see Fig 3.6). With installed MCP grid these artifacts disappear but the calibration values remain basically unchanged.

For the timesum calibration the detector is illuminated by alpha particles without the calibration grid. The start of the TDC is taken directly from the MCP back thus there is no delay due to the time of flight t_{tof} and if D_s is set to 0 the timesums turn to $S_{12}(\Delta T_{12}) = P_{x1} + P_{x2} = T_{x1} + T_{x2}$ and respectively $S_{34}(\Delta T_{34}) = P_{y3} + P_{y4} = T_{y3} + T_{y4}$ the results of these calibration runs are depicted in Fig. 4.11. A polynomial fit to both distributions yields the corresponding calibration functions $S_{12}(\Delta T_{12}) = (154.5 \pm 0.1) + (0.03 \pm 0.002)\Delta T_{12} + (-6.7 \cdot 10^{-5} \pm 5.1 \cdot 10^{-5})\Delta T_{12}^2$ and $S_{34}(\Delta T_{34}) = (146.5 \pm 0.03) + (-0.03 \pm 0.001)\Delta T_{34} + (6.1 \cdot 10^{-4} \pm 1.9 \cdot 10^{-5})\Delta T_{34}^2$.

Fig. 4.12 displays a showcase example of the distribution of the $||t_{012}| - |t_{034}||$ values used for event validity check (see also Eq. 3.14). It illustrates that a cut of 5ns on the $||t_{012}| - |t_{034}||$ value for an event is sufficient to verify the validity of that particular event. Eq. 3.14 can therefore be rephrased as

$$||t_{012}(i)| - |t_{034}(i)|| \leq 5ns. \tag{4.4}$$

5. Optical laser experiments

5.1 Rare gas dimer ions

Rare gas dimer ions and their corresponding neutral states are in general of importance for the understanding of the kinetics of rare gas excimer or rare gas halide (exciplex) systems for example in lasers. The operating principle of these laser systems is based on electron beam excitations of mixtures of rare gases and rare gases containing amounts of halogen gas. These excitations eventually lead to the formation of the excited rare gas molecules or rare gas halide complexes through kinetic processes. These excimers or exciplexes decay and emit laser radiation in the UV. However, it was discovered that also significant concentrations of rare gas dimer ions are formed through the same excitation processes [38, 43]. These dimer ions were thought to act as a gain inhibitor because of indications of strong photoabsorption cross sections throughout the visible and the UV and would therefore absorb the emitted laser radiation. This observation sparked extensive research in the field of noble-gas dimer ions with emphasize put on the systems Ar_2^+ , Kr_2^+ and Xe_2^+ because of the widespread use of the parent rare gases in laser applications.

Furthermore, the rare gas dimers ions are important for understanding the structure and reactivity of large rare gas clusters. There exists experimental evidence [76, 75, 58] as well as theoretical predictions [53, 30] supporting that ionic clusters contain a dimer or trimer ion localized inside the neutral rare gas atoms.

Neglecting the spin-orbit interaction, in the so called Hund's case (b), the atomic $Ar(^1S_0)$ and $Ar^+(^2P)$ ground states correlate to four molecular electronic states of symmetry $X^2\Sigma_u^+$, $A^2\Pi_g$, $B^2\Pi_u$ and $C^2\Sigma_g^+$. The ground state of the nobel gas ion is split by spin-orbit coupling into two components, a $^2P_{3/2}$ state, which lies lowest, and a low lying $^2P_{1/2}$ state. This splitting is small in the case of Ne^+ (97meV) but is of the same magnitude as the chemical binding in the case of Xe^+ (1.3eV) [66]. In Hund's case (a) only the projection of the total angular electronic momentum ($J_z = L_z + S_z$) on the internuclear axis is a constant of motion with corresponding quantum number Ω. For the states described by $^2\Sigma$ ($\Lambda = 0, \Sigma = \pm\frac{1}{2}$) and $^2\Pi$ ($|\Lambda| = 1, \Sigma = \pm\frac{1}{2}$), spin-orbit effects lead to states with $\Omega = \frac{1}{2}, \frac{3}{2}$ which can be described by a linear combination of Σ and Π states [67, 66, 101]. For the gerade (g) states one obtains

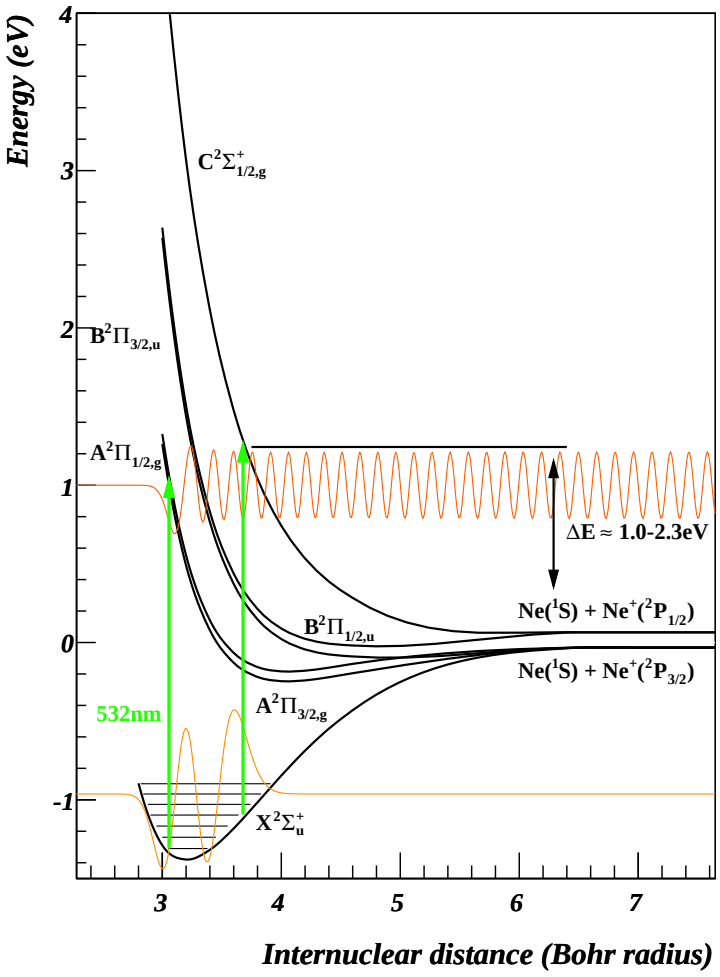

Figure 5.1: *Potential energy curves for the low doublet states of Ne_2^+ including spin-orbit coupling as calculated in [66]. The vibrational levels were calculated from the spectroscopic constants given in [66]. The green line indicates the transition induced by photons with a wavelength of 532nm. A bound wavefunction and a continuum wavefunction obtained from the Franck-Condon (see Fig. 5.22) factor calculations are indicated.*

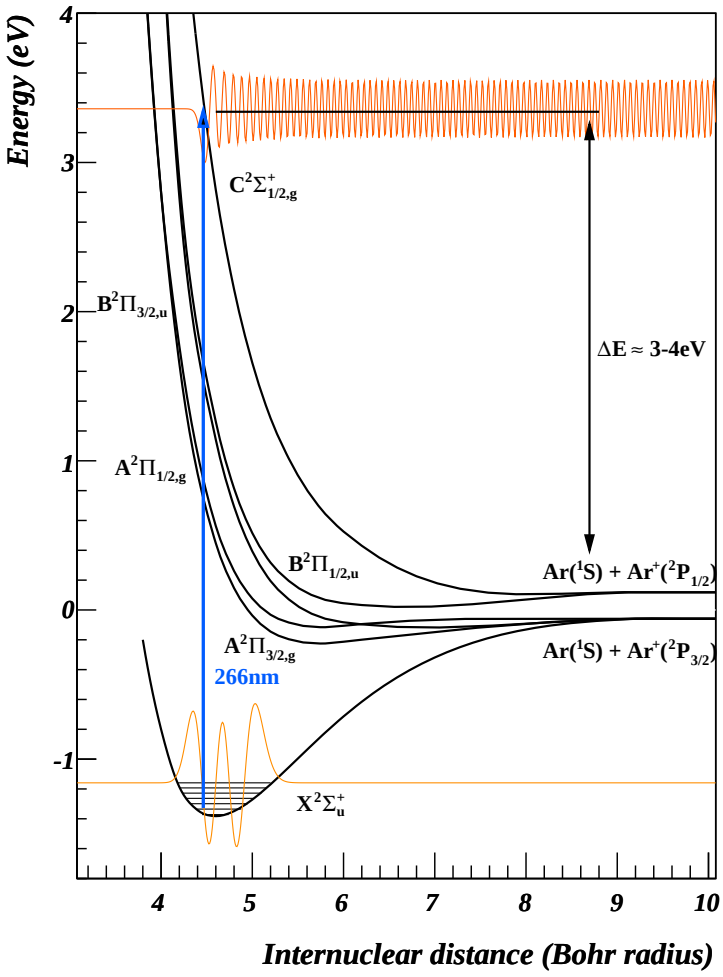

Figure 5.2: *Potential energy curves for the low doublet states of Ar_2^+ including spin-orbit coupling as calculated in [66]. The vibrational levels were calculated from the spectroscopic constants given in [66]. The blue line indicates the transition induced by photons with a wavelength of 266nm. A bound wavefunction and a continuum wavefunction obtained from the Franck-Condon (see Fig. 5.13) factor calculations are indicated.*

$$|^2\Sigma_{\frac{1}{2},g}\rangle = a_g|^2\Sigma_g\rangle + b_g|^2\Pi_g\rangle \quad (5.1)$$

$$|^2\Pi_{\frac{3}{2},g}\rangle = |^2\Sigma_g\rangle \quad (5.2)$$

$$|^2\Pi_{\frac{1}{2},g}\rangle = a'_g|^2\Pi_g\rangle + b'_g|^2\Sigma_g\rangle, \quad (5.3)$$

and respectively for the ungerade (u) states. In Hund's case (b) optical transitions of $\Delta\Lambda = 0$ are termed parallel while $\Delta\Lambda = \pm 1$ are termed perpendicular since the radiation couples to the electronic dipole moment parallel or perpendicular to the internuclear axis. If the dissociation is prompt, parallel transitions lead to angular distributions with $\beta = 2$ while perpendicular transitions lead to angular distributions of $\beta = -1$ (see Ch. 2.4). The spin-orbit induced states defined by the coefficients a_g, b_g, a'_g and b'_g will thus manifest themselves in the angular distribution of the photofragments since transitions involving these $\Omega = \frac{1}{2}$ states now gain a contribution of both $\Delta\Lambda = 0$ and $\Delta\Lambda = \pm 1$.

Theoretical calculations of the potential energy curves have been carried out using various ab initio approaches for instance in the case of Ar_2^+ [111, 66] or for Ne_2^+ [66, 19, 64]. Theoretically calculated potential energy surfaces are displayed in Fig. 5.1 in the case of Ne_2^+ and Fig. 5.2 for Ar_2^+ [66]. The lowest state, usually labeled $X^2\Sigma_u^+$, is bound for the four systems Ne_2^+, Ar_2^+, Kr_2^+ and Xe_2^+. The higher lying $C^2\Sigma_g^+$ state is purely repulsive while latest calculations on the $B^2\Pi_u$ and $C^2\Pi_g$ states show them to be slightly binding having a binding energy of 70-170meV in the case of Ne_2^+ and 60-100meV for Ar_2^+ [66, 64].

The low lying electronic states of Ar_2^+ were extensively studied in ion-atom scattering experiments by for example Lorents et. al [61] or experiments conducted by Jones and co workers [47]. From the values of the observed rainbow scattering angel they were able to report first experimentally determined results for binding energy of the system. Further information about the Ar_2^+ potential curves and absolute photodissociation cross sections were acquired using photofragment spectroscopy at a wide range of wavelengths. In the UV by Vanderhoff [109], in the visible regime by Lee [56], Miller [69] and Moseley [74] and in the infrared by Duffy [29] and Woodward [112]. More recently, results form photoelectron spectroscopy were obtained by Signorell et al. [98].

For Ar_2^+ theoretical values were also obtained for the photoabsorption cross sections for the bound-free transitions from the $X^2\Sigma_u^+$ ground state to the repulsive $A^2\Pi_g$ and $C^2\Sigma_g^+$ states. For the $\Sigma \rightarrow \Pi$ transition Stevens and co workers [101] arrived at a value of $2.6 \cdot 10^{-19}\text{cm}^2$ at 716nm and for the $\Sigma \rightarrow \Sigma$ transition they calculated a value of $5.0 \cdot 10^{-17}\text{cm}^2$ at 300nm.

The Ne_2^+ dimer ion has received limited attention. Attempts to measure the photodissociation cross section in the visible regime by the above mentioned studies by Lee [56] and Miller [69] failed due to the lack of detectable photofragments and only upper limits could be given. The binding energy of the system was determined in scattering experiments [70], photoionization studies of Neon dimers [105] and lately also using photodissocation [19]. The obtained results

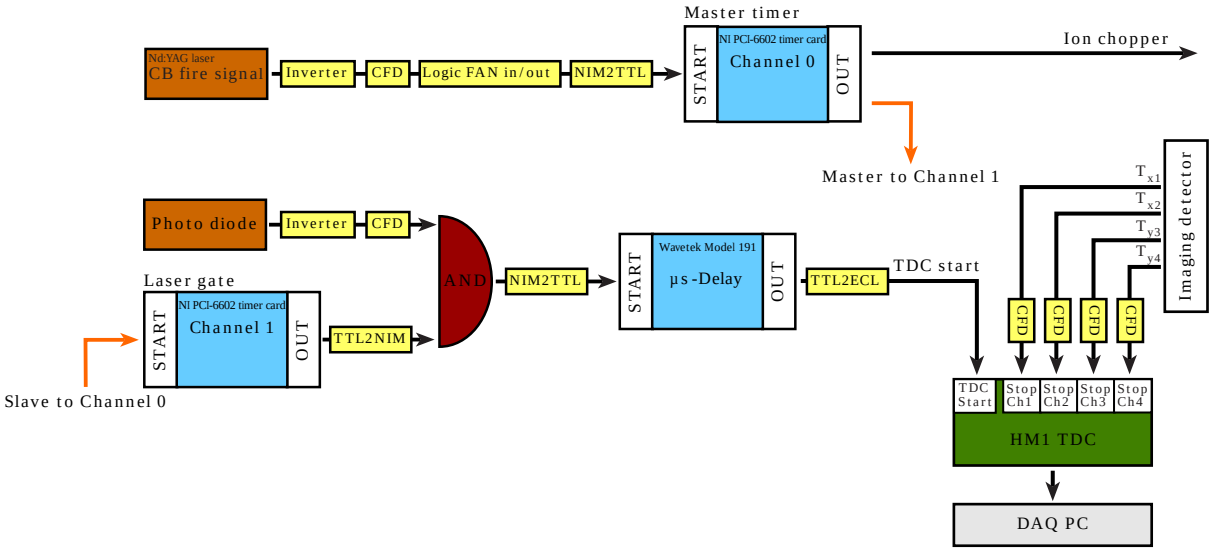

Figure 5.3: *Schematic timing and data acquisition diagram used in the optical laser photodissociation experiments conducted in Heidelberg.*

are in good agreement with the theoretical values calculated in [19].

Previous experiments have been very successful in determining the shape and dimensions of the potential energy surfaces involved in the dissociation process. Detailed results were also obtained on the magnitude of the absolute cross sections of the dissociation process and the wavelength dependence. However due to the applied method of detection of the photofragments (see also Ch. 2.2) only limited data on the angular distribution of photofragments could be extracted from these experiments.

With the angular distributions of fragments resulting from photodissociation reactions directly measurable more insight can be gained into the magnitude and character of the aforementioned spin orbit effects. Comparing the different contributions to the angular distributions can thus test theoretical predictions on the mixing coefficients.

5.2 Timing and data acquisition

Fig. 5.3 shows a schematic of the experimental timing and data acquisition used for the studies performed on Ar_2^+ and Ne_2^+ using the optical laser (see Ch. 3.7.1). The flash lamp trigger pulse (CB fire signal) originating from the Nd:YAG laser comes 155μs before the laser pulse is emitted. The signal is processed as indicated in Fig. 5.3 and triggers the master timer (Channel 0) situated on the PCI timer card (compare to Ch. 4.1.1). The master timer controls the beam chopper (see Ch. 3.2.5) and triggers the laser gate (Channel 1) at the same time. The fast photo diode signal which registers the light pulse emitted by the laser is processed and anded with the laser gate

	Ar_2^+ photodissociation	Ne_2^+ photodissociation
Master timer (Ch. 0) delay:	98μs	56μs
Master timer (Ch. 0) width:	5μs	6μs
Laser gate (Ch. 1) delay:	56μs	32μs
Laser gate (Ch. 1) width:	4μs	6μs
TDC delay	6.995μs	5.419μs

Table 5.1: *Timer settings for the optical laser experimtens.*

signal trigger by channel 0. The resulting signal triggers the Wavetek function generator which effectively delays the signal for several μs before starting all four TDC channels, to account for the time of flight of the photofragments. The arrival times of the respective stop signals T_{x1}, T_{x2}, T_{y3} and T_{y4} (see also Ch. 3.6) are recorded and the data is transferred to the DAQ PC. The repetition rate of the experiment is defined by that of the Nd:YAG laser which can be either 40Hz or 50Hz. The individual timer settings are displayed in Tab. 5.1.

5.3 Photodissociation of Ar_2^+ at 266nm

5.3.1 Experimental parameters

A beam of Ar_2^+ ions was produced with the hollow cathode ion source (see Ch. 3.3 and Ch. 4.2) totaling to a DC current of ≈400pA in the interaction region. The ion beam was pulsed using the ion trap yielding a bunch width of 5μs.
Laser pulses at a wavelength of 266nm emitted from the Nd:YAG laser (see Ch. 3.7.1) were overlapped with the Ar_2^+ ion bunch at a 90° angle. The laser polarization was perpendicular the the ion beam direction. The average pulse energy per laser shot was 0.75mJ.
In total this corresponds to $1.0 \cdot 10^{15}$ UV photons per pulse interacting with typically 25 Ar_2^+ ions assuming an average length of the laser pulse of 9ns. The experiment was triggered by the laser as illustrated in Fig. 5.3 giving a repetition rate of 40Hz.

5.3.2 Fragment imaging

Neutral fragments produced in the crossing of laser beam and ion beam proceed to the time and position sensitive imaging detector (see also Ch. 3.6.2) situated about 850mm downstream. In addition to the laser induced signal, collisional dissociation of the molecular ions in the residual gas ($3 \cdot 10^{-9}$mbar) produced a background of neutrals on the detector. Data was recorded for ≈11 hours.

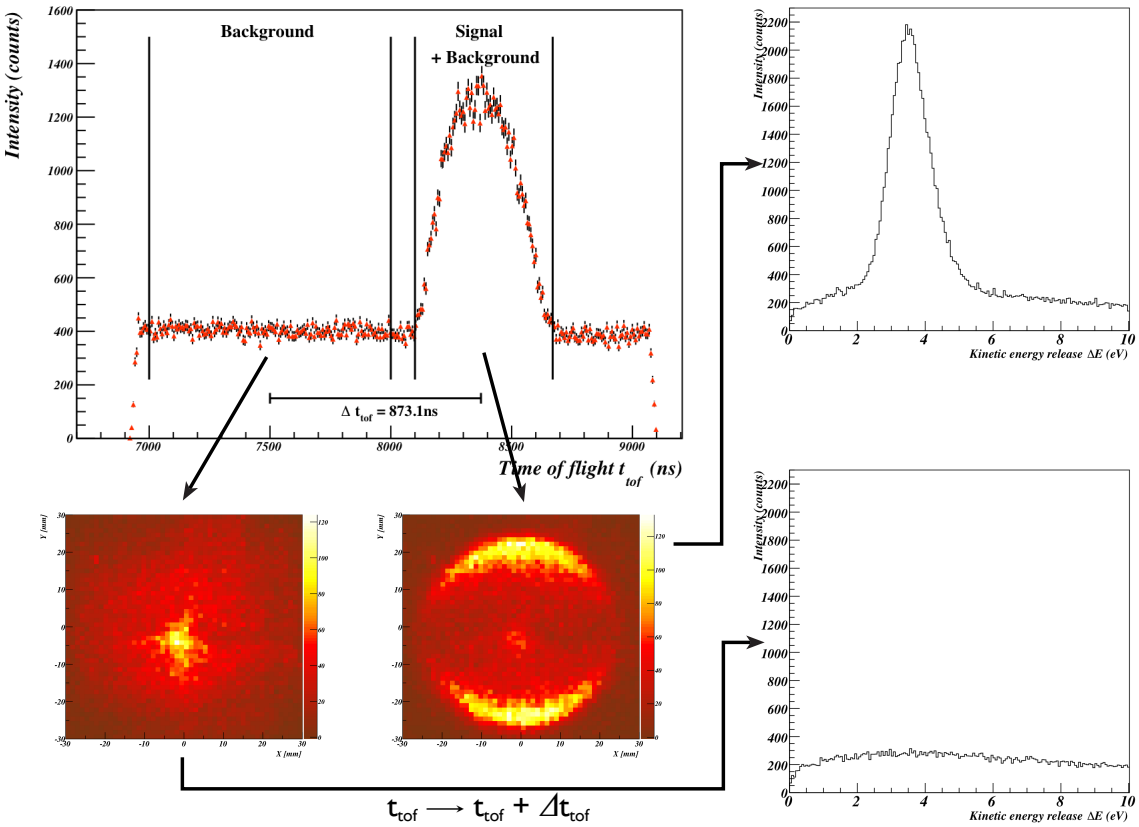

Figure 5.4: *Time of flight t_{tof} spectrum of the neutral Argon fragments. The method for obtaining the background estimate is described. The background spectrum is extracted from time of flight values of* 7000ns $\leq$ t_{tof} $\leq$ 8000ns *and then shifted to coincide with the mean arrival time of the signal events. The resulting kinetic energy release distributions are displayed on the right.*

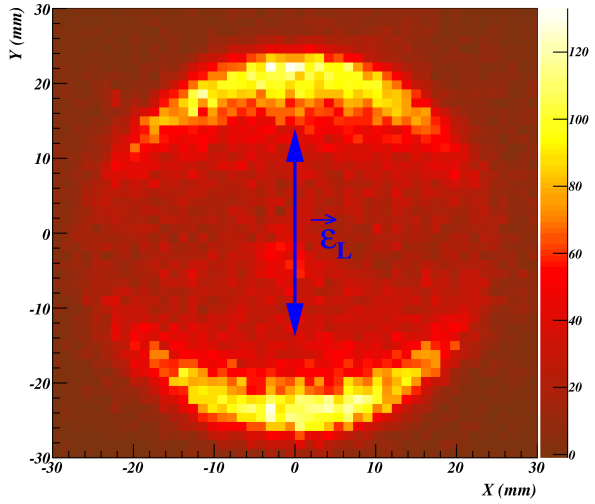

Figure 5.5: *2D detector image of the neutral Argon photofragments measured by the imaging detector. The blue arrow indicates the laser polarization which is perpendicular to the ion beam direction.*

In the upper left part of Fig. 5.4 a time of flight spectrum of the Ar^0 fragments is shown. The t_{tof} spectrum shows a clear photon induced signal at a mean time of flight value of ≈8300ns. The ion bunch length is relatively long (5μs) and the ion density distribution in the bunch is uniform, hence the characteristics of events with time of flight values different from the signal events are similar to the background at the time of flight where the signal is observed. Thus, the background was extracted from neutral fragments having a time of flight value ranging from 7000ns to 8000ns as illustrated in Fig.5.4. 2-dimensional detector pictures corresponding to each region of the time of flight are displayed in the lower part of Fig.5.4. The kinetic energy release and angular distributions were obtained by shifting the time of flight value by $\Delta t_{tof} = 873.1ns$ to match the flight time of the signal plus background events. Resulting kinetic energy release spectra are also displayed in Fig. 5.4.

An enlarged X-Y distribution of the signal plus background events (8.1μs $\leq t_{tof} \leq$ 8.67μs) is displayed in Fig. 5.5. The arrow in Fig. 5.5 illustrates the direction of the laser polarization $\vec{\varepsilon}_L$.

A 3-dimensional representation of the experimental data is given in Fig. 5.6. Here the time of flight t_{tof} of the Ar^0 fragments is plotted versus the squared radial position $R^2 = (X - X_0)^2 + (Y - Y_0)^2$ on the detector where X_0 and Y_0 constitute the position of the beam center.

By inversion of the equation for the kinetic energy release (Eq. 2.30) one obtains

$$R^2 = \frac{2\mu\Delta E}{M^2} \cdot t_{tof}^2 - (L - v_{ion} \cdot t_{tof})^2. \tag{5.4}$$

Using Eq. 5.4 and the values for the ion kinetic energy $E_{ion} \approx$ 4200keV and the distance between interaction point and detector L ≈ 850mm curves indicating the expected kinetic energy release 3eV≤ ΔE ≤4eV (see Fig. 5.2) are drawn. Fig. 5.6 shows an amassing of neutral Argon fragments with high R^2 values fulfilling the indicated condition on the kinetic energy release.

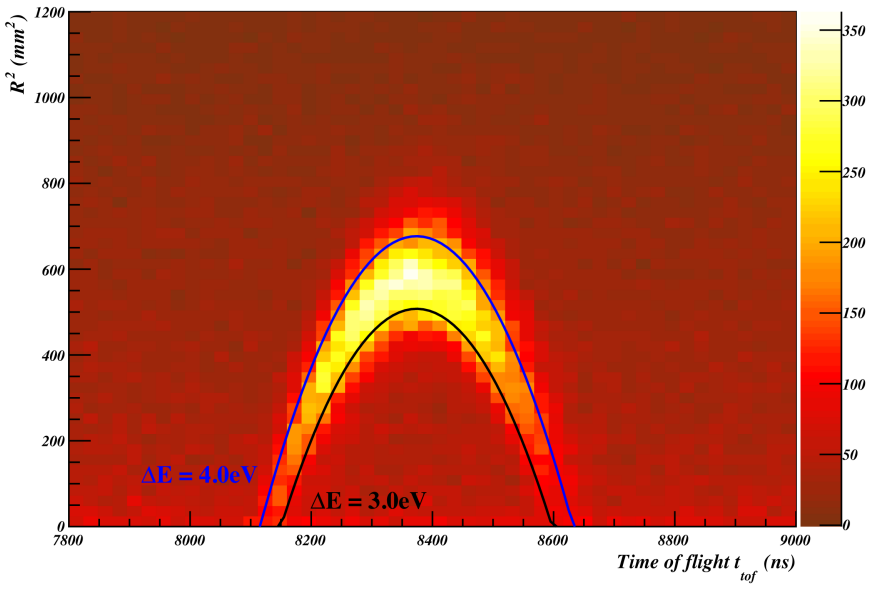

Figure 5.6: *R^2 versus time of flight t_{tof} distribution for Ar^0 fragments resulting from Ar_2^+ photodissociation at 266nm. The lines indicate R^2 values for constant kinetic energy release of $\Delta E = 3eV$ and $\Delta E = 4eV$*

5.3.3 Kinetic energy release and angular distributions

From the radial position of the fragments on the imaging detector and the time of flight the kinetic energy release was calculated using Eq. 2.30. The kinetic energy release obtained from the Ar^0 fragments emerging from Ar_2^+ photodissociation after background subtraction is depicted in Fig. 5.7 showing a single peak centered around 3.5eV.

The range of the energy release is consistent with a transition from the $X^2\Sigma^+_{\frac{1}{2},u}$ ground state to the $C^2\Sigma^+_{\frac{1}{2},g}$ repulsive state which decays to the $Ar(^1S)$ + $Ar^+(^2P_{1/2})$ final channel as indicated in Fig. 5.2. The kinetic energy release is related to the initial rovibrational excitation of the molecular ion as illustrated in Fig. 2.2 and is given by Eq. 2.18. Thus, high levels of internal excitation will lead to high values of the kinetic energy release.

The kinetic energy release corresponding to the individual vibrational levels of the ion was calculated with the spectroscopic constants given in [66] for the two possible final channels of the dissociation process. The results are included in Fig. 5.7. Thus, the extension of the high energy edge up to ≈5.0eV can be attributed to the presence of highly excited Ar_2^+ ions. This should be expected since no cooling was applied to the Ar_2^+ ions prior to dissociation and the ion production mechanism in the ion source should lead to high levels of internal excitation. The position resolution of the detector corresponds to ±0.1mm while the uncertainty in the arrival time of the fragments is ±10ns due to the length of the laser pulse. This leads to an energy resolution of dE ≈0.5eV. Since the vibrational spacing of Ar_2^+ is only on the order of several 10meV (e.g. the difference between $\nu = 0$ to $\nu = 1$ equals to 37meV) individual vibrational levels should not be resolved. Additionally, the uncertainty in energy is evident through the extension of the low energy edge of the ΔE spectrum.

The dissociation angles relative to the laser polarization were obtained by first evaluating the angle θ_z between the z-axis and the axis of dissociation in the cm-frame of the molecule according to Eq. 2.29. The angle between polarization direction and molecular orientation θ_L was obtained by turning the coordinate system according to Eq. 2.34. The angular distributions are bound to be symmetric to the axis defined by $\theta_L = \frac{\pi}{2}$. Thus, the resulting distributions were symmetrized to compensate for detector inefficiencies by randomly assigning the sign of the right side in equation Eq. 2.34.

The angular distributions for the background events were obtained in the same way. The resulting spectra were then subtracted from the signal distributions. Fig. 5.8 shows the angular distributions after background subtraction for different regions of the kinetic energy release.

The angular distributions are obviously different for different range of kinetic energy release: with increasing energy release the valley between the two distinct lobes of the distribution observed in Fig. 5.8 a) slowly fills up until the depth of the valley is about half the peak height for high kinetic energy release (Fig. 5.8 f)).

To quantitatively characterize the angular distributions two different models were fitted to the

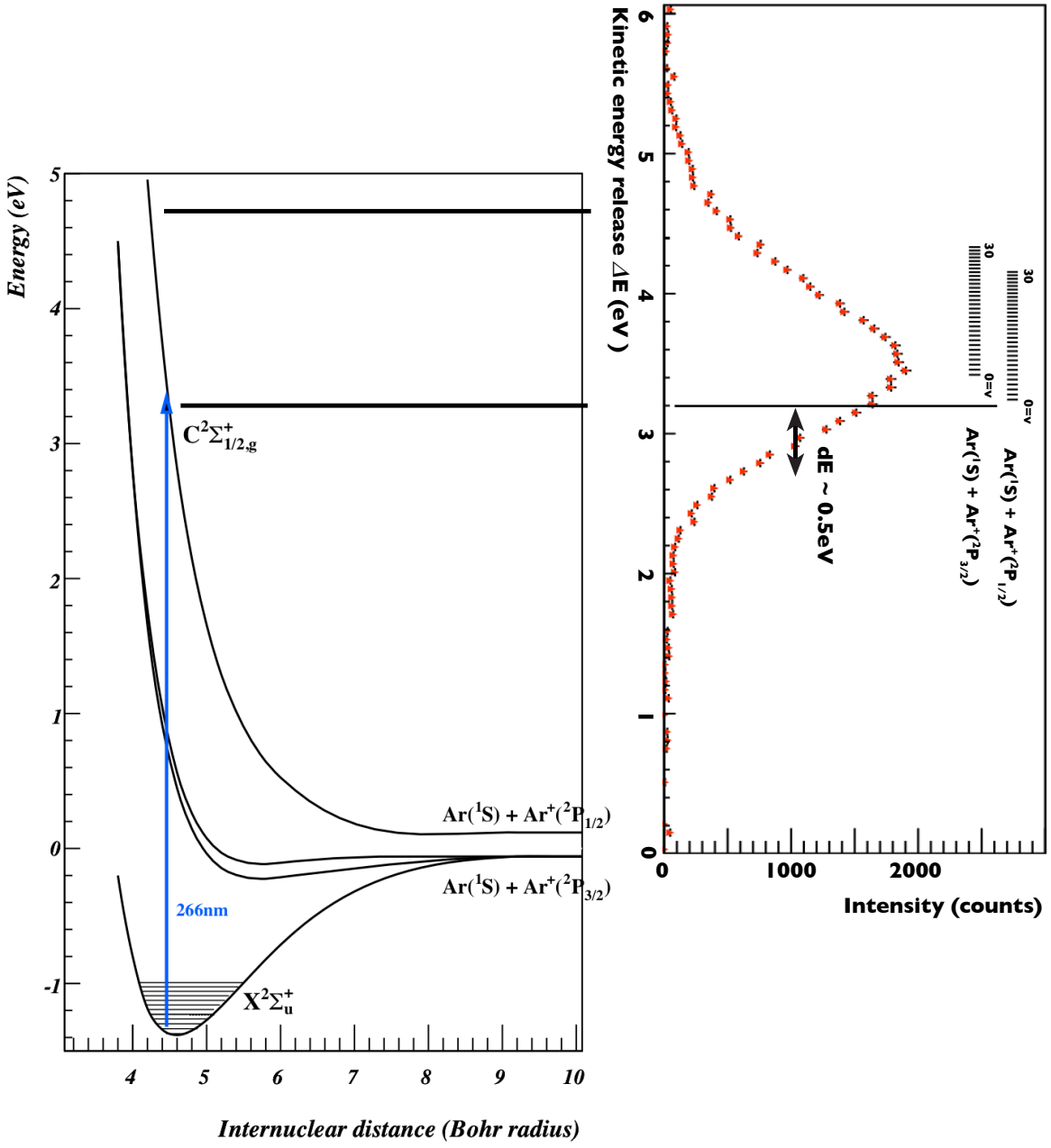

Figure 5.7: *Potential diagram for Ar_2^+ photodissociation and the measured kinetic energy release ΔE distribution of neutral Argon fragments emerging from Ar_2^+ photodissociation at 266nm. The kinetic energy release corresponding to the vibrational levels of the two final states are indicated.*

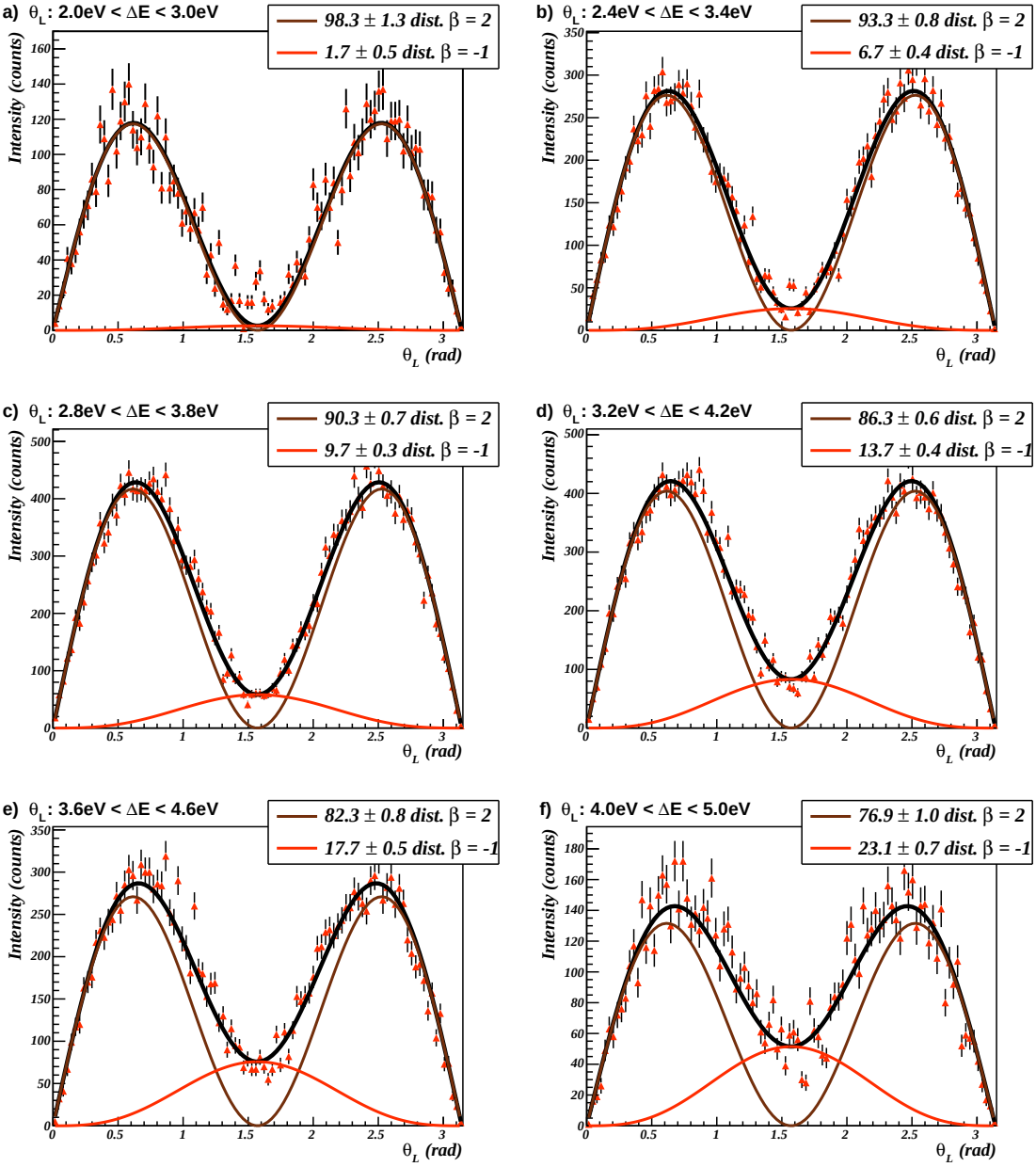

Figure 5.8: *Distribution of Ar_2^+ dissociation angle relative to the laser polarization for different cuts on the kinetic energy release. Background was subtracted for each slice of the energy release. θ_L denotes the angle between the direction of dissociation and the laser polarization $\vec{\varepsilon}_L$. The black curve shows the fit to the distribution taking into account a $\beta = 2$, $\beta = -1$ (see also Ch. 2.4).*

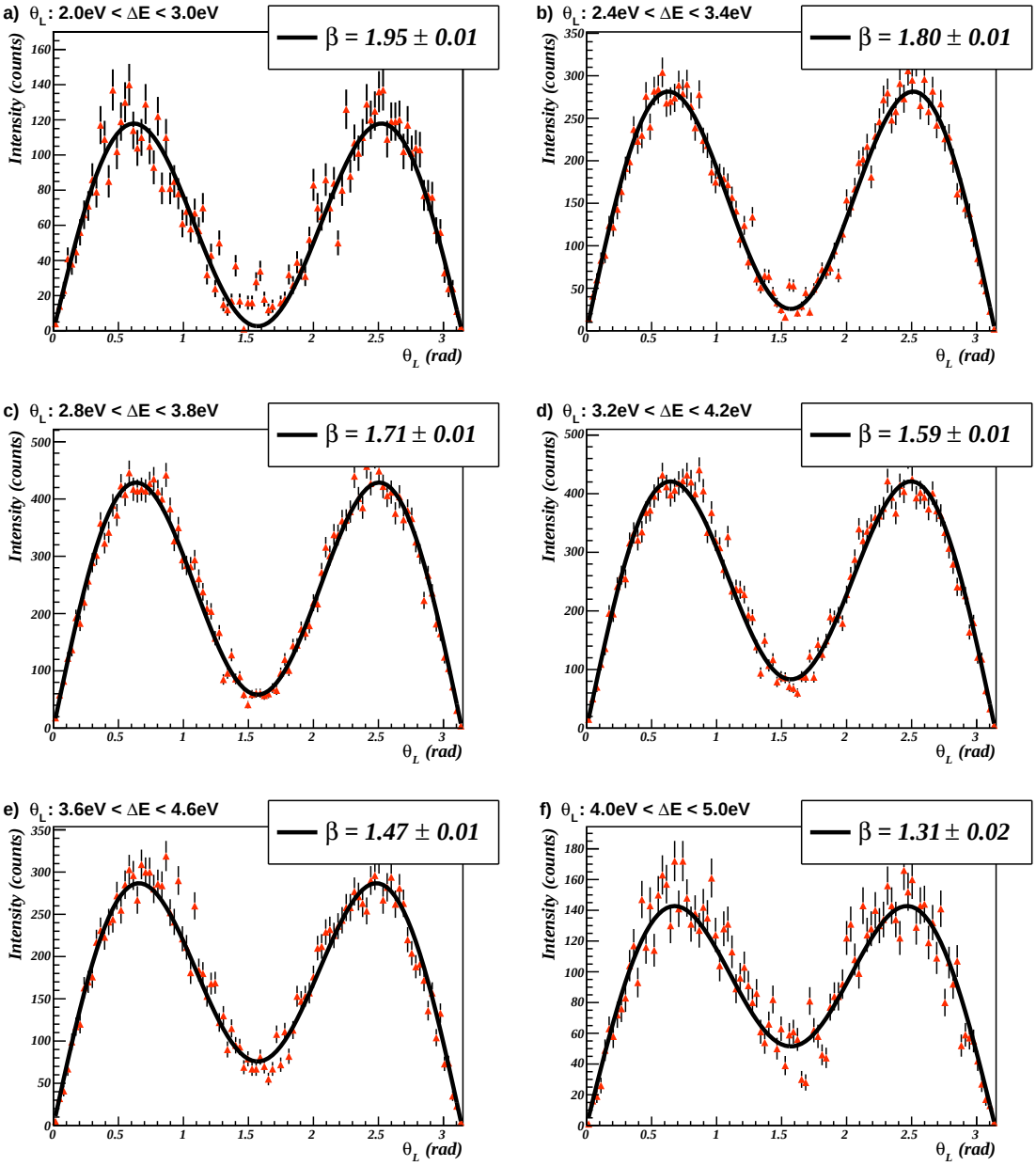

Figure 5.9: *Distribution of Ar_2^+ dissociation angle relative to the laser polarization for different cuts on the kinetic energy release. Background was subtracted for each slice of the energy release. θ_L denotes the angle between the direction of dissociation and the laser polarization $\vec{\varepsilon}_L$. The black curve shows the fit to the distribution taking into account a free β parameter.*

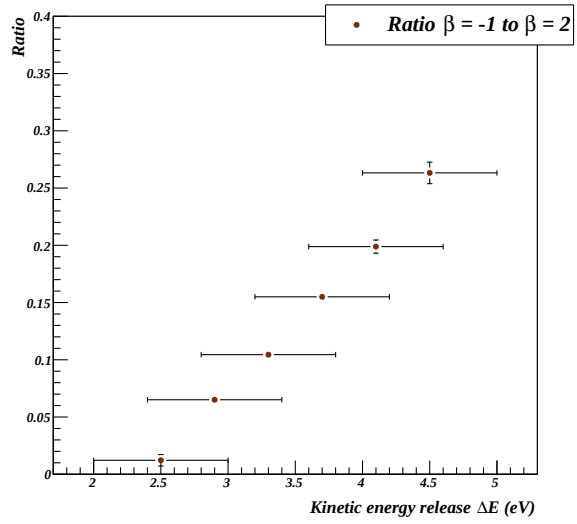

Figure 5.10: *Ratio of the $\beta = -1$ contribution to the $\beta = 2$ contribution versus kinetic energy release ΔE obtained from the fits in Fig. 5.8.*

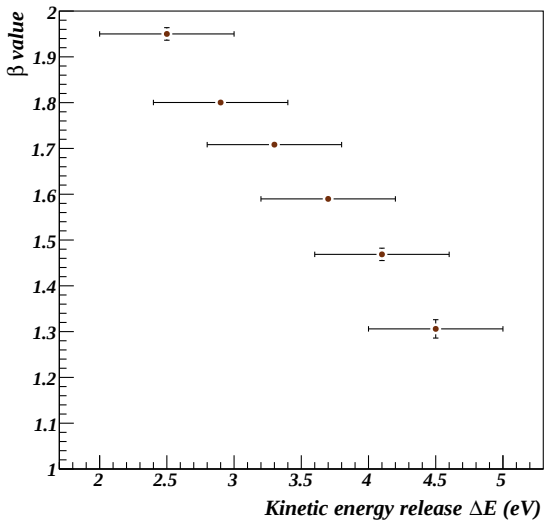

Figure 5.11: *Energy dependence of the β parameter obtained in the fits in Fig. 5.9.*

experimental data depicted in Fig. 5.8.
The first model assumes that the distribution originate from pure perpendicular and parallel transitions and takes the from

$$P_{model1}(\theta_L) = a_{-1} \cdot I(\beta = -1, \theta_L) + a_2 \cdot I(\beta = 2, \theta_L), \tag{5.5}$$

where the angular distributions were fitted with a_{-1} and a_2 as free parameters and $I(\beta, \theta_L)$ are the theoretical distributions given in Eq. 2.33. The results of the fit with model 1 are indicated by the black curves in Fig. 5.8 while the red and brown curves indicate the individual contributions of $\beta = -1$ and $\beta = 2$.
The second model takes into account a angular distribution given by Eq. 2.33 were beta is not kept fixed in the fit. Thus, the fit function can be formulated as

$$P_{model2}(\beta, \theta_L) = a \cdot I(\beta, \theta_L). \tag{5.6}$$

The obtained curves for different regions of the kinetic energy release are displayed in Fig. 5.9 with the resulting dependence of the β parameter on the kinetic energy release depicted in Fig. 5.11. The fit results show an decreasing anisotropy parameter for higher kinetic energy release values.
The results of both methods are shown in Fig. 5.10 and Fig. 5.11. For model number one the angular distributions show an increasing contribution of perpendicular dissociation for increasing kinetic energy release. The ratio $\frac{a_{-1}}{a_2}$ between $\beta = -1$ and $\beta = 2$ versus kinetic energy release is shown in Fig. 5.10.
For the second model one finds for the anisotropy parameter β a value of 1.84 for the lowest kinetic energy region. With increasing energy release the β parameter decreases until it reaches a value of 1.31 for the very high kinetic energy release.

5.3.4 Discussion

The observed angular distributions for a transition from the $X^2\Sigma^+_{\frac{1}{2},u}$ ground state of the Argon dimer ion to the $C^2\Sigma^+_{\frac{1}{2},g}$ repulsive state should have dominantly $\beta = 2$ character. For the lowest kinetic energy region (Fig. 5.8 a) and Fig. 5.9 a)) the findings agree more or less with the expected value of a pure parallel transition. However, the fits to the angular distributions conducted for both models show a striking deviation from the expected β value for increasing internal excitation of the molecular ions, i.e. for increasing kinetic energy release. It was carefully checked that neither the finite angular resolution nor a false assignment of the laser polarization was the origin of this effect.
If the molecular ion would rotate before the dissociation was completed a pure $\beta = 2$ distribution would appear to have a perpendicular component. To judge the effect of rotations on the dissociation process a classical calculation was conducted on the dissociation time of the

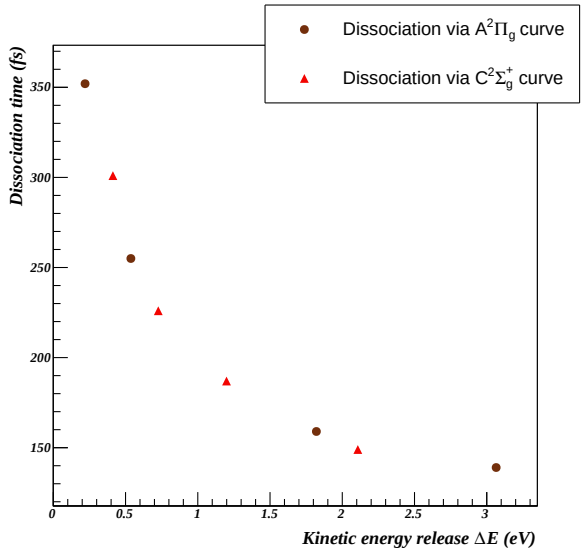

Figure 5.12: *Estimated dissociation time for the two repulsive states in the Ar_2^+ system versus kinetic energy release ΔE.*

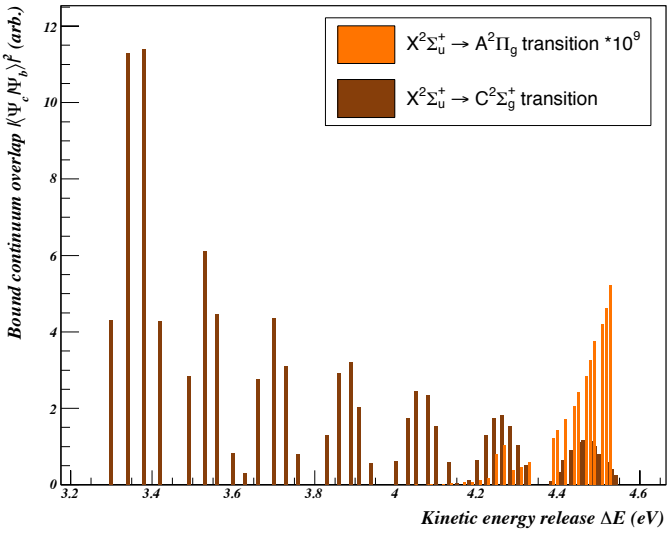

Figure 5.13: *Calculations of the Franck-Condon factors for the transitions from individual vibrational wavefunctions of the ground state to the continuum wavefunctions of the $A^2\Pi$ and $C^2\Sigma^+$ state. Please note that the factors for the $\Sigma \rightarrow \Pi$ overlap are scaled by a factor of 10^9 and shifted to lower energies by 0.01eV for better visibility.*

Ar_2^+ fragments. Thus, the Ar_2^+ ions were propagated on the potential energy surfaces $A^2\Pi_g$ and $C^2\Sigma_g^+$ displayed in Fig. 5.2. The molecular ion was assumed to be fully dissociated when the internuclear distance exceeded 10 Bohr radii. The dissociation time obtained from these calculations for the two dipole-allowed transitions from the ground state, namely $X^2\Sigma_u \rightarrow A^2\Pi_g$ and $X^2\Sigma_u \rightarrow C^2\Sigma_g$, are depicted in Fig. 5.12 as a function of the kinetic energy release. Typical dissociation times are on the order of 120-350fs and they show an inverse dependence on the energy released in the dissociation process. Hence, dissociation is in indeed faster if the molecular ion is initially at short internuclear distances. Since the energy dependence of the ratio of $\beta = -1$ to $\beta = 2$ (see Fig. 5.10) and the β trend observed in Fig. 5.11 anti correlate to the dissociation time, the deviations from pure $\beta = 2$ distributions cannot be attributed to a rotational effect. Furthermore, typical rotation times for the Ar_2^+ ions calculated using the rotational constant given in [66] are 57.4ps for the J = 1 level and 7.4ps for the J = 10 level and are thus significantly longer than the estimated dissociation times.

Another possible source for a perpendicular dissociation could arise if transitions to the $A^2\Pi_g$ states would occur. The Franck-Condon factors for the overlap of the bound wavefunctions to the continuum wavefunctions of the $A^2\Pi_g$ and the $C^2\Sigma_g^+$ were calculated [80] for the potential energy surfaces published in [66]. The Franck-Condon factors are decisive for the strength of the transition (see Ch. 2.1.2) and a comparison of these factors for individual vibrational levels should thus give insight into the relative contribution of the two possible transitions.

The calculated bound-continuum overlap factors are displayed in Fig. 5.13 where the brown bars indicate the strength of the $X^2\Sigma_u^+ \rightarrow C^2\Sigma_g^+$ transition and the orange bars show the strength of the $X^2\Sigma_u^+ \rightarrow A^2\Pi_g$ transition multiplied by a factor of 10^9 for better visibility. The overlap factors for the $X^2\Sigma_u^+ \rightarrow C^2\Sigma_g^+$ decrease as a function of kinetic energy release

while the $X^2\Sigma_u^+ \rightarrow A^2\Pi_g$ transition strength only picks up at high kinetic energy release of 4.2eV. Evidently, the $X^2\Sigma_u^+ \rightarrow C^2\Sigma_g^+$ transition are several orders of magnitude stronger than the $X^2\Sigma_u^+ \rightarrow A^2\Pi_g$ transition throughout the range of kinetic energy release observed in the experimental data (see Fig. 5.7). Thus, it is unlikely that the perpendicular dissociation observed in the angular distributions can be attributed to transitions to the $A^2\Pi_g$ states.
In conclusion, it seems evident that the observed photodissociation of Ar_2^+ originates solely from the $X^2\Sigma^+_{\frac{1}{2},u} \rightarrow C^2\Sigma^+_{\frac{1}{2},g}$ transitions and that the measured perpendicular contribution result from the mixing of $|\Pi\rangle$ character into $X^2\Sigma^+_{\frac{1}{2},u}$ ground state and the $C^2\Sigma^+_{\frac{1}{2},g}$ excited state due to spin orbit effects as mentioned in Ch. 5.1.

5.3.5 Comparison to theoretical calculations

Following the description in Ch. 5.1 the functions for the $X^2\Sigma^+_{\frac{1}{2},u}$ ground state and the $C^2\Sigma^+_{\frac{1}{2},g}$ can be formulated as a linear combination of $|^2\Pi\rangle$ and $|^2\Sigma\rangle$ states and one obtains:

$$|^2\Sigma_{\frac{1}{2},u}\rangle = a_u|^2\Sigma_u\rangle + b_u|^2\Pi_u\rangle \quad (5.7)$$
$$|^2\Sigma_{\frac{1}{2},g}\rangle = a_g|^2\Sigma_g\rangle + b_g|^2\Pi_g\rangle. \quad (5.8)$$

The matrix elements of the electronic dipole operator for the $^2\Sigma_u \rightarrow {}^2\Sigma_g$ transition in terms of spin-orbit mixed electronic states are

$$T_0 = \langle^2\Sigma_u^+|\mu_0|^2\Sigma_g^+\rangle \quad (5.9)$$
$$T_1 = \langle^2\Sigma_u^+|\mu_{\pm1}|^2\Sigma_g^+\rangle, \quad (5.10)$$

where μ is the dipole operator in the molecule fixed coordinate frame. The matrix elements T can be reformulated using the wavefunction representation given in Eq. 5.7 and Eq. 5.8 and one obtains

$$T_0 = a_u a_g\langle^2\Sigma_u^+|\mu_0|^2\Sigma_g^+\rangle + b_u b_g\langle^2\Pi_u|\mu_0|^2\Pi_g\rangle \quad (5.11)$$
$$T_1 = a_u b_g\langle^2\Sigma_u^+|\mu_{+1}|^2\Pi_g\rangle + b_u a_g\langle^2\Pi_u|\mu_{-1}|^2\Sigma_g^+\rangle. \quad (5.12)$$

The mixing coefficients a and b and the dipole transitions moments for the non spin-orbit split states $\langle^2\Sigma_u^+|\mu_0|^2\Sigma_g^+\rangle$, $\langle^2\Pi_u|\mu_0|^2\Pi_g\rangle$, $\langle^2\Sigma_u^+|\mu_{+1}|^2\Pi_g\rangle$ and $\langle^2\Pi_u|\mu_{-1}|^2\Sigma_g^+\rangle$ were published for different values of the internuclear distance R in the article by Stevens et al. [101] and are displayed in Tab. 5.2 and Tab. 5.3.
The individual strength of the bound-continuum transitions ignoring the effect of rotations is then given by the matrix elements $|\langle\chi_\nu(R)|T_0|\chi_c(R)\rangle|^2$ for the perpendicular transition and

	$X^2\Sigma^+_{\frac{1}{2},u}$		$C^2\Sigma^+_{\frac{1}{2},g}$	
R (Bohr)	a_u	b_u	a_g	b_g
4.00	0.99987	0.01611	0.99979	-0.02035
4.25	0.99979	0.02056	0.99969	-0.02496
4.50	0.99966	0.02613	0.99952	-0.03092
4.75	0.99945	0.03306	0.99925	-0.03861
5.00	0.99913	0.04165	0.99881	-0.04880
5.50	0.99786	0.06536	0.99695	-0.07809
6.50	0.98838	0.152	0.97734	-0.21166
7.00	0.97549	0.2203	0.94217	-0.33514

Table 5.2: *Ar_2^+ spin-orbit mixing coefficients taken from [101].*

R (Bohr)	$\langle {}^2\Sigma^+_u \lvert \mu_0 \rvert {}^2\Sigma^+_g \rangle$	$\langle {}^2\Pi_u \lvert \mu_0 \rvert {}^2\Pi_g \rangle$	$\langle {}^2\Sigma^+_u \lvert \mu_{+1} \rvert {}^2\Pi_g \rangle$	$\langle {}^2\Pi_u \lvert \mu_{-1} \rvert {}^2\Sigma^+_g \rangle$
4.00	1.974	1.955	0.066	-0.064
4.25	2.085	2.088	0.053	-0.037
4.50	2.198	2.220	0.042	-0.017
4.75	2.313	2.350	0.034	-0.004
5.00	2.432	2.478	0.028	0.005
5.50	2.676	2.733	0.020	0.014
6.50	3.184	3.237	0.012	0.016
7.00	3.441	3.489	0.011	0.014

Table 5.3: *Transition moments in atomic units taken from [101].*

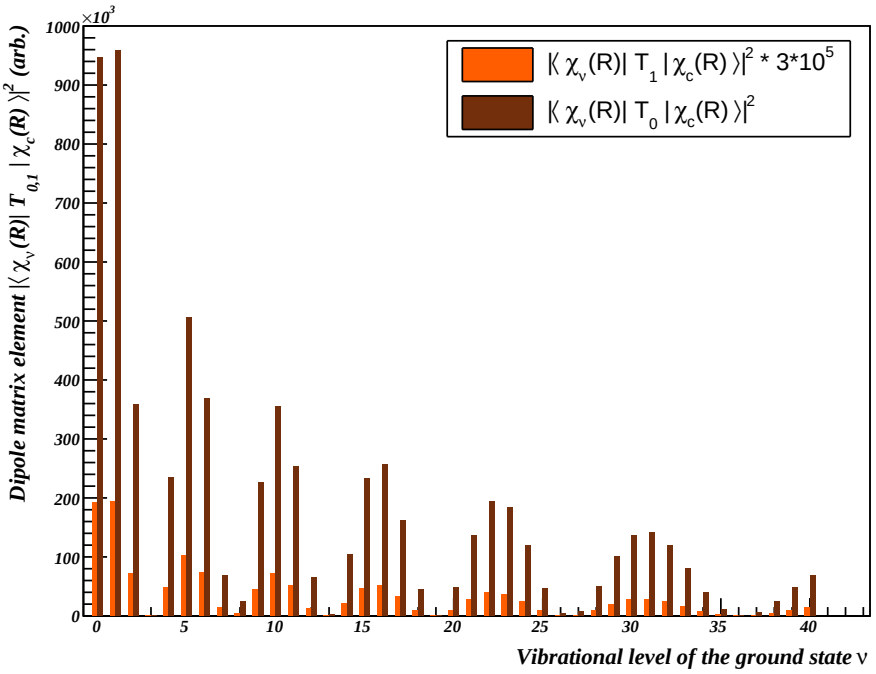

Figure 5.14: *Calculations of the individual strength of the bound-continuum transition for perpendicular and parallel transitions as a function of the initial vibrational level ν. Please note that the perpendicular dipole matrix elements have been scaled by a factor of $3 \cdot 10^5$. Both matrix element values haven been shifted by 0.15 viblevel up and down respectively for better visibility.*

$|\langle\chi_\nu(R)|T_1|\chi_c(R)\rangle|^2$ for the parallel transition, where $\chi_\nu(R)$ constitutes the wavefunction of a vibronic ground state and $\chi_c(R)$ is the wavefunction of the continuum state.
Using the wavefunctions obtained from the Franck-Condon factor calculations and the values published by Stevens et al. [101] these matrix elements can be evaluated. The results obtained from these calculations for the first 40 vibrational levels of the ground state are displayed in Fig. 5.14. Here the perpendicular matrix elements were scaled by a factor of $3 \cdot 10^5$. The dependence of the matrix elements on the initial vibrational level of the ground state is quite similar for the perpendicular case as well as the parallel transition. This is due to the fact that the bound and continuum wavefunctions only constitute to the matrix elements at small internuclear separations R were the operators T_0 and T_1 are basically constant and only differ by factors. Thus, the dependence on vibrational levels is only determined by the overlap of the bound and continuum wavefunction. However, the size of the parallel matrix elements is orders of magnitude larger than for the perpendicular transition which can not explain the discrepancies observed in the angular distributions. Thus, the experimental findings show a much larger effect of the spin orbit mixing as predicted in direct calculations of the transition probabilities using the Franck-Condon overlap integrals.

5.4 Photofragmentation studies of Ne_2^+ ions at 532nm

5.4.1 Experimental parameters

Similar to the photodissociation studies performed on Ar_2^+ (see Ch. 5.3) Ne_2^+ was also a subject to investigations. Here a Ne_2^+ ion beam with an average DC beam current of 1nA, measured close to the interaction point, was extracted from the hollow cathode ion source. The ion beam was bunched using the longitudinal pulsing capabilities of the ion beam trap with a length of each pulse of about 6μs. The Ne_2^+ molecular ion beam was crossed at a 90° angle with the laser beam emitted by the Nd:YAG laser system (see Ch. 3.7.1). The wavelength used for fragmentation of the ions was 532nm with an average of 3mJ per pulse and a 40Hz repetition rate. The photons were horizontally polarized thus the direction of polarization was parallel to the ion beam direction (compare to Fig. 3.18). Overall this corresponds to $8 \cdot 10^{15}$ photons per pulse colliding with approximately 56 Ne_2^+ ions.

5.4.2 Fragment imaging

The neutral Ne^0 fragments emerging from the photodissociation reaction were recorded by the imaging detector situated downstream from the interaction region (see Ch. 3.5) while the charged photofragments and the remaining ion beam were removed from the beam pipe by the imaging deflector unit (IMD). In addition to the laser induced signal, dissociation of the Ne_2^+ ions due to collisions with residual gas particles ($8 \cdot 10^{-9}$mbar) produced a background of neutral particles

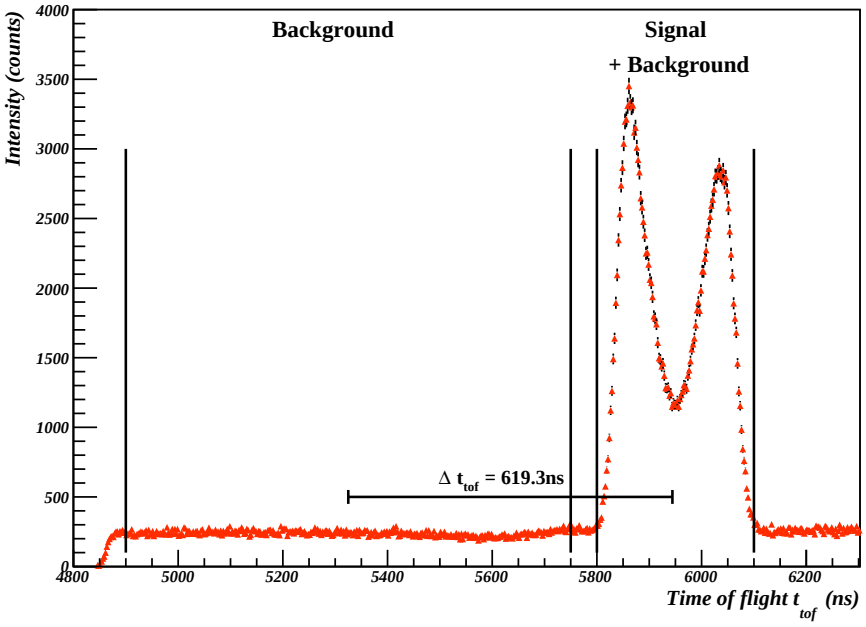

Figure 5.15: *Time of flight spectrum of the He^0 fragments resulting from photofragmentation of Ne_2^+ at 532nm.*

on the detector.

The time of flight t_{tof} spectrum of Ne^0 fragments after ≈12 hours of measurement is displayed in Fig. 5.15. In comparison to the Ar_2^+ results the time of flight for the Neon fragments shows two distinct peaks separated by ≈175ns. The mean arrival time of the fragments at the detector was ≈5940ns.

Similar to the Ne_2^+ measurements the background was determined from neutral fragments with a time of flight of 4900ns $\leq t_{tof} \leq$ 5750ns (see Fig. 5.4) shifted by ≈619ns to match the time of flight of the signal plus background events.

Fig. 5.16 shows the 2-dimensional positions of the signal Ne^0 fragments emerging from the overlap region having a time of flight of 5.8μs $\leq t_{tof} \leq$ 6.1μs. The green mark in Fig. 5.16 indicates the direction of the laser polarization $\vec{\varepsilon}_L$ which is in this case parallel to the propagation direction of the ion beam and thus perpendicular to the detector plane.

The 3-dimensional representation of the experimental data is give in Fig. 5.17. Here the squared radial position R^2 of a neutral Ne^0 fragment on the imaging detector is plotted versus the time of flight t_{tof} of the fragment. Lines of constant kinetic energy release according to Eq. 5.4 are also drawn for illustrative purposes. Fig. 5.17 shows an accumulation of neutral Neon fragments fulfilling the expected conditions on the kinetic energy release of 1eV$\leq \Delta E \leq$2.3eV (see also Fig. 5.1). The distribution illustrates that the Ne^0 fragments are well separated in time of flight

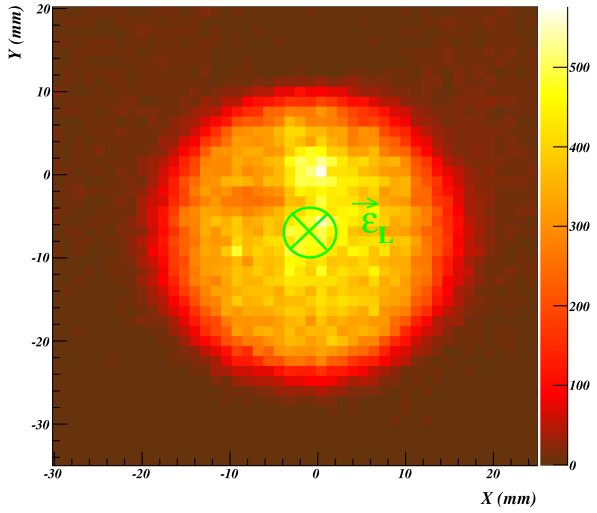

Figure 5.16: *2D detector image of the neutral Neon photofragments measured by the imaging detector. The green mark indicates the laser polarization which is perpendicular to the paper plane and thus parallel to the ion beam direction.*

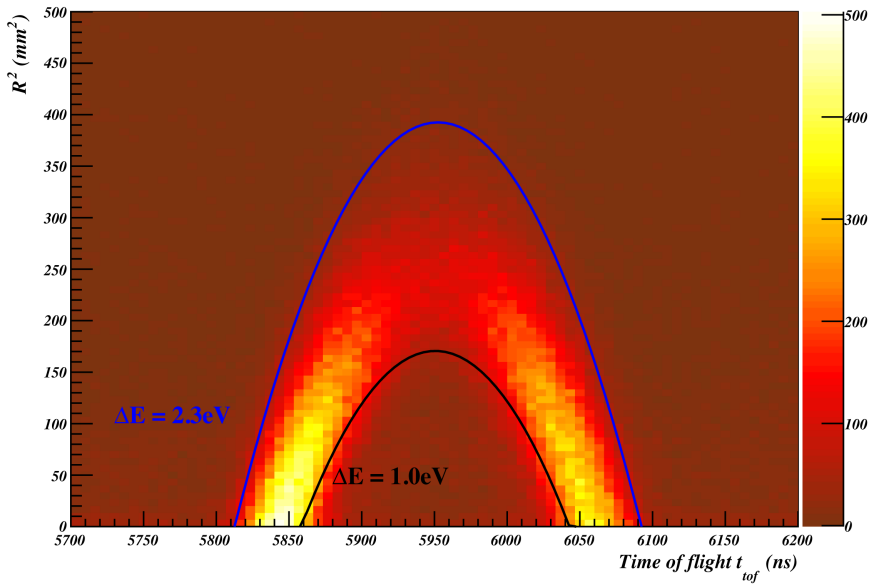

Figure 5.17: *R^2 versus time of flight t_{tof} distribution for Ne^0 fragments following photodissociation of Ne_2^+ ions at 532nm.*

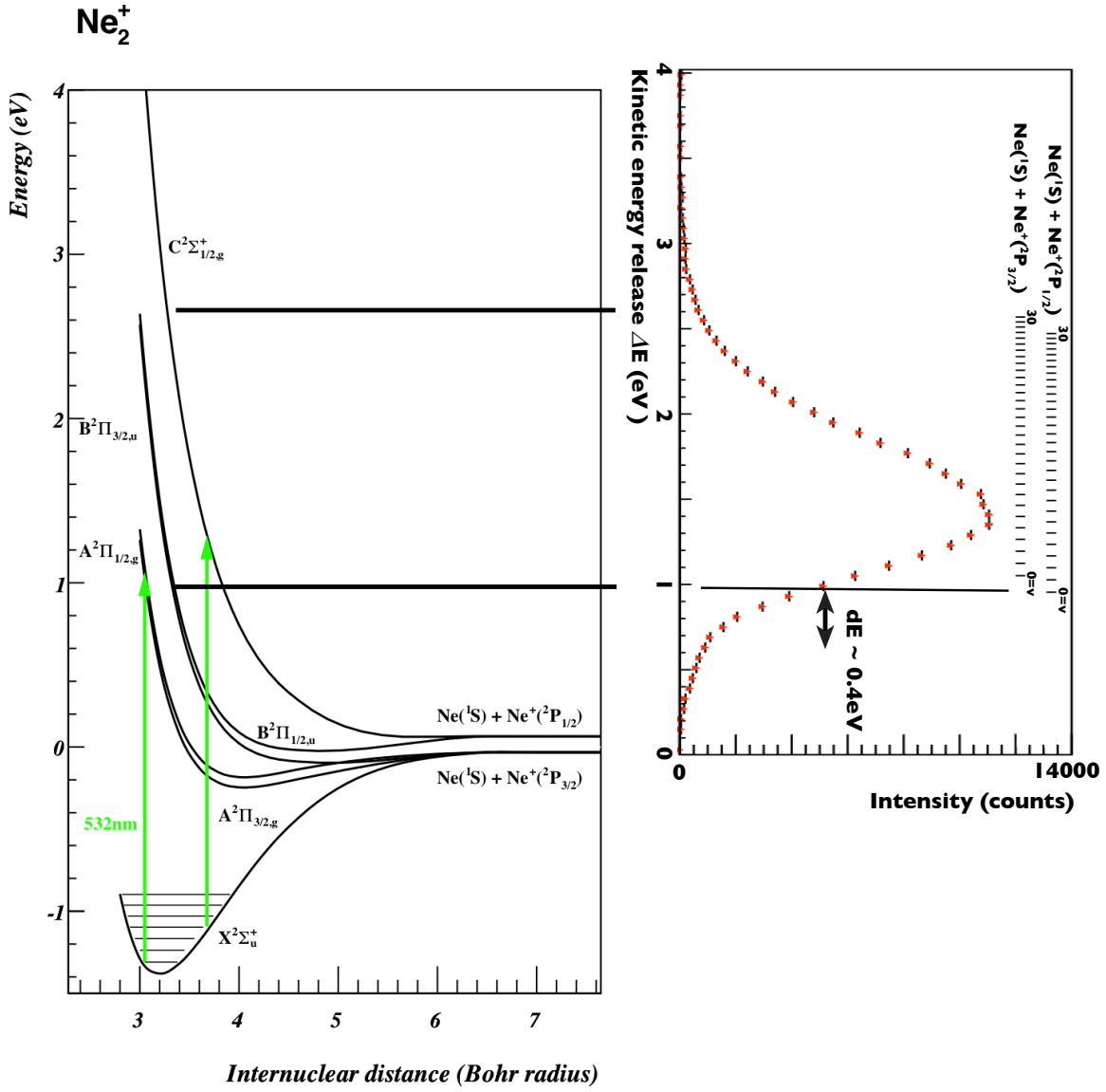

Figure 5.18: *Diagram of the dissociation of Ne_2^+ and the measured kinetic energy release of the neutral Neon photofragments.*

but have only low R^2 values.

5.4.3 Kinetic energy release and angular distributions

From the R^2 values and the time of flight of the Neon fragments the kinetic energy release ΔE (see Eq. 2.30) was derived. In addition to the spectrum of the signal events a kinetic energy distribution of the neutral background was also obtained and subtracted from the signal distribution. The resulting kinetic energy release spectrum is displayed in Fig. 5.18. At energy release values between 0.5eV and 3.0eV the distribution for the photofragments shows a clear

peak.

The kinetic energy release is related to the initial internal excitation of the molecular ion as given by Eq. 2.18. Thus, high internal excitation will lead to a high kinetic energy release. At 532nm the photodissociation of Ne_2^+ can proceed either via the $A^2\Pi_g$ repulsive curve or the $C^2\Sigma_g^+$ state. The kinetic energy release values corresponding to the two possible final channels for different vibrational levels of the ground state were calculated using the spectroscopic constants given in [66] and the experimentally determined value for the dissociation energy published in [19], and are displayed in Fig. 5.18. The experimentally observed kinetic energy release is consistent with a dissociation process via the $A^2\Pi_g$ and the $C^2\Sigma_g^+$ repulsive curves. Similar to the results obtained from the Ar_2^+ measurements, high vibrational excitation of the Ne_2^+ ions prior to dissociation is found to be present, leading to the extension of the spectrum to $\Delta E \approx 3eV$. With the same position resolution as in Ar_2^+ ($\pm 0.1mm$) and the same length of the laser pulse (9ns), the uncertainty of the energy measurement is slightly better, having a value of 0.4eV. The vibrational spacing of the Ne_2^+ ions is larger than for Ar_2^+ (e.g. the difference between $\nu = 0$ to $\nu = 1$ equals to 73meV) but the splitting of the final states due to spin-orbit effects is smaller with only 97meV. However, due to the energy resolution it is not expected that these features should be resolved. Furthermore, the observed extension of the spectrum to low kinetic energy energy release values observed in Fig. 5.18 can be attributed to the energy resolution.

The angular distributions of the photofragments were calculated using Eq. 2.29. Since the direction of polarization of the laser coincides with the ion beam propagation direction the angles θ_z and θ_L are the same. The distributions were again symmetrized by randomly assigning the sign to the argument of arctan in Eq. 2.29. The background angular distributions were obtained in the same manner and the results were subtracted from the signal distributions. The spectra are plotted in Fig. 5.19 for different ranges of the kinetic energy release.

The angular distributions for different regions of ΔE are clearly different from one another: for different values of the kinetic energy release the ratio between the height of the valley between the two peaks of the distribution and the maxima of the distribution changes.

In order to characterize the angular distributions, fits were conducted for pure perpendicular and parallel transitions assuming the same form as the first model in Ar_2^+ (see Eq. 5.5). Again a_{-1} and a_2 were free parameters in the fits. The obtained results are illustrated by the black curve in Fig. 5.19 while individual contributions for both symmetries are drawn for $\beta = -1$ (red curve) and for $\beta = 2$ (brown curve).

The amplitude of each contribution versus the kinetic energy release is depicted in Fig. 5.20 while Fig. 5.21 shows the ratio between the $\beta = -1$ and the $\beta = 2$ contribution. For the ratio of the two different symmetries one finds a clear dependence on the energy released in the dissociation process.

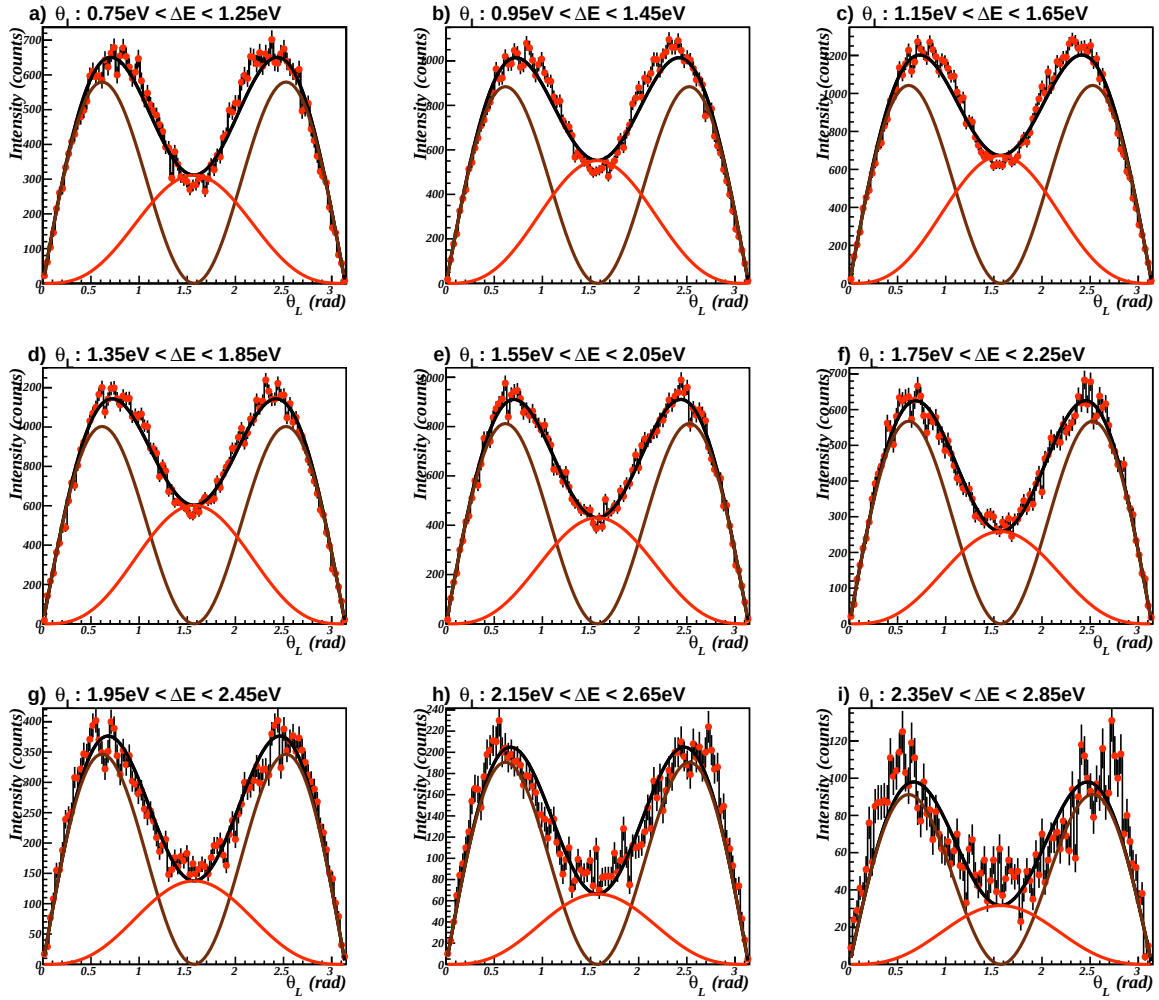

Figure 5.19: *Angular distribution of Ne^0 photofragments with the background subtracted for different cuts on the kinetic energy release. The black curve illustrates a fit using the model described by Eq. 5.5 while the brown curve shows the contribution of $\beta = 2$ and the red curve corresponds to the $\beta = -1$ contribution.*

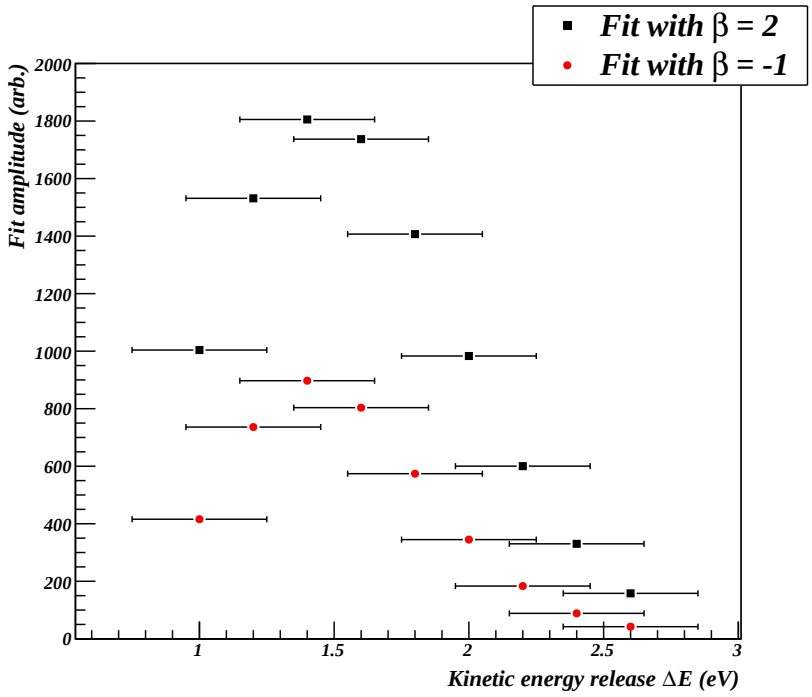

Figure 5.20: *Results for the fits conducted in Fig. 5.19, versus kinetic energy release ΔE.*

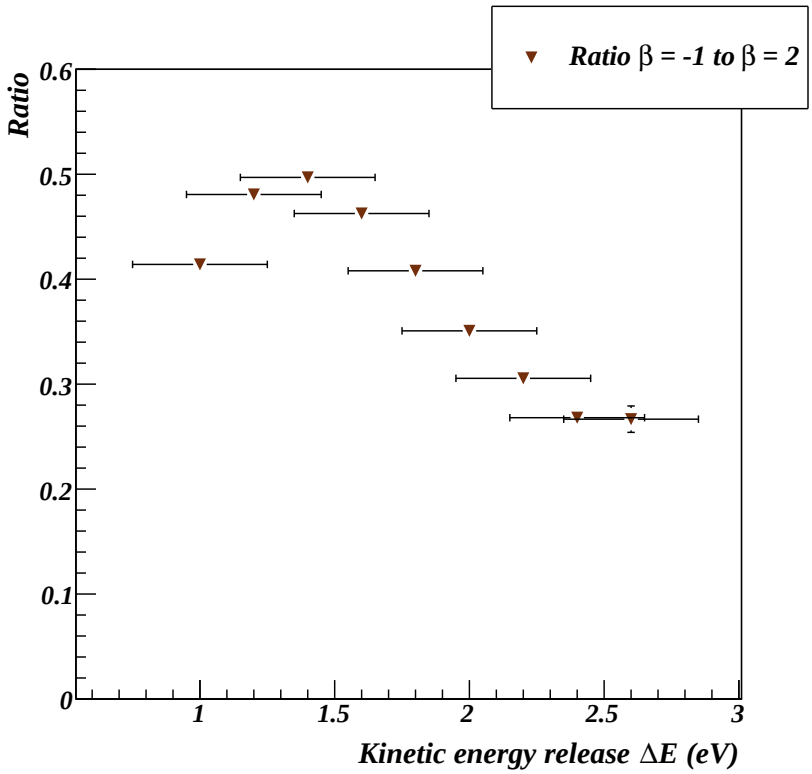

Figure 5.21: *Ratio of the $\beta = -1$ contribution to the $\beta = 2$ contribution versus kinetic energy release ΔE obtained from the fits in Fig. 5.19.*

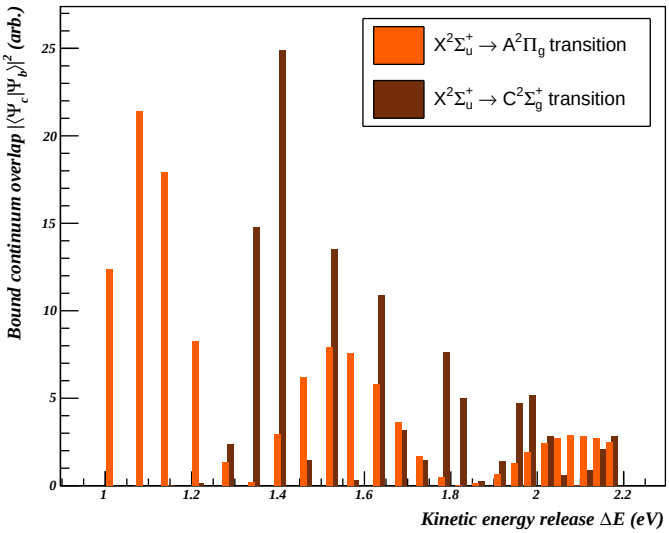

Figure 5.22: *Calculations of the Franck-Condon factors for the transitions from individual vibrational wavefunctions of the ground state to the continuum wavefunctions of the $A^2\Pi_g$ and $C^2\Sigma_u^+$ state. The values for the $A^2\Pi_g$ overlap factors have been shifted by -0.01eV for better visualization.*

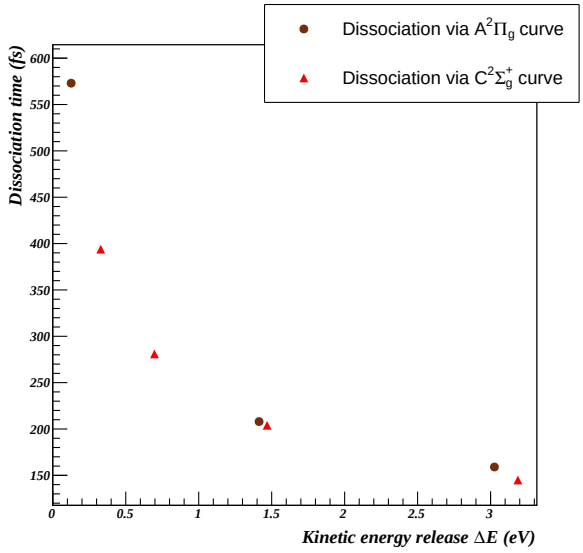

Figure 5.23: *Estimated dissociation time for the two repulsive states in the Ne_2^+ system versus kinetic energy release ΔE.*

5.4.4 Discussion

In Ne_2^+ photodissociation with 532nm photons dipole-allowed transitions are possible from the $X^2\Sigma_u^+$ ground state to the $A^2\Pi_g$ states and from the ground state to the $C^2\Sigma_g^+$ repulsive state. To compare the relative strength of each transition Franck-Condon factor calculations were carried out for the overlap of the bound and continuum wavefunctions [80] using the potential energy curves published by [19]. The calculated factors for individual vibrational levels of the bound state versus the kinetic energy release are shown in Fig. 5.22. The results show that the $X^2\Sigma_u^+ \rightarrow A^2\Pi_g$ transition is expected to dominate for a value of the kinetic energy release lower than 1.25eV. In addition, $X^2\Sigma_u^+ \rightarrow A^2\Sigma_g^+$ transitions should be observable for higher ΔE.

Transitions to the $A^2\Pi_g$ states should have perpendicular character while transitions to the $C^2\Sigma_g^+$ state should have parallel character. Judging by the calculated overlap factors shown in Fig. 5.22 the contribution from the $X^2\Sigma_u^+ \rightarrow C^2\Sigma_g^+$ transitions can be ruled out for values of the kinetic energy release below 1.25eV. Thus, only $X^2\Sigma_u^+ \rightarrow A^2\Pi_g$ should be observable. However, the angular distribution for the kinetic energy region $0.75 \leq \Delta E \leq 1.25$eV (see Fig. 5.19 a)) exhibits a predominantly parallel character with a small perpendicular contribution.

To evaluate the effect of rotation on the dissociation process the dissociation times were calculated. The time it takes for the molecule to dissociate was simulated using the same approach as for the Ar_2^+ dissociation (see Ch. 5.3.4). The molecular ion was assumed to be dissociated when the internuclear distance was larger than 8 Bohr radii. Dissociation times were calculated for fragmentation via the $C^2\Sigma_g^+$ state and via the $A^2\Pi_g$ states. The results are plotted versus the energy released in the dissociation process and are displayed in Fig. 5.23. For dissociation via the $C^2\Sigma_g^+$ excited state dissociation times vary between 130-400fs while the time it takes for the Ne_2^+ to separate via the $A^2\Pi_g$ curve can take slightly longer namely, 160-570fs. In case

of the Ne_2^+ ion the rotational constant is calculated in [66] with a value of B = 70μeV. This yields an estimated time of rotation for the molecule ranging from 200ps for J = 1 down to for instance 13ps for J = 20, assuming that the distance between the two atoms remains constant. In comparison to the dissociation times these values are larger by orders of magnitude and thus the effect of rotation on the angular distributions can be said to be negligible.
Due to spin-orbit effects, as discussed in Ch. 5.1, the $A^2\Pi_g$ states are in fact split into a $A^2\Pi_{\frac{1}{2},g}$ state and a $A^2\Pi_{\frac{3}{2},g}$ state which can be written as a linear combination of $|^2\Pi_g\rangle$ and $|^2\Sigma_g\rangle$ according to Eq. 5.3. Transitions from the ground state to the $A^2\Pi_{\frac{3}{2},g}$ should be dominantly perpendicular in nature while transitions to the $A^2\Pi_{\frac{1}{2},g}$ should exhibit both perpendicular and parallel character. Thus, it seems evident that the parallel character observed in the angular distribution for ΔE $\leq$1.25eV (Fig. 5.19 a)) results from the mixing of $|^2\Sigma_g\rangle$ into the $A^2\Pi_{\frac{1}{2},g}$.
This effect is consistent with the experimental observations of Moseley et al. [74] and the calculations preformed by Stevens et al. [101] in the case of the Argon dimer ion. In their calculations on the cross sections for the $X^2\Sigma_u^+ \rightarrow A^2\Pi_{\frac{1}{2},g}$ transition and $X^2\Sigma_u^+ \rightarrow A^2\Pi_{\frac{3}{2},g}$ transition Stevens and co workers find that the cross section increases by a factor of six due to the fact that the transition moments caused by spin-orbit effects ($\langle^2\Sigma_u^+|\mu_0|^2\Sigma_g^+\rangle$ and $\langle^2\Pi_u|\mu_0|^2\Pi_g\rangle$ see also Eq. 5.12) dominate the dissociation process.
At higher vibrational levels of the ground state, i.e. higher kinetic energy release values, the situation gets more complex, because in addition to transitions to the $A^2\Pi_{\frac{1}{2},g}$ and $A^2\Pi_{\frac{3}{2},g}$ state, the $C^2\Sigma_{\frac{1}{2},g}^+$ state becomes accessible (compare Fig. 5.22). This should give more parallel character to the angular distributions for values of the kinetic energy release higher than 1.25eV, while the perpendicular contribution should become smaller. However, the ratio between $\beta = -1$ and $\beta = 2$ (see Fig. 5.21) shows an even stronger perpendicular contribution which peaks at around ΔE = 1.4eV and than drops of for higher values of ΔE. The fact that the perpendicular contribution remains high throughout the observed kinetic energy regime, even though the transition to the $C^2\Sigma_{\frac{1}{2},g}^+$ should dominate according to the calculated Franck-Condon factors (Fig. 5.22), points to a similar effect as observed in the Ar_2^+ photodissociation experiments (Ch. 5.3). In the Ar_2^+ experiments the photodissociation was found to proceed via the $C^2\Sigma_{\frac{1}{2},g}^+$ repulsive state also here high $\beta = -1$ contributions were observed in the angular distributions of the photofragments for large kinetic energy release.

6. Free electron laser experiments

6.1 Significance of the HeH^+ ion

There has been extensive theoretical and experimental interest in HeH^+ partly because it is the simplest heteronuclear ion. The existence of a permanent dipole moment in the HeH^+ ion has permitted the acquisition of highly precise vibration-rotational and pure rotational transition energies from gas phase spectra. The first high resolution spectrum was obtained by Tolliver and co workers [103] using Doppler tuned ion beam spectroscopy. Bernath and Amano [10] determined accurate vibration-rotation constants of HeH^+ while the measurements were extended to the isotopomers by Crofton et al. [23] in 1989. More recently very precise studies of pure rotational transitions were obtained by [63] and measurements of pure rotational transitions up to the dissociation threshold were reported by [59].
The need for increasingly accurate ab inito calculations of HeH^+ was stimulated by these aforementioned high resolution measurements. The $X^1\Sigma^+$ ground state of HeH^+ is well established by first calculations published by Kołos and Peek [51] in 1976 (see Fig. 6.1) and by adiabatic corrections calculated by Bishop et al. [12]. The first excited state of HeH^+, namely $A^1\Sigma^+$, correlates with the $H(1^1S) + He^+(1^2S)$ limit, which is situated approximately 11eV [22] above the ground state limit of $H^+ + He(1^1S)$. Hence, the ground state is essentially isolated. Electronically excited states of HeH^+ are only reached from the ground state by high energy ($\geq$ 20eV) input. They have been theoretically extensively characterized by [36, 34, 35, 96, 8, 94], including their photodissociation [96, 8, 94]. Potential energy surfaces were taken from [82] and are displayed in Fig. 5.1.
Moreover, HeH^+ is composed of the two most abundant elements in the universe, and thus there is much astrophysical interest in the possibility that HeH^+ is an important species in interstellar space. HeH^+ is assumed to exists, although not definitively confirmed [68], in astrophysical plasmas [90] and is of importance in the chemistry of planetary nebulae [13].
Besides the fundamental interest in HeH^+ it also attracts attention as the isotopologue of $^3HeT^+$ which is formed in the T_2 beta decay given by

$$T_2 \rightarrow {}^3HeT^+(f) + e^- + \bar{\nu}_e, \tag{6.1}$$

where f designates a molecular final state of the daughter ion. By studying the shape of the

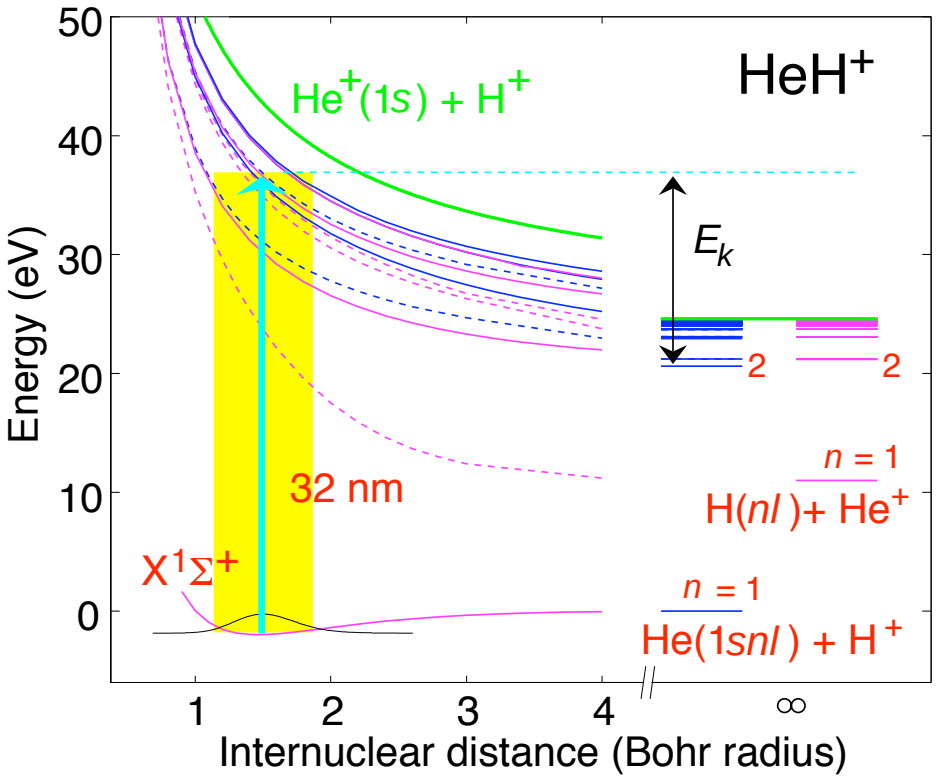

Figure 6.1: *HeH^+ potential energy surfaces, atomic final states and sample kinetic energy release for photodissociation of HeH^+ using VUV photons at 32nm [82]. The lowest vibrational wave function and the Franck-Condon region for high vibrational excitation are shown schematically for the $X^1\Sigma^+$ ground state [51] with excited $^1\Sigma^+$ [48] (dashed) and $^1\Pi$ (full lines) [36, 34, 35]. The green line traces the $He^+ + H^+$ Coulomb potential.*

β electron energy spectrum near the end-point energy it is possible to deduce the mass of the neutrino m_ν. However, the accuracy of these experiments [60, 15] is limited by the molecular final state distribution used in the analysis of the experimental data [94, 48]. This distribution is so far only available from theory, for example calculations were published by [50, 46] with more recent refinements presented in [48, 95] and references therein. In this framework it has been suggested [94] that the experimental investigation of the photoabsorption spectrum of the HeH^+ ion could serve as a good check of the accuracy of the calculated molecular final state distributions. Thus, calculated photodissociation cross sections for the HeH^+ ion were presented in [94].

6.2 Timing requirements

The time structure of the pulse train delivered by the free-electron laser is fairly complex. The overall repetition rate used in the FEL experiments was 5Hz. Every FEL light pulse is subdivided into several micro pulses. The amount of these micro pulses can be varied between one to several hundred, with a variable spacing of 1μs to 10μs between the micro pulses. For the HeH^+ experiments conducted at the free-electron laser the used settings were five micro pulses with a 10μs division (see Fig. 6.3).

Fig. 6.2 illustrates the timing scheme used in the FEL experiments. The timing signals triggering the different sub-branches, namely TIFF ion trigger, TIFF RoentDek start, TIFF PC scope start, TIFF ADC trigger and TIFF gate trigger, are delivered by the FEL through VME based timer cards. The TIFF timer channels are fixed in time with respect to the emission of the FEL pulse train.

For illustrative purposes all the relevant pulse trains produced are depicted in Fig. 6.3. The FEL pulse train consisting of five photon pulses with a division of 10μs is emitted every 200ms. Each FEL micro pulse is matched with an ion bunch. The TIFF ion trigger signal starts the generation of a pulse train of five ion bunches with a width of $\approx 2.0\mu$s and the same frequency as the FEL micro pulses. TIFF RoentDek start, TIFF PC scope start and TIFF ADC trigger supply the start signals of the TDC, the PC scope trigger and the ADC trigger respectively. TIFF gate trigger activates the generation of a second pulse train used to gate the imaging detector.

To conduct a background measurement between each FEL pulse train all channels, except for the ADC trigger, are equipped with a pseudo trigger (see Fig. 6.2). The pseudo trigger effectively delays the incoming FEL timing signals by 100ms and triggers the same sub-branch through an OR unit effectively doubling the repetition rate of the experiment to 10Hz. Hence, every second ion bunch train coincides with a FEL pulse train while every other ion bunch train is used as a background measurement.

The pulse train generation is explained in the insert of Fig. 6.2. The incoming start pulse

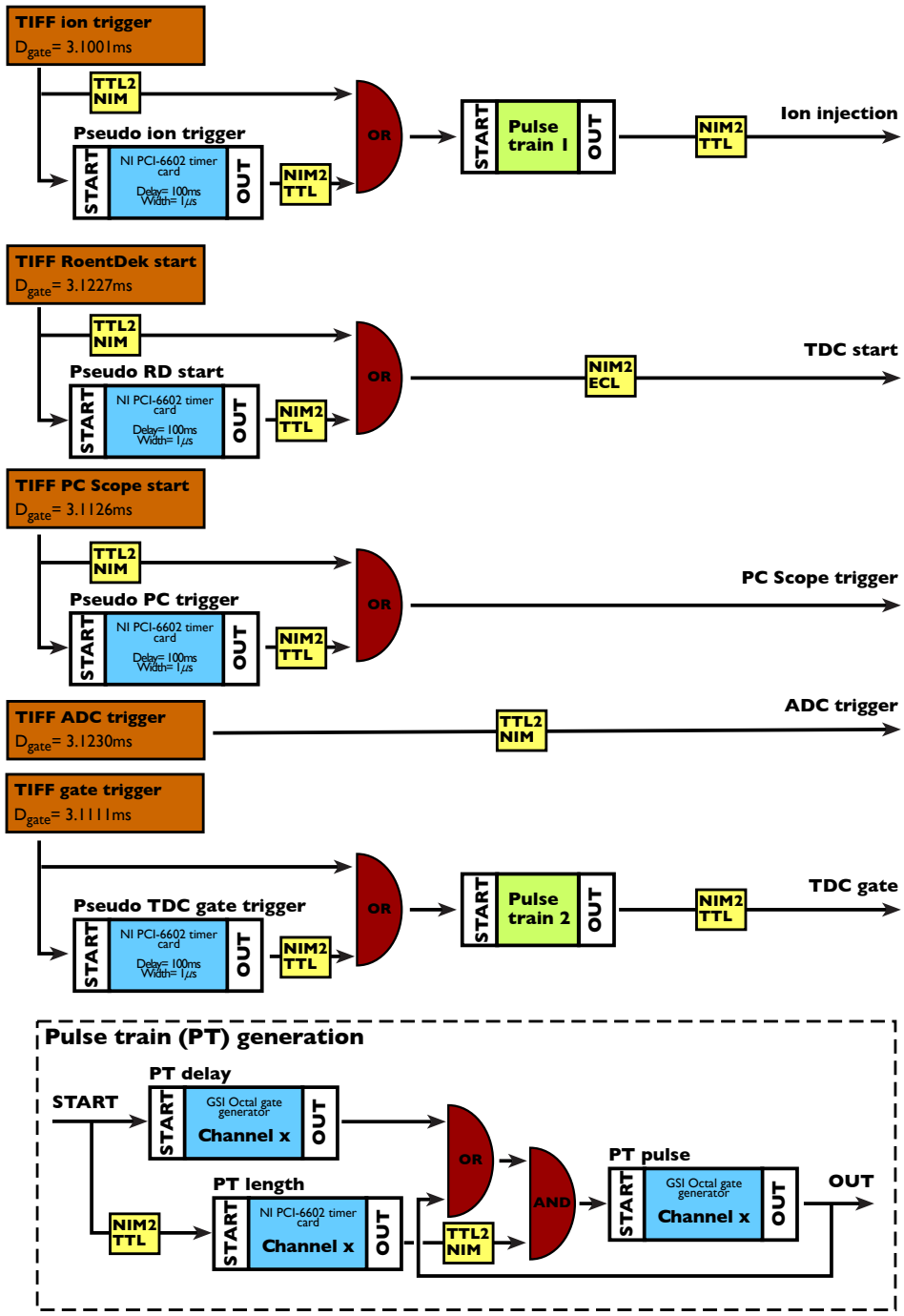

Figure 6.2: *Schematic diagram of the timing of the experimental setup used in the FEL experiments.*

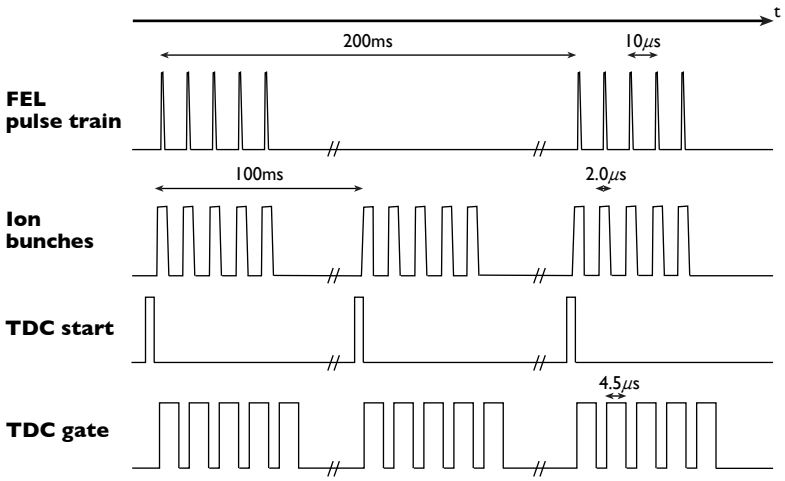

Figure 6.3: *FEL pulse train and corresponding pulse trains for the ion bunches and detector signals resulting from the timing scheme illustrated in Fig. 6.2.*

activates two timers. The upper timer (PT delay) controls the initial delay of the pulse train and triggers the PT pulse timer via an OR and an AND unit. The PT pulse timer controls the spacing and width of each individual pulse in the train. The output of PT pulse is fed to the outside, but is also used to trigger itself through the OR unit. The PT length timer only allows the PT pulse timer to trigger itself if a NIM signal is present at the AND unit. Hence, PT length defines the overall length of the pulse train.
The data acquisition system comprises the PC scope, CAMAC TDC module and CAMAC ADC module (see also Ch. 4.1.1). The PC scope records the analog signals originating from the photon beam dump and the ion bunch signals from the online beam monitor (see Fig. 3.15 a) and Ch. 3.5.3). In the resulting analog spectrum the peak heights of the ion and the photon bunches are measured. The obtained values are sent to the DAQ program and are recorded for every event.
The CAMAC TDC unit is triggered by the TDC start signal and then acquires the timing signals from the imaging detector for the full range of 65μs. Up to 16 hits per TDC channel were recorded. To blend out background events between the laser shots the TDC was gated by the TDC gate signal. The detector gate only allows the detector timing signals T_{x1}, T_{x2}, T_{y3} and T_{y4} (see Ch. 3.6) to be recorded by the TDC if the gate signal is high. The gate is positioned so that starting with the laser shot all neutral particles events are accepted for $\approx 4.5\mu$s.
Furthermore, the ADC was used to record an analog signal proportional to the average FEL pulse train intensity provided by the gas monitor detector (GMD) [89, 104] of the FEL.

6.3 HeH^+ photodissociation using VUV photons at 32nm

In the photodissociation experiments conducted at the free-electron laser in Hamburg the first system studied was HeH^+ ion. The data displayed in this section was taken in a total of 13 hours of measurement time. The experimental results are also subject of an article published by Pedersen et al. [82].
VUV photon pulses produced by FLASH at 32nm wavelength were crossed with a HeH^+ beam at a 90° angle. The photon polarization was directed parallel to the propagation direction of the ion beam. The FEL pulse train consisted of several short (≈30fs in length) micro pulses of which a number of 5 were matched with an equal number of ion bunches. With an FEL repetition rate of 5Hz this yielded an effective interaction rate of 25Hz. The ion beam intensity at the interaction point was typically 2-3nA of HeH^+ with a pulse length ranging from 2-4.5μs. The average energy per micro pulse was 20-30μJ. The photons were directed across the plane grating monochromator (see Ch. 3.7.2 for more details) which was set to the zeroth order, resulting in an approximate transmission of 30-50% and a laser bandwidth of ±0.5nm. Both beams were focussed to a comparable beam diameter of 1-2mm. Hence, on average ≈25 HeH^+ ions collided with $2 \cdot 10^{12}$ photons.

After passing through the interaction region the photon beam was collected on the photon beam dump (see Ch. 3.5.3). The signal obtained from the beam dump was calibrated relative to the gas monitor detector giving the absolute photon number per pulse.

Neutral fragments produced in photodissociation reactions are recorded by the imaging detector 3.6.2 which is situated about 1m downstream oriented perpendicular to the ion beam axis. The region around the overlap of the two beams was biased to a negative potential of 1500-3000V using the device described in Ch. 3.5.3 and depicted in Fig. 3.15 b). Hence, neutral fragments emerging from the interaction point had a higher kinetic energy than neutrals formed in other sections of the beam pipe, e.g. by dissociative collisions of the ions with the residual gas ($\approx 5 \cdot 10^{-10}$mbar). He^0 fragments released from the ion bunch in the biased region arrived at the imaging detector ≈350-600ns earlier than fragments produced in other sections of the beam pipe facing the detector. By adjusting the temporal overlap of both beams so that the photons coincide with the ions after ≈100ns with respect to the edge of the ion bunch the photofragment signal could be observed at a time when only neutrals produced in the small biased region contribute to the background.

In addition to the neutral background a background of stray photons was observed promptly after the FEL pulse on the imaging detector. This photonic background could be sufficiently reduced by correctly aligning the FEL beam in the interaction region.

The remaining ion beam is removed from the beam pipe after leaving the interaction region via the vertical deflection plates mounted on the interaction feedthrough (see Fig. 3.15 b)). The beam is deflected onto the beam monitoring plate. The resulting analog signal indicating the ion bunch intensities was recorded using the PC scope.

The imaging detector records the time of flight t_{tof} and position of each neutral fragment for the full length of the photon and ion pulse train. Thus, the resulting spectrum has to be deconvoluted to obtain the correct time of flight for each particle. Therefore the time of each laser shot was determined by getting the peak position of the signal produced by the stray photons. The five distinct slices of the spectrum were then overlayed so that the photon signal positions coincided and the contained counts were summed up.

For each setting of the bias potential the precise fragment energy was determined by the average time of flight of the photon induced signal events. The runs with different settings were added by scaling each event to the nominal value of 7200eV (given by E_{ion} = 4200eV plus the additional acceleration due to the bias potential), thereby keeping the longitudinal velocity $v_{||} = \frac{L - v_{ion} t_{tof}}{t_{tof}}$ and the transverse velocity $v_{\perp} = \frac{R}{t_{tof}}$ of each event constant (here L corresponds to a value of 0.987m).

Fig. 6.4 shows the resulting 3-dimensional distribution of the neutral fragments. Here the radial position of each fragment on the detector given by $R = \sqrt{X^2 + Y^2}$ is plotted versus the time of flight t_{tof}. In comparison to the background measurement (left) the image representing the data taken with both FEL and ion beam present clearly shows an amassment of He fragments with

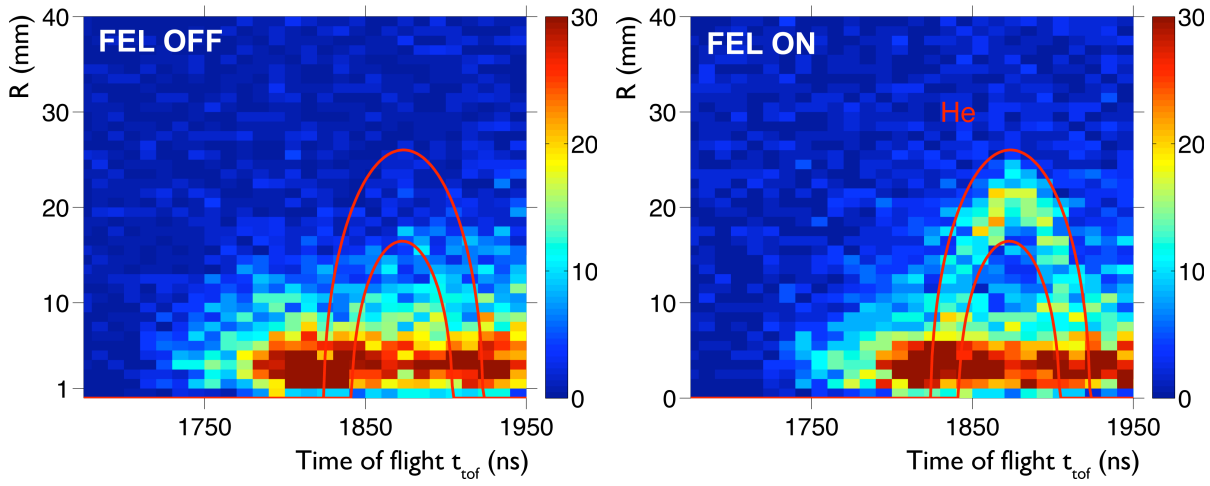

Figure 6.4: *Radial position* $\mathrm{R} = \sqrt{\mathrm{X}^2 + \mathrm{Y}^2}$ *versus the event time of flight* t_{tof} *for* HeH^+ *photodissociation at 32nm.*

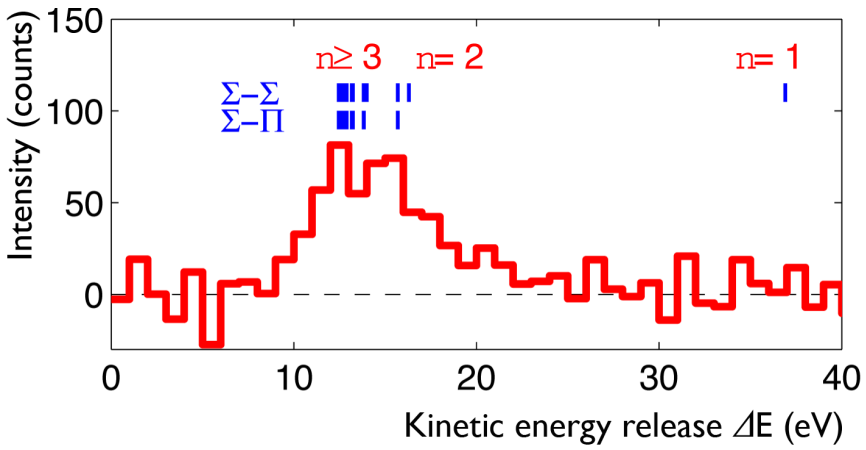

Figure 6.5: *HeH^+ kinetic energy release spectrum after subtraction of the background energy release.*

large transverse momentum fulfilling the condition of high kinetic energy release. The red curves indicate lines of kinetic energy release equal to 8eV and 20eV respectively which correspond to the expected ΔE values taken from Fig. 6.1.

Neutral Hydrogen fragments are expected to emerge at similar kinetic energy values. However, the anticipated center of mass velocities of the H^0 fragments are larger by a factor of four, due to the smaller mass. The resulting radial position of the fragments on the imaging detector also increases by the same factor and thus only a small portion of the solid angle of these fragments is covered by the current detector arrangement.

With the radial position and time of flight of each fragment one can determine the corresponding kinetic energy release of the fragment using Eq. 2.30. The distribution of kinetic energy release of the fragments after subtraction of the background is displayed in Fig. 6.5. The kinetic energy release is related to the initial excitation of the ions and the final excitation of the photofragments as described in Eq. 2.18. Thus, a low kinetic energy release corresponds to a highly excited final states of the He atoms. The energy release distribution shows a significant contribution of highly excited ($n \geq 3$) He^0 fragments totaling to about 50% with the remaining contribution going into the n = 2 final state.

The low energy edge of the spectrum is consistent with the spectral width of the unmonochromatised photon beam of $\pm$0.5eV and the resolution of the detector which is determined by the time resolution of the TDC of 1ns which results in an energy resolution of $\pm$0.7eV. The extension of the energy release spectrum towards ΔE values of up to 21eV indicates the presence of high internal excitation of the HeH^+ ions prior to dissociation which was also found to be present in the experiments conducted on the rare gas dimer ions (see Ch. 5.3 and Ch. 5.4).

The absolute cross section for the reaction of HeH^+ ions with 32nm photons can be derived from the measured ion current I and photon number N_p for each pulse. Using the overlap

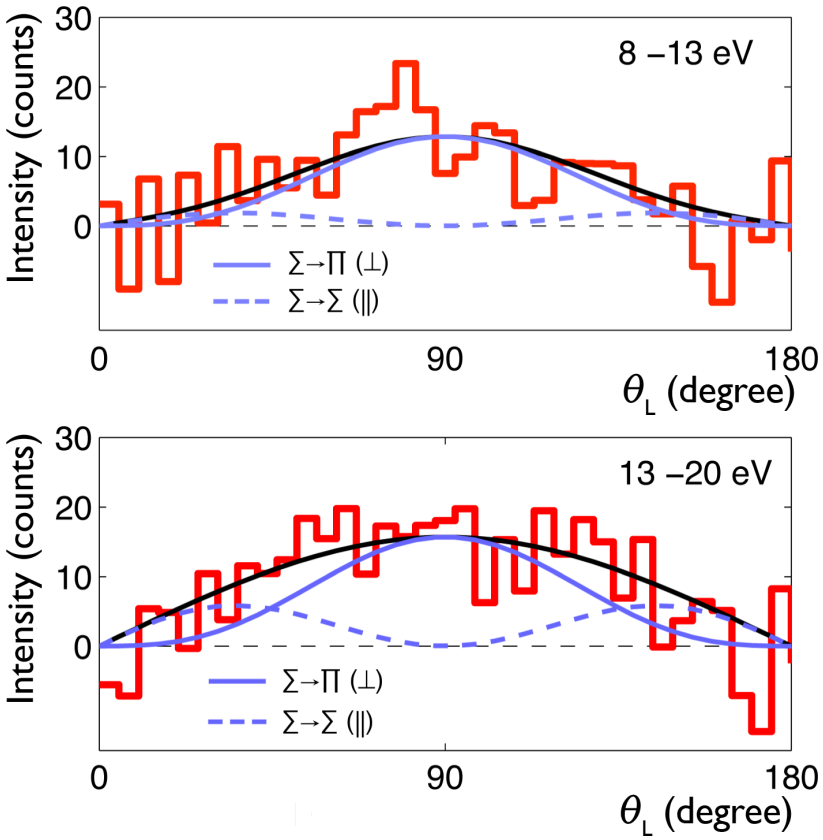

Figure 6.6: *Angular distribution of neutral He^0 fragments following photodissociation of HeH^+ for different regions of the kinetic energy release. The distributions obtained from the background measurements were subtracted in both plots.*

of ion and photon beam determined by scanning the 1mm slit across the interaction point as described in Ch. 4.4 the overlap factor can be derived to $\mathrm{F} = 3.5 \pm 1.0\mathrm{cm}^{-1}$. With the number of observed signal events N and an estimated detection efficiency of the micro channel plate used for fragment detection $\varepsilon = 0.5 \pm 0.1$ the cross section is given by $\sigma = \frac{\mathrm{N}}{\varepsilon \mathrm{F} \sum \mathrm{N}_p n_l}$, where $\sum$ denotes the sum over all temporal overlaps of ion and FEL beam and $n_l = \frac{I}{e \mathrm{v}_{ion}}$ is the linear ion density corresponding to the ion current I and the velocity of the ion v_{ion}. Thus, one arrives at an absolute cross section of $\sigma = (1.4 \pm 0.7) \cdot 10^{-18}\mathrm{cm}^2$.

Fig 6.6 shows the angular distribution of the photofragments. Here the angle comprised between the molecular axis of dissociation and the polarization direction of the laser beam is plotted versus the count rate for two cuts on the kinetic energy release corresponding to the n = 2 and the $n \geq 3$ final channel.

The angular distributions of He^0 fragments for both kinetic energy regimes show a clear dominance of excitations from the $X^1\Sigma^+$ ground state excited Π states resulting in a $\beta = -1$ character of the distribution with respective contributions of ≈90% for the low kinetic energy release and

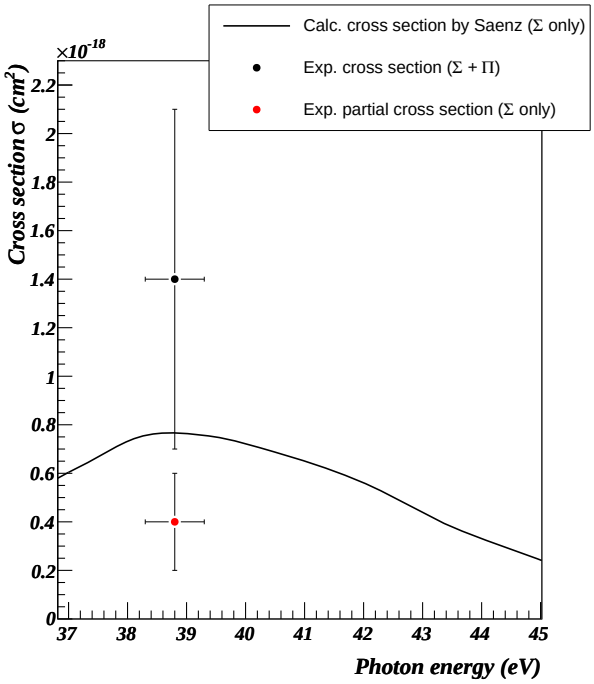

Figure 6.7: *Comparison of the calculated cross section published by [94] and the experimentally determined total and partial cross sections.*

≈70% for the high ΔE region.

6.3.1 Comparison to theoretical studies of the HeH^+ system

The observed photodissociation of HeH^+ at 32nm proceeds via a manifold of excited HeH^+ potential curves (see Fig. 6.1). So far only one theoretical study by Saenz and co workers [94] calculated the cross section of a large subset of these curves. They selected the twelve lowest $^1\Sigma^+$ states correlated to the $He^+(1s) + H(nl)$ and the $He(1snl) + H^+$ final states, arriving at a value of $0.8 \cdot 10^{-18}cm^2$ for the cross section at 32nm for the vibrational ground state of HeH^+. From the angular distributions one arrives at a contribution of the $\Sigma \rightarrow \Sigma$ transition of ≈10% and ≈30% respectively. Taking the 30% of the estimated contribution one obtains a measured partial cross section of $(0.4 \pm 0.2) \cdot 10^{-18}cm^2$ for the $He(1snl) + H^+$ final channel and an unknown vibrational excitation. The calculated cross section and the experimentally determined values for the total cross section (Σ and Π) and the partial cross section (Σ only) are plotted in Fig. 6.7. If one assumes that the magnitude of the cross section is similar for both final states and for the various vibrational levels the calculated value is in reasonable agreement with the measurement.

However, the kinetic energy release distribution (see Fig. 6.5) of the He^0 fragments shows that even for the low vibrational states highly excited He atoms ($n \leq 3$) are observed indicating that even higher excited molecular states than considered in [94] play a role in the dissociation process.

Furthermore, the angular distributions shows that the major contribution to the cross section

arises due to $\Sigma \rightarrow \Pi$ transitions. These states have been neglected in the recent calculations because the population of the $^1\Pi$ states in $T_2\beta$ decay is only a higher order effect [94]. The study performed by Basu et al. [8] took into account the lowest lying $C^1\Pi$ state and calculated partial dissociation cross sections showing that the contribution from both symmetries is about equal. This tendency is more or less confirmed by the experimental results.
From the experimental data it becomes clear that for theoretical predictions of the total photodissociation cross section of HeH^+ higher excited potential curves of both Σ and Π symmetry need to be included in the calculations. Also for a full theoretical understanding of the photodissociation of the HeH^+ system at VUV photon energies, which is of importance in astrochemistry and the associated chemical models, these high lying potential surfaces cannot be ignored.

7. Summary and outlook

7.1 Summarized results and conclusions

In this work a novel apparatus to study photodissociation of molecular ions has been introduced. The Trapped Ion Fragmentation experiment at FLASH was designed and setup at the Max-Planck-Institut für Kernphysik in Heidelberg. Advanced ion beam pulsing and trapping schemes as well as photodissociation imaging on molecular ion beams using optical lasers was explored in test experiments. At a later stage the setup was installed at the plane grating monochromator beamline of the new free-electron laser at DESY. The experimental setup combines fast ion beam imaging of photofragments with an electrostatic ion trap which allows trapping of the ions prior to dissociation experiments.

The molecular ions are produced using a hollow cathode ion source suitable for production of a wide variety of molecular ions. The molecular ions are accelerated to energies of a few keV upon leaving the ion source. The desired ion species is mass selected in a 90° dipole magnet and transferred to the ion trap. The primary purpose of the ion beam trap is to store the ions for a prolonged time to allow them to relax to the vibrational ground state.

After being extracted from the trap the ion bunches are crossed at a 90° angle with the photon pulses either coming from the free-electron laser or from a pulsed Nd:YAG laser system. Neutral and charged fragments resulting from photodissociation reactions proceed to an MCP delay-line detector mounted straight ahead of the interaction point oriented perpendicular to the ion beam propagation direction. The imaging detector records the position of each fragment on the detector as well as the corresponding arrival time of the particle. With the recorded information the energy released in the photodissociation process and the angular distribution of the photofragments can be inferred.

The experimental setup was extensively characterized. The performance of the ion source was investigated using different settings and gas mixtures. Several mass spectra were obtained which illustrated that sufficient currents of the desired ion species, namely Ar^+, Ne_2^+ , Ar_2^+ , and HeH^+ could be obtained.

The ion trap operation was established. The obtained results for stable trapping conditions were found to be in good agreement with conducted computer simulations. Typical storage times of ions inside the trap were found to be on the order of several 100ms at a trap inside pressure

corresponding to $3 \cdot 10^{-9}$mbar.

Additionally a novel extraction and pulsing method was implemented and successfully tested. Tests conducted with this extraction scheme successfully demonstrated that short ion bunches of ≈500ns length could be produced. In combination with ions stored in the ion beam trap it could be illustrated, that multiple short ion bunches could be extracted from one filling of the ion beam trap.

Based on the availability of short ion pulses, a new diagnostic method to control the temporal and spatial overlap of ion and photon beam was devised. To determine the temporal overlap the arrival time of the ion pulse is recorded using a MCP detector while the photon beam timing signal is derived by collecting the beam on a copper plate which is mounted electrically isolated. The relative position of ion and photon beam at the interaction point is obtained by scanning a 1mm slit across the overlap region. The information on the spatial overlap of the two beams is used to determine the overlap function and to measure absolute cross sections of the photodissociation reactions.

Studies of photofragmentation of rare-gas dimer ions, namely the two systems Ar_2^+ and Ne_2^+, were performed using a pulsed Nd:YAG laser. The photodissociation experiments on Ar_2^+ were done using UV photons at 266nm. The kinetic energy release of the Ar^0 fragments recorded after fragmentation is consistent with a dissociation via the $C^2\Sigma^+_{\frac{1}{2},g}$ repulsive state. The measured angular distributions exhibit a striking deviation from the expected purely parallel character of the transition which increases for higher kinetic energy release values. An influence of rotation of the molecule on the angular distributions could be ruled out. Also a transition to the lower lying $A^2\Pi_g$ states was found to be negligible. Thus, the effect has to be caused by the mixing of states due to spin-orbit effects. The magnitude of these effects observed in the experimental data were compared to previous theoretical predictions. The experimental data was found to exhibit much stronger mixing effects than previously conceived.

In photodissociation reactions of the Neon dimer ion with photons at 532nm wavelength transitions are possible from the ground state to the $A^2\Pi_g$ states and the $C^2\Sigma_{\frac{1}{2},g}$ state. For the low kinetic energy release values only transitions to the $A^2\Pi_g$ states contribute to the photodissociation process. One finds in the angular distribution some contribution of perpendicular transitions but also a dominant contribution of parallel character which can be attributed to the mixing due to spin orbit interactions of the $A^2\Pi_{\frac{1}{2},g}$ state. At higher kinetic energy release values the situation gets more complicated because transitions to the $A^2\Pi_g$ states as well as the $C^2\Sigma^+_g$ state are equally possible. In the angular distributions the parallel transition still dominates the picture but the perpendicular contribution to the transition remains high indicating that transitions to the $C^2\Sigma^+_g$ in Ne_2^+ also exhibit a strong perpendicular character as observed in the case of Ar_2^+.

While in the Ar_2^+ and Ne_2^+ photodissociation experiments still relied on conventional lasers the dissociation of HeH^+ requires highly energetic photons to reach the highly excited repulsive po-

tential energy curves. With the 32nm photons available at the free-electron laser corresponding to a photon energy of 38.8eV a significant portion of these high-lying potential surfaces could be addressed. Photodissociation of HeH^+ ions using 32nm photons focussed on the detection of the neutral Helium fragments emerging from the overlap region. The resulting kinetic energy release spectrum of the He^0 fragments showed two distinct peaks. The lower energy release peak residing between $8eV \leq \Delta E \leq 13eV$ corresponds to highly excited neutral He(1snl) fragments with a contribution of ≈50% found in $n \geq 3$. The remaining half of the fragments contributed to the $n = 2$ final channel having a kinetic energy release ranging from 13eV to 20eV. The absolute cross section at this wavelength was measured to be $(1.4 \pm 0.7) \cdot 10^{-18}\text{cm}^2$. The determined angular distributions of the photofragments for both regions of the kinetic energy release showed a clear dominance of photodissociation perpendicular to the laser polarization was found in contrast to dissociation pathways so far addressed in theoretical studies. Taking into account the relative contributions observed in the angular distribution measurements yields a value for the partial cross section which is ≈50% lower than previously predicted by theory.

7.2 Outlook

Based on the presented results and recent technical development at the TIFF setup the above mentioned experimental results can be further improved in the near future.

All molecular ion species studied showed high vibrational excitation to be present prior to dissociation which made analysis of the data difficult. Thus, all experiments would benefit from cooling of the ions inside the ion beam trap. In the case of the homonuclear rare gas ions storage of these ions should not lead to a significant reduction of vibrational excitation because of the lack of a permanent dipole moment. Hence, a move to dimer ions which experience a permanent dipole moment, e.g. the $HeNe^+$ system, is planned. This system was tried previously but it turned out that insufficient current could be produced with the hollow cathode ion source. Therefore, a switch to a different ion source is necessary. First tests showed that high currents of the Helium Neon dimer ion could be produced using a duo-plasmatron ion source. Work on installation of this ion source at the TIFF setup is currently under way.

In the case of HeH^+ with typical relaxation times of ≈100ms cooling is possible. However, due to limitations in the initially available photon intensities at the FEL, storage of the ions would have lead to a significant reduction in ion beam intensity which would have made the current experiments impossible. With the anticipated further increase in pulse energies at the free-electron laser, photodissociation studies in combination with trapping of the ions would become feasible. Higher photon intensities would also lead to a further improvement in statistics for the HeH^+ experiments.

With the second imaging detector for light photofragments now installed at the TIFF setup the neutral Hydrogen channel in the HeH^+ photodissociation can also be observed. Furthermore, this

improvement will enhance the energy resolution of the detector system and through coincidence measurements the signal to background ratio can be further improved. Additionally, it opens up many new possibilities to study the fragmentation of systems consisting of more than two atoms since almost all photodissociation fragments of such a system can be recorded. A further step would also be the extension of the HeH^+ photodissociation measurements to different wavelength to probe the theoretical calculated cross section for different photon energies.

References

[1] SASE FEL at the TESLA Facility, Phase 2. TESLA-FEL Report 2002-01, Deutsches Elektronen-Synchrotron DESY, Notkestr. 85, 22607 Hamburg, June 2002.

[2] T. Åberg. A VUV Free Electron Laser at the TESLA Test Facility at DESY. TESLA-FEL Report 1995-03, Deutsches Elektronen-Synchrotron DESY, Notkestr. 85, 22607 Hamburg, 1995.

[3] A. C. Allison and A. Dalgarno. Photodissociation of vibrationally excited H_2, HD, and D_2 by absorption into the continua of the Lyman and Werner system. *Atomic Data*, 1:91–102, 1969.

[4] M. Altarelli, R. Brinkmann, M. Chergui, W. Decking, B. Dobson, S. Düsterer, G. Grübel, W. Graeff, H. Graafsma, J. Hajdu, J. Marangos, J. Pflüger, H. Redlin, D. Riley, I. Robinson, J. Rossbach, A. Schwarz, K. Tiedtke, T. Tschentscher, I. Vartaniants, H. Wabnitz, H. Weise, R. Wichmann, K. Witte, A. Wolf, M. Wulff, and M. Yurkov. The European X-Ray Free-Electron Laser Technical Design Report. Technical report, Deutsches Elektronen-Synchrotron DESY, Notkestr. 85, 22607 Hamburg, June 2006.

[5] S. M. Altevogt. Production of rotationally cold H_3^+ ions with a hollow cathode ion source. Diploma thesis, University of Heidelberg, July 2003.

[6] J. Andruszkow, B. Aune, V. Ayvazyan, N. Baboi, R. Bakker, V. Balakin, D. Barni, A. Bazhan, M. Bernard, A. Bosotti, J. C. Bourdon, W. Brefeld, R. Brinkmann, S. Buhler, J.-P. Carneiro, M. Castellano, P. Castro, L. Catani, S. Chel, Y. Cho, S. Choroba, E. R. Colby, W. Decking, P. Den Hartog, M. Desmons, M. Dohlus, and D. Edwards. First observation of self-amplified spontaneous emission in a free-electron laser at 109nm wavelength. *Phys. Rev. Lett.*, 85(18):3825–3829, October 2000.

[7] V. Ayvazyan, N. Baboi, J. Bähr, V. Balandin, B. Beutner, A. Brandt, I. Bohnet, A. Bolzmann, R. Brinkmann, O. I. Brovko, J. P. Carneiro, S. Casalbuoni, M. Castellano, P. Castro, L. Catani, E. Chiadroni, S. Choroba, A. Cianchi, H. Delsim-Hashemi, G. Di Pirro, M. Dohlus, S. Düsterer, H. T. Edwards, B. Faatz, A. A. Fateev, J. Feldhaus, K. Flöttmann, J. Frisch, L. Fröhlich, T. Garvey, U. Gensch, N. Golubeva, H.-J. Grabosch, B. Grigoryan,

O. Grimm, U. Hahn, J. H. Han, M. V. Hartrott, K. Honkavaara, M. Hüning, R. Ischebeck, E. Jaeschke, M. Jablonka, R. Kammering, V. Katalev, B. Keitel, S. Khodyachykh, Y. Kim, V. Kocharyan, M. Körfer, M. Kollewe, D. Kostin, D. Krämer, M. Krassilnikov, G. Kube, L. Lilje, T. Limberg, D. Lipka, F. Löhl, M. Luong, C. Magne, J. Menzel, P. Michelato, V. Miltchev, M. Minty, W. D. Möller, L. Monaco, W. Müller, M. Nagl, O. Napoly, P. Nicolosi, D. Nölle, T. Nuñez, A. Oppelt, C. Pagani, R. Paparella, B. Petersen, B. Petrosyan, J. Pflüger, P. Piot, E. Plönjes, L. Poletto, D. Proch, D. Pugachov, K. Rehlich, D. Richter, S. Riemann, M. Ross, J. Rossbach, M. Sachwitz, E. L. Saldin, W. Sandner, H. Schlarb, B. Schmidt, M. Schmitz, P. Schmüser, J. R. Schneider, E. A. Schneidmiller, H.-J. Schreiber, S. Schreiber, A. V. Shabunov, D. Sertore, S. Setzer, S. Simrock, E. Sombrowski, L. Staykov, B. Steffen, F. Stephan, F. Stulle, K. P. Sytchev, H. Thom, K. Tiedtke, M. Tischer, R. Treusch, D. Trines, I. Tsakov, A. Vardanyan, R. Wanzenberg, T. Weiland, H. Weise, M. Wendt, I. Will, A. Winter, K. Wittenburg, M. V. Yurkov, I. Zagorodnov, P. Zambolin, and K. Zapfe. First operation of a free-electron laser generating GW power radiation at 32nm wavelength. *The European Physical Journal D - Atomic, Molecular, Optical and Plasma Physics*, V37(2):297–303, 2006.

[8] D. Basu and A. K. Barua. Photodissociation of HeH^+ molecular ion. *J. Phys. B*, 17(8):1537–1545, 1984.

[9] D. R. Bates and L. Spitzer. The density of molecules in interstellar space. *Astrophys. J.*, 113(3):441–463, May 1951.

[10] P. Bernath and T. Amano. Detection of the infrared fundamental band of HeH^+. *Phys. Rev. Lett.*, 48(1):20–22, Jan 1982.

[11] R. A. Beyer and J. A. Vanderhoff. Cross section measurements for photodetachment or photodissociation of ions produced in gaseous mixtures of O_2, CO_2, and H_2O. *J. Chem. Phys.*, 65(6):2313–2321, 1976.

[12] D. M. Bishop and L. M. Cheung. A theoretical investigation of HeH^+. *J. Mol. Spectros.*, 75(3):462–473, 1979.

[13] J. H. Black. Molecules in planetary nebulae. *Astrophys. J.*, 222:125–131, May 1978.

[14] R. Bonifacio, C. Pellegrini, and L. M. Narducci. Collective instabilities and high-gain regime in a free electron laser. *Optics Communications*, 50(6):373–378, 1984.

[15] J. Bonn, B. Bornschein, L. Bornschein, L. Fickinger, B. Flatt, O. Kazachenko, A. Kovalik, Ch. Kraus, E. W. Otten, J. P. Schall, H. Ulrich, and Ch. Weinheimer. The Mainz neutrino mass experiment. *Nucl. Phys. B - Proc. Suppl.*, 91(1-3):273–279, 2001.

[16] M. Born and R. Oppenheimer. Zur Quantentheorie der Molekeln. *Ann. Phys.*, 84(4):457–484, 1927.

[17] B. H. Bransden and C. J. Joachain. *Physics of atoms and molecules.* Addison Wesley Longman Limited, 1997.

[18] R. Brinkmann, G. Materlik, J. Rossbach, J. R. Schneider, and B.-H. Wiik. An X-ray FEL laboratory as part of a linear collider design. *Nucl. Instr. Meth. Phys. Res. A*, 393(1-3):86–92, 1997.

[19] L. Broström, M. Larsson, S. Mannervik, R. T. Short, and D. Sonnek. Photodissociation of Ne_2^+. *J. Chem. Soc. Faraday Trans.*, 87:797–802, 1991.

[20] Continuum, 3150 Central Expressway, Santa Clara, CA 05051. *Operation and Maintenance Manual for the Continuum Powerlite 6000 Series Laser*, 1993.

[21] J. Cooper and R. N. Zare. Angular distribution of photoelectrons. *J. Chem. Phys.*, 48:942–943, 1968.

[22] J. A. Coxon and P. G. Hajigeorgiou. Experimental born-oppenheimer potential for the $X^1\sigma^+$ ground state of HeH^+: Comparison with the Ab *initio* Potential. *J. Mol. Spectros.*, 193(2):306–318, 1999.

[23] M. W. Crofton, R. S. Altman, N. N. Haese, and T. Oka. Infrared spectra of $^4HeH^+$, $^4HeD^+$, $^3HeH^+$, and $^4HeD^+$. *J. Chem. Phys.*, 91(10):5882–5886, 1989.

[24] M. Dahan, R. Fishman, O. Heber, M. Rappaport, N. Altstein, D. Zajfman, and W. J. van der Zande. A new type of electrostatic ion trap for storage of fast ion beams. *Review of Scientific Instruments*, 69(1):76–83, October 1997.

[25] D. A. Dahl. SIMION 3D Version 7.0, 2000.

[26] D. P. de Bruijn and H. Helm. Dissociative decay of n=3 levels in H_2. II. Excited by laser from the metastable c $^3\Pi_u^-$ state of H_2. *Phys. Rev. A*, 34(5):3855–3864, Nov 1986.

[27] D. P. de Bruijn and J. Los. Time and position-sensitive detector for dissociative processes in fast beams. *Rev. Sci. Instrum.*, 53(7):1020–1026, 1982.

[28] H. G. Dehmelt and K. B. Jefferts. Alignment of the H_2^+ molecular ion by selective photodissociation. I. *Phys. Rev.*, 125(4):1318–1322, Feb 1962.

[29] Liam M. Duffy, Thomas N. Feinberg, and Tomas Baer. Infrared vibrational photodissociation spectra of Ar_2^+ ions. *J. Chem. Phys.*, 101(4):2793–2799, 1994.

[30] M. Fieber, A. M. G. Ding, and P. J. Kuntz. A diatomics-in-molecules model for singly ionized neon clusters. *Z. Phys. D, Atoms Mol. and Clust.*, 23(2):171–179, 1992.

[31] R. Follath, F. Senf, and W. Gudat. Plane-grating monochromator at BESSY II using collimated light. *J. Synchrotron Rad.*, 5(3):769–771, May 1998.

[32] B. S. Freiser and J. L. Beauchamp. Gas phase ion chemistry and photochemistry of ions generated from Perflouropropylene. Photodissociation of the Perflouroallyl cation. *J. Am. Chem. Soc.*, 96(20):6260–6266, October 1974.

[33] R. Gredel, S. Lepp, A. Dalgarno, and E. Herbst. Cosmic-ray-induced photodissociation and photoionization rates of interstellar molecules. *Astrophys. J.*, 347:289–293, December 1989.

[34] T. A. Green, J. C. Browne, H. H. Michels, and M. M. Madsen. Configuration interaction studies of HeH^+ molecular ion. II. Dipole and radial coupling matrix elements for the singlet sigma states. *J. Chem. Phys.*, 61(12):5198–5204, 1974.

[35] T. A. Green, H. H. Michels, and J. C. Browne. Configuration interaction studies of the HeH^+ molecular ion. III. Singlet pi and delta states. *J. Chem. Phys.*, 64(10):3951–3956, 1976.

[36] T. A. Green, H. H. Michels, J. C. Browne, and M. M. Madsen. Configuration interaction studies of the HeH^+ molecular ion. I. Singlet sigma states. *J. Chem. Phys.*, 61(12):5186–5199, 1974.

[37] J. C. Hansen, J. T. Moseley, and P. C. Cosby. High-resolution photofragment spectroscopy of the O_2^+ $b^4\Sigma_g^-(\nu' = 5-8) \leftarrow a^4\Pi_u(\nu'' = 6-9)$ first negative system. *J. Mol. Spectros.*, 98(1):48–63, 1983.

[38] A.M. Hawryluk, J. A. Mangano, and J. H. Jacob. Gain and absorption measurements in a KrF* laser. *Applied Physics Letters*, 31(3):164–166, 1977.

[39] H. Helm and P. C. Cosby. Photodissociation measurement of rovibrational energies and populations of molecules in fast beams. *J. Chem. Phys.*, 86(12):6813–6822, 1987.

[40] R. C. Henry. The local interstellar radiation field. *Astrophys. J.*, 570:697–707, May 2002.

[41] R. C. Henry, R. C. Anderson, and W. G. Fastie. Far-ultraviolet studies. VII. The spectrum and latitude dependence of the local interstellar radiation field. *Astrophys. J.*, 239:859–866, August 1980.

[42] B. A. Huber, T. M. Miller, P. C. Cosby, H. D. Zeman, R. L. Leon, J. T. Moseley, and J. R. Peterson. Laser–ion coaxial beams spectrometer. *Rev. Sci. Instrum.*, 48(10):1306–1313, 1977.

[43] R. O. Hunter, J. Oldenettel, C. Howton, and M. V. McCusker. Gain measurements at 4416 Å on ArXeF* and KrF*. *J. Appl. Phys.*, 49(2):549–552, February 1978.

[44] O. Jagutzki, V. Mergel, K. Ullmann-Pfleger, L. Spiegelberger, U. Spillmann, R. Dörner, and H. Schmidt-Böcking. A broad-application microchannel-plate detector system for advanced particle or photon detection tasks: large area imaging, precise multi-hit timing information and high detection rate. *Nucl. Instr. Meth. Phys. Res. A*, 477:244–249, 2002.

[45] W. R. Jarmain and R. W. Nicholls. A theorectical study of the O_2 $x^3\Sigma_g^-$ - $b^3\Sigma_u^-$ photodissociation continuum. *Proc. Phys. Soc.*, 84:417–424, 1964.

[46] B. Jeziorski, K. Kołos, Wl.and Szalewicz, O. Fackler, and H. J. Monkhorst. Molecular effects in tritium β decay. II. Rotation-vibration excitation, dissociation, and rotational predissociation in the decay of the T_2 and TH molecules. *Phys. Rev. A*, 32(5):2573–2583, Nov 1985.

[47] P. R. Jones, G. M. Conklin, D. C. Lorents, and R. E. Olson. Differential elastic-scattering measurements of Xe^+ on Xe and Ar^+ on Ar in the 20-340ev range. *Phys. Rev. A*, 10(1):102–109, July 1974.

[48] S. Jonsell, A. Saenz, and P. Froelich. Neutrino-mass determination from tritium β decay: Corrections to and prospects of the experimental verification of the final-state spectrum. *Phys. Rev. C*, 60:034601, July 1999.

[49] K. P. Kirby and E. F. van Dishoeck. Photodissociation processes in the diatomic molecules of astrophysical interest. *Adv. Atom. Mol. Phys.*, 25:437–476, 1988.

[50] W. Kołos, B. Jeziorski, K. Szalewicz, and H. J. Monkhorst. Molecular effects in tritium β decay: Transitions to the discrete electronic states of the HeT^+ molecule. *Phys. Rev. A*, 31(2):551–555, February 1985.

[51] W. Kołos and J. M. Peek. New ab initio potential curve and quasibound states of HeH^+. *Chem. Phys.*, 12(4):381–386, 1976.

[52] A. M. Kondratenko and E. L. Saldin. Generation of coherent radiation by a relativistic electron beam in an ondolator. *Part. Accel.*, 10:207–216, 1980.

[53] P. J. Kuntz and J. Valldorf. A DIM model for homgeneous nobel gas ionic clusters. *Z. Phys. D, Atoms Mol. and Clust.*, 8:195–208, 1988.

[54] R. E. Kutina, A. K. Edwards, R. S. Pandolfi, and J. Berkowitz. Uv laser photodissociation of molecular ions. *The Journal of Chemical Physics*, 80(9):4112–4119, 1984.

[55] W. Lange. *Einführung in die Laserphysik*. Wissenschaftliche Buchgesellschaft, 1994.

[56] L. C. Lee and G. P. Smith. Photodissociation cross sections of Ne_2^+, Ar_2^+, Kr_2^+, and Xe_2^+ from 3500 to Å. *Phys. Rev. A*, 19(6):2329–2334, 1979.

[57] J. Lequeux and E. Roueff. Interstellar molecules. *Physics Reports*, 200(5):241–299, 1991.

[58] N. E. Levinger, D. Ray, M. L. Alexander, and W. C. Lineberger. Photoabsorption and photofragmentation studies of Ar_n^+ cluster ions. *J. Chem. Phys.*, 89(9):5654–5662, 1988.

[59] Z. Liu and P. B. Davis. Infrared laser absorption spectroscopy of rotational and vibration rotational transitions of HeH^+ up to the dissociation threshold. *J. Chem. Phys.*, 107(2):337–341, July 1997.

[60] V. M. Lobashev, V. N. Aseev, A. I. Belesev, A. I. Berlev, E. V. Geraskin, A. A. Golubev, O. V. Kazachenko, Yu. E. Kuznetsov, R. P. Ostroumov, L. A. Rivkis, B. E. Stern, N. A. Titov, C. V. Zadoroghny, and Yu. I. Zakharov. Direct search for neutrino mass and anomaly in the tritium beta-spectrum: Status of "troitsk neutrino mass" experiment. *Nucl. Phys. B - Proc. Suppl.*, 91(1-3):280–286, 2001.

[61] D. C. Lorents, R. E. Olson, and G. M. Conklin. Rainbow scattering for Ar^+ + Ar and Xe^+ + Xe. *Chem. Phys. Lett.*, 20(6):589–591, 1973.

[62] M. Martins, M. Wellhofer, J. T. Hoeft, W. Wurth, J. Feldhaus, and R. Follath. Monochromator beamline for FLASH. *Rev. Sci. Instrum.*, 77(11):115108, 2006.

[63] F. Matsushima, T. Oka, and K. Takagi. Observation of the rotational spectra of $^4HeH^+$, $^4HeD^+$, $^3HeH^+$, and $^3HeD^+$. *Phys. Rev. Lett.*, 78(9):1664–1666, March 1997.

[64] J. Mášik, J. Urban, P. Mach, and I. Hubač. Applicability of multireference many-body perturbation theory to the Ne_2^+ molecule. *Interantional Journal of Qunatum Chemistry*, 63:333–343, 1997.

[65] D. Meschede. *Optik, Licht und Laser.* Teubner Studienbücher, 1999.

[66] H. H. Michels and R. H. Hobbs. Electronic structure of the nobel gas dimer ions. I. potential energy curves and spctroscopic constants. *J. Chem. Phys.*, 69:5151–5162, 1978.

[67] H. H. Michels, R. H. Hobbs, and L. A. Wright. Electronic structure of the nobel gas dimer ions. II. Theoretical absorption spectrum for the $A^2\Sigma^+_{1/2u} \rightarrow d^2\Sigma^+_{1/2g}$ system. *J. Chem. Phys.*, 71(12):5053–5062, December 1979.

[68] S. Miller, J. Tennyson, S. Lepp, and A. Dalgarno. Identification of features due to H_3^+ in the infrared spectrum of supernova 1987A. *Nature*, 355(6359):420–422, 1992.

[69] T. M. Miller, J. H. Ling, R. P. Saxon, and J. T. Moseley. Absolute total cross sections for the photodissociation of Ar_2^+, Kr_2^+, Xe_2^+, KrN_2^+ and KrN^+ from 565 to 695nm. *Phys. Rev. A*, 13(6):2171–2177, June 1976.

[70] H.-U. Mittman and H.-P. Weise. Scattering of ions V. elastic scattering of the symmetric rare gas ion – Rare gas atom systems. *Z. Naturforsch. Teil A*, 29(1):400–410, 1974.

[71] J. Moseley and J. Durup. Fast ion beam photofragment spectroscopy. *Ann. Rev. Phys. Chem.*, 32:53–76, 1981.

[72] J. T. Moseley. Ion photofragment spectroscopy. In K. P. Lawley, editor, *Advances in chemical physics: Photodissociation and photoionization*, volume 60, pages 245–298. John Wiley & Sons, 1985.

[73] J. T. Moseley, P. C. Cosby, R. A. Bennett, and J. R. Peterson. Photodissociation and photodetachment of molecular negative ions. I. Ions formed in CO_2/H_2O mixtures. *J. Chem. Phys.*, 62(12):4826–4834, 1975.

[74] J. T. Moseley, R. P. Saxon, B. A. Huber, P. C. Cosby, R. Abouaf, and M. Tadjeddine. Photofragment spectroscopy and potential curves of Ar_2^+. *J. Chem. Phys.*, 67(4):1659–1668, August 1977.

[75] T. Nagata, J. Hirokawa, T. Ikegami, T. Kondow, and S. Iwata. Photodissociation of Ar_+^3 cluster ion. *Chem. Phys. Lett.*, 171(5-6):433–438, 1990.

[76] T. Nagata, J. Hirokawa, and T. Kondow. Photodissociation of Ar_n^+ cluster ions. *Chem. Phys. Lett.*, 176(6):530, February 1991.

[77] J. B. Ozenne, D. Pham, and J. Durup. Photodissociation of H_2^+ by monochromatic light with energy analysis of the ejected H^+ ions. *Chem. Phys. Lett.*, 17(3):422–424, 1972.

[78] C. Pagani, R. Bandelmann, D. Barni, M. Bonezzi, G. Grygiel, K. Jensch, W. Lange, A. Matheisen, W. D. Moeller, H.-B. Peters, B. Petersen, P. Pierini, J. Sekutowicz, D. Sellmann, S. Wolff, and K. Zapfe. The TESLA cryogenic accelerator modules. Technical Report 36, Deutsches Elektronen-Synchrotron DESY, Notkestr. 85, 22607 Hamburg, 2001.

[79] H. B. Pedersen. Geometry files for the ion beam trap. private communication.

[80] H. B. Pedersen. Molecular program for bound-continuum calculations. private communication.

[81] H. B. Pedersen. this section follows closely a note provided by H. B. Pedersen. private communication.

[82] H. B. Pedersen, S. Altevogt, B. Jordon-Thaden, O. Heber, M. L. Rappaport, D. Schwalm, J. Ullrich, D. Zajfman, R. Treusch, N. Guerassimova, M. Martins, J.-T. Hoeft, M. Wellhöfer, and A. Wolf. Crossed beam photodissociation imaging of HeH^+ with vacuum ultraviolet free-electron laser pulses. *Phys. Rev. Lett.*, 98(22):223202, June 2007.

[83] H. B. Pedersen, M. J. Jensen, C. P. Safvan, X. Urbain, and L. H. Andersen. Fast beam photofragment apparatus for studies of electronic and nuclear dynamics. *Rev. Sci. Instrum.*, 70(8):3289–3298, August 1999.

[84] H. B. Pedersen, D. Strasser, B. Amarant, O. Heber, M. L. Rappaport, and D. Zajfman. Diffusion and synchronization in an ion-trap resonator. *Phys. Rev. A*, 65(4):042704, Mar 2002.

[85] H. B. Pedersen, D. Strasser, O. Heber, M. L. Rappaport, and D. Zajfman. Stability and loss in an ion-trap resonator. *Phys. Rev. A*, 65(4):042703, Mar 2002.

[86] W. H. Press, S. A. Teukolsky, W. T. Vetterling, and B. P. Flannery. *Numerical recipes in FORTRAN*. Cambridge University Press, 1992.

[87] J. Raeder, K. Borraß, R. Bünde, W. Dänner, R. Klingelhöfer, L. Lengyel, F. Leuterer, and M. Söll. *Kontrollierte Kernfusion*. Teubner Studienbücher, 1981.

[88] Y. P. Raizer. *Gas discharge physics*. Springer-Verlag Berlin Heidelberg, 1997.

[89] M. Richter, A. Gottwald, U. Kroth, A. A. Sorokin, S. V. Bobashev, L. A. Shmaenok, J. Feldhaus, Ch. Gerth, B. Steeg, K. Tiedtke, and R. Treusch. Measurement of gigawatt radiation pulses from a vacuum and extreme ultraviolet free-electron laser. *Appl. Phys. Lett.*, 83(14):2970–2972, 2003.

[90] W. Roberge and A. Dalgarno. The formation and destruction of HeH^+ in astrophysical plasmas. *Astrophys. J.*, 255:489–496, April 1982.

[91] RoentDek Handels GmbH, Im Vogelshaag 8, 65779 Kelkheim-Ruppertshain, Germany. *HM1/T and HM1 TDC for PC (ISA or PCI)*, 6.2.1.83 edition.

[92] RoentDek Handels GmbH, Im Vogelshaag 8, 65779 Kelkheim-Ruppertshain, Germany. *Position and time sensitive multi-hit MCP delay-line detector system*, 6.2.82.8 edition.

[93] J. Rossbach. A VUV free electron laser at the TESLA test facility at DESY. *Nucl. Instr. Meth. Phys. Res. A*, 375(1-3):269–273, 1996.

[94] A. Saenz. Photoabsorption and photoionization of HeH^+. *Phys. Rev. A*, 67:033409, 2003.

[95] A. Saenz, S. Jonsell, and P. Froelich. Improved molecular final-state distribution of HeT^+ for the β-decay process of T_2. *Phys. Rev. Lett.*, 84(2):242–245, Jan 2000.

[96] S. Saha, K. K. Datta, and A. K. Barua. Photodissociation of HeH^+ by both electronic and vibrational transitions. *J. Phys. B*, 11(19):3349–3356, 1978.

[97] E. L. Saldin, E. A. Schneidmüller, and M. V. Yurkov. *The physics of Free Electron Lasers*. Springer-Verlag Berlin Heidelberg, 2000.

[98] R. Signorell and F. Merkt. The first electronic states of Ar_2^+ studied by high resolution photoelectron spectroscopy. *J. Chem. Phys.*, 109(22):9762–9771, 1998.

[99] U. Spillmann, O. Jagutzki, L. Spiegelberger, R. Dörner, V. Mergel, K. Ullmann-Pfleger, and H. Schmidt-Böcking. A novel delay-line anode design for position and time sensitive read-out of MCP-based detectors. *Physica Scripta.*, T92:225–226, 2001.

[100] G. Stark, K. Yoshino, K. I. Smith, and W. H. Parkinson. High-resolution absorption cross sections of carbon monoxide bands at 295k between 91.7 and 100.4 nanometers. *Astrophys. J.*, 369:574–580, March 1991.

[101] W. J. Stevens, M. Gardner, A. Karo, and P. Julienne. Theoretical determination of bound-free absorption cross section of Ar_2^+. *J. Chem. Phys.*, 67(6):2860–2867, September 1977.

[102] M. Szilágyi. *Electron and ion optics*. Plenum Press, 1988.

[103] D. E. Tolliver, G. A. Kyrala, and W. H. Wing. Observation of the infrared spectrum of the helium-hydride molecular ion $^4HeH^+$. *Phys. Rev. Lett.*, 43(23):1719–1722, Dec 1979.

[104] R. Treusch. Photon diagnostics for the VUV-FEL. *HASYLAB Annual report*, pages 159–164, 2005.

[105] D. J. Trevor, J. E. Pollard, W. D. Brewer, S. H. Southworth, C. M. Truesdale, D. A. Shirley, and Y. T. Lee. Photoionization mass spectroscopy of Ne dimers. *J. Chem. Phys.*, 80(12):6083–6091, 1984.

[106] N. P. F. B. van Asselt, J. G. Maas, and J. Los. Laser induced photodissociation of H_2^+ and D_2^+ ions. *Chem. Phys.*, 5(3):429–438, 1974.

[107] N. P. F. B. van Asselt, J. G. Maas, and J. Los. Laser induced photodissociation of H_2^+ ions. *Chem. Phys. Lett.*, 24(4):555–558, 1974.

[108] E. F. Van Dishoeck. Photodissociation and photoionization processes. In T. J. Millar and D. A. Williams, editors, *Rate coefficients in astrochemistry*, pages 49–72. Dordrecht and Norwell, MA, Kluwer Academic Publishers, 1988.

[109] J. A. Vanderhoff. Photodissociation cross section for Ar_2^+, Kr_2^+, and Xe_2^+ at 3.0 and 3.5ev. *J. Chem. Phys.*, 68(7):3311–3313, April 1978.

[110] F. von Busch and G. H. Dunn. Photodissociation of H_2^+ and D_2^+: Experiment. *Phys. Rev. A*, 5(4):1726–1743, Apr 1972.

[111] W. R. Wadt. The electronic states of Ar_2^+, Kr_2^+, Xe_2^+. I. Potential curves with and without spin-orbit coupling. *J. Chem. Phys.*, 68(2):402–414, January 1978.

[112] C. A. Woodward, B. J. Whitaker, P. J. Knowles, and A. J. Stace. The infrared photofragmentation of Ar_2^+. evidence of excited state population from dimer and cluster ionization. *J. Chem. Phys.*, 96(5):3666–3677, March 1992.

[113] A. Yariv. *Quantum Electronics*. Wiley, New York, 1989.

[114] D. Zajfman, O. Heber, L. Vejby-Christensen, I. Ben-Itzhak, M. Rappaport, R. Fishman, and M. Dahan. Electrostatic bottle for long-time storage of fast ion beams. *Phys. Rev. A*, 55(3):R1577–R1580, Mar 1997.

[115] R. N. Zare. Photoejection dynamics. *Mol. Photochem.*, 4:1–37, 1972.